Radiation Transfer
March 2000

By **Jean-Jacques Morcrette**

European Centre for Medium-range Weather Forecasts, Shinfield Park, Reading Berkshire RG2 9AX, United Kingdom

Table of contents

Abstract

These notes aim at fulfilling two different and somewhat contradictory objectives:

1) to give a general introduction to the parametrization of radiation transfer (RT) in numerical weather prediction and climate models. This might be useful to people who wish to look at general circulation model (GCM) outputs and to understand qualitatively how radiation transfer in clear and cloudy atmospheres is linked to the other physical processes, and how it can influence the atmospheric motions. In that case, the internal behaviour of the radiation scheme might remain a black box.

2) to provide a reasonably complete description of the RT parametrizations presently used in the ECMWF model to help understand the specific properties of the ECMWF forecasts. While the former task requires only basic knowledge of physics, the latter requires much more insight in how a RT scheme works.

The following pages somehow attempt to tackle these two tasks. After an introduction, the second chapter discusses the radiation budget at the top, and within the atmosphere, both globally and more regionally in relation with the other terms of the atmospheric energy balance. The third chapter is devoted to the derivation of the RT equation from an observational and

qualitative point of view and to the introduction to the basic laws of physics necessary to understand the RT. The simplifications that can be used when dealing with RT in the Earth's atmosphere, and the various approximations needed to make the RT a problem tractable for a numerical model of the atmosphere are also presented in chapter 3. The main aspects of the various RT parametrizations presently used in the ECMWF forecasting system are presented in chapter 4, together with the specification of the cloud optical properties. Examples of validation of various aspects of the parametrization of cloud-radiation interactions with observed radiation fields are presented in chapter 5. As a matter of conclusion, some comments on the future of RT calculations, and on some other radiation-related hot topics are given in chapter 6.

1. INTRODUCTION: AN HISTORICAL PERSPECTIVE

Among the various processes responsible for the diabatic heating of the atmosphere (convection, turbulence, large-scale condensation, heat, moisture and momentum transfer at the surface, radiation transfer), which have to be described by physical parametrizations in a general circulation model (GCM), this last one stands because its impact is felt at all times and over the whole 3-D domain. Compared to other processes, radiation transfer (RT) also stands as having a long history of theoretical developments. From the statistical and quantum mechanics at the end of the 19th and beginning of the 20th century, Boltzmann, Stefan, Wien, Planck and Einstein made pioneering advances in the spectral description of the radiation emitted by a black body. Afterwards, spectroscopic studies of the gases important for the radiative budget of the atmosphere, and the development of various approximations made the calculation of the radiation transfer in the atmosphere a tractable problem.

The very first such approximation is the separation between shortwave (SW) and longwave (LW) schemes due to the obvious wavelength difference between a black-body at Sun's temperature (around 5800 K, with most of its energy below 4 microns, and the energy source outside the atmosphere) and that of the atmosphere (globally averaged equivalent temperature of about 255 K as seen from the top of the atmosphere, with most of its energy above 4 microns, and the sources being the surface, the radiatively active gases (mostly H_2O, CO_2, O_3), and the clouds within the atmosphere). *Chandrasekhar* (1935, 1958, 1960) provided the first approximations to the radiation transfer in a scattering atmosphere. *Elsasser* (1938, 1942), *Goody* (1952, 1964), *Curtis* (1952, 1956), *Godson* (1953), *Malkmus* (1967) defined the first usable simplifications to the spectral representation of the radiation transfer including its dependence on two key atmospheric parameters, pressure and temperature, allowing atmospheric heating/cooling rates to be computed (*Rodgers and Walshaw*, 1966).

To the point, that in the mid-70s, it was said (WMO/Global Atmospheric Research Program, 1975) that radiation transfer was a solved problem, provided big enough computers were available. The only developments required were for fast parametrizations. A good description of the various approximations used in the 80's at the different stages in the development of computer-efficient radiation schemes (and of the necessary trade-offs between accuracy and efficiency, two contradictory arguments) is given in *Stephens* (1984) and *Fouquart* (1987).

Unfortunately, the InterComparison of Radiation Codes for Climate Models (ICRCCM) at the end of the 80s (*Ellingson et al.*, 1991; *Fouquart et al.*, 1991, *Baer et al.*, 1996) showed that, if an overall good agreement in clear-sky longwave computations by line-by-line models existed, large discrepancies were found in the results of both the LW parametrized schemes and all types of SW schemes. Hereafter, at least for clear-sky atmospheres, these were tracked down to deficiencies, mainly in the implementation of the approximations used to deal with the spectral and vertical integrations.

Since ICRCCM, a number of parametrized RT schemes have been developed from line-by-line (LbLs) models so that their accuracy, at least in clear-sky atmospheres, should be very close from that of LbLs (e.g., *Ramaswamy and Freidenreich*, 1992; *Edwards and Slingo*, 1996; *Mlawer et al.*, 1997, to name just a few. As far as clouds are concerned, the situation is much more complex with an ongoing debate whether or not clouds might absorb more than what current parametrizations account for, with the somewhat related role of the spatial inhomogeneities in the 3-dimensional distribution of water condensates on the radiation fields within and at the boundaries of a cloud, with

the role that the overlapping of cloud layers plays on the vertical distribution of the radiative fluxes and heating rates. Also the computational environment of a general circulation model might also impose some external limitations on the quality of the representation of the cloud-radiation interactions. In the following sections, an overview of these different questions will be provided.

2. THE EARTH'S RADIATIVE BALANCE AND ITS IMPLICATIONS

2.1 The need for parametrization

The need for a parametrization of the radiation transfer in a large-scale numerical model of the atmosphere stems for two reasons:

  •   first, like the other physical processes (condensation, surface processes, turbulence, ...) the radiation transfer actually occurs at spatial scales much smaller than the scales (e.g., interaction with cloud droplets) explicitly resolved by the model in its treatment of the adiabatic part of the prognostic equations;

  •   second, although the theory of radiation transfer has been well known for decades, the complexity of the governing equation is such that it cannot be used starightforwardly in a large-scale model. A much more computationally efficient scheme has to be designed to account for the effect of the radiative processes.

2.2 Global mean considerations

The importance of the radiation transfer processes for the Earth's atmosphere system is obvious: Radiation is the only way through which the Earth-atmosphere system can exchange energy with the rest of the universe. The importance of a proper representation of the radiative processes in climate modelling or weather forecasting (after a few days) comes from this simple consideration;

A zero-dimensional energy balance model describes the global annual mean equilibrium of the Earth-atmosphere system as

$$0.25(1 - \alpha)S_0 = F = \sigma T_e^4$$

where α is the planetary albedo (the ratio between reflected and incident solar energy at the top of the atmosphere, ToA), S_0 is the "solar constant" (the flux of energy from the Sun at the mean Sun–Earth distance), F is the outgoing terrestrial longwave radiation, T_e is the radiometric temperature of the Earth, and σ is the Stefan-Boltzmann constant ($\sigma = 5.67 \times 10^{-8}$ W m^{-2} K^{-4}). The factor 0.25   (= 1/4) arises from the Earth intercepting solar radiation proportionally to its cross-section and emitting terrrestrial radiation proportionally to its surface. According to the latest available satellite measurements (ERBE, Earth Radiation Budget Experiment, Barkstrom and Smith, 1986) $S_0 = 1372$ W m^{-2} and $\alpha = 0.295 \pm 0.010$. Thus F is 237 W m^{-2} and $T_e = 255$ K. The discrepancy between this value and the mean climatological surface temperature ($T_s = 288$ K) is explained by the so-called "greenhouse" effect, which will be discussed later.

Fig. 1 presents the various radiative streams within the atmosphere after Ramanathan (1987). Out of the 343 W m^{-2} of solar energy available at ToA in the 0.2 to 4 μm wavelength range, about 30% is reflected back to the outer space without change of wavelength after scattering in the atmosphere and/or reflection at the Earth's surface. There the true solar imput to the atmosphere is about 237 W m^{-2}. A large fraction of this reaches the surface and is absorbed by land masses and oceans; only roughly one quarter of this solar radiation is absorbed within the atmosphere and creates a mean heating of about 0.6 K/day. The exact fractions being absorbed within clouds and by

the "clear" atmosphere are presently debated (Cess et al., 1995; Ramanathan et al., 1995; Pilewskie and Valero, 1995; Stephens, 1996) with the role of aerosols in clear sky atmosphere and of cloud inhomogeneities recently coming to the forefront to explain this excess absorption not properly accounted by the current generation of radiation schemes in GCMs (e.g., Cairns et al., 2000). Part of the solar energy input to the surface (between 155 and 180 W m^{-2} depending on how much is actually absorbed within the atmosphere) is returned to the atmosphere by emission of terrestrial longwave radiation in the 4 to 100 μm wavelength range, but this emission (about 63 W m^{-2}, difference between 390 W m^{-2}, the longwave upward emission of the surface and 327 W m^{-2}, the longwave downward emission of the atmosphere) does not fully compensate for the solar flux into the surface. The deficit of about 106 W m^{-2} is compensated by turbulent transport of latent heat (for about 90 W m^{-2}) and sensible heat (for about 16 W m^{-2}) from the surface to the atmosphere. The existence of a radiative balance at ToA and of a radiative imbalance at the surface implies that the atmosphere itself is a net source of terrestrial longwave radiation to compensate for the warming by the solar heating, latent heat release and sensible heat flux. Thus the atmosphere cools through emssion of longwave radiation by about 1.6 K/day.

In the above discussion, only the figures of the radiation budget at ToA are known with some degree of accuracy thanks to some decades of satellite measurements. Estimates of the components of the energy budget at the surface are more difficult to obtain due to the lack of global coverage by conventional observation systems and to the alrge uncertainties in the ongoing tentative determination of these quantities from satellite measurements.

2.3 Time and space variations of the solar zenith angle and their consequences

The solar zenith angle θ_0 is the angle between the vertical at a given point on the Earth and the Sun's direction. Its cosine, μ_0, which is the relevant parameter for radiative computations can be computed knowing the latitude, the longitude, the time of the year, and the time of the day. μ_0 influences the radiation transfer in two ways:

- the amount of energy received at ToA is the product of the solar constant by a factor depending on the time of the year (1.0000 ± 0.0035) and by μ_0 if μ_0 is positive and zero otherwise (see Fig. 2);
- the atmospheric mass encountered by a solar beam is proportional to $1/\mu_0$ (for $\mu_0 > 0$).

Therefore, a diminishing μ_0 means not only less input at ToA but also more scattering and absorption within the atmosphere, therefore an even smaller solar flux at the surface. The time variations of μ_0 are the daily cycle and the yearly aseasonal cycle, which induce cyclic temperature variations and many specific patterns in the instantaneous weather. But the most important factor of influence of radiation on the weather is linked to its spece variations. Due to a better insolation of the equatorial belt than of the polar regions, which is not compensated by the terrestrial longwave output, the equatorial region is warmer than the polar ones. This situation has two major consequences for the weather:

- the same pressure layers are thicker at the equator than at the poles; since the sea level pressure is observed to be uniformly distributed due to friction in the planetary boundary layer, and according to Buys–Ballot's law, the zonal mean wind regime is of zonal westerlies, therefore the atmosphere precedes the Earth in its rotation;
- there is a need to transport heat from the equatorial to the polar regions. This transport is partly realized by the oceans, partly by the atmosphere, But a simple zonal circulation does not allow the atmosphere to fulfill this role and disturbances have to develop.

These last two points clearly indicate what is required from a radiation scheme in a large-scale numerical model of the atmosphere: first a good estimate of the pole–equator radiative imbalance, second an accurate partition of the poleward transport of heat between oceans and atmosphere.

In the tropics, the mean annual net heating of about 60 W m^{-2} is the sum of a 320 W m^{-2} heating by absorption of solar radiation and a 260 W m^{-2} cooling by emission of longwave radiation. This net heating of only about 20% of

the available solar input (the remaining 80% heat the tropical surface) is the driving force for the general circulation of the atmosphere and oceans. Therefore a 10% systematic error in the column absorbed solar radiation or in the longwave emission may potentailly translate into a factor 5 larger (i.e., 50%) change in the poleward transport of heat.

Also important is the dipole-like deposit of radiative energy in the earth–atmosphere system. As a whole, the troposphere is subject to a net radiative cooling (of about 106 W m^{-2}, Ramanathan, 1987), whereas the surface is subject to a net radiative heating of the same amplitude. Here again a 10% systematic error in the amplitude of this dipole will directly affect the destabilization of the troposphere, i.e., the fundamental drive for the tropospheric convection.

These questions may seem mainly related to climate studies, especially those performed with coupled ocean–atmosphere models. However the previous argument is also relevant to NWP modelling. NWP models are integrated with an analysed non-interactive sea-surface temperature, which provides the right oceanic heat transport. In the past, most NWP (and climate) models were using cloudiness fixed and/or zonally averaged to get the right answer for the pole-equator radiative gradient. Nowadays, NWP and climate GCMs have interactive cloudiness and cloud-radiation processes, as early satellite observations have shown the longitudinal gradients of radiative heating to be of the same magnitude as the latitudinal gradients, due to the cloud distribution (Stephens and Webster, 1979).

Such gradients are illustrated in Figs. 3 to 6 , which present averaged over the summer 1987 (June–July–August) the different components of the radiation budget derived from ERBE measurements. Fig. 3 displays the total and clear-sky absorbed SW radiation whereas Fig. 4 presents the reflected SW radiation. The clear-sky fields obtained by retaining the data only when clouds were found to be absent from the field of view of the satellite are highly zonal over the oceans, with only the land surface albedo differing with the various land types introducing marked departures. In comparison, the total fields clearly show the impact of the cloudiness with higher albedo (smaller absorption) in the ITCZ, the Indian monsoon and over the storm track. Minimum albedo (maximum absorption) is found over the relatively clear-sky subtropics, except over the extended low-level (stratocumulus) cloud decks on the western facades of the continents (California, Peru, Namibia). Fig. 5 presents the total and clear-sky outgoing longwave radiation for the same months. This field also displays the impact of the clouds, this time mainly of the high-level cloudiness usually linked to convection in the ITCZ or over the Indian monsoon area. Over the equatorial Pacific, the clear-sky OLR is less zonal than its SW counterpart indicating the role of moister atmospheres over the west part than over the eastern part of the basin. Fig. 6 presents the shortwave and longwave cloud forcing, i.e., the difference between clear-sky and total fluxes. In the shortwave, clouds with their reflecting effect are responsible for a cooling of the atmosphere-surface system, through a decrease of the energy available for heating. On the opposite, in the longwave, clouds contribute to a heating of the atmosphere by trapping the radiation coming from the surface and the lower layers of the atmosphere and by emitting at the cold temperatures representative of the higher clouds.

Cloud-radiation interactions are now thought to be of importance not only for mesoscale phenomena (the sea breeze is the best but not the only example of intercation between radiation and surface discontinuities to create local dynamical circulations), but also for synoptic scale phenomena such as the onset of the Indian monsoon (Webster and Stephens, 1980).

Finally, some systematic errors of a NWP model can be traced back to a deficient radiation transfer parametrization and at least partially corrected by an improved representation of the cloud-radiation interactions in the model (Morcrette, 1990).
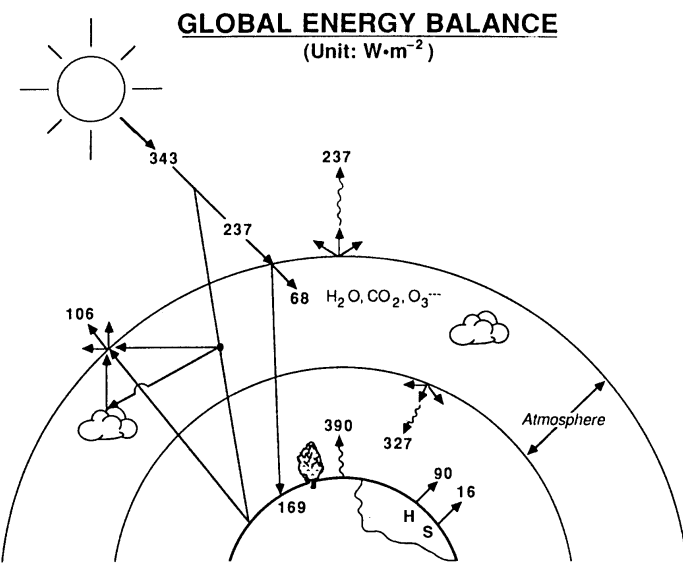
Figure 1. The global energy balance for annual mean conditions. The top-of-the-atmosphere estimates of solar insolation (343 W m^{-2}), solar radiation reflected by the whole atmosphere-surface system (106 W m^{-2}), and outgoing longwave radiation (237 W m^{-2}) are obtained from satellite data (Ramanathan, 1987). The other quantites in the figure are obtained from various published mode and empirical estimates, and might still be fraught with uncertainties. The quantities include: absorption of solar radiation at the surface (169 W m^{-2}), downward longwave radiation at the surface emitted by the atmosphere (327 W m^{-2}), upward longwave radiation emitted by the surface (390 W m^{-2}), and the turbulent heat fluxes from the surface, H the latent heat flux (90 W m^{-2}) and S the sensible heat flux (16 W m^{-2}).
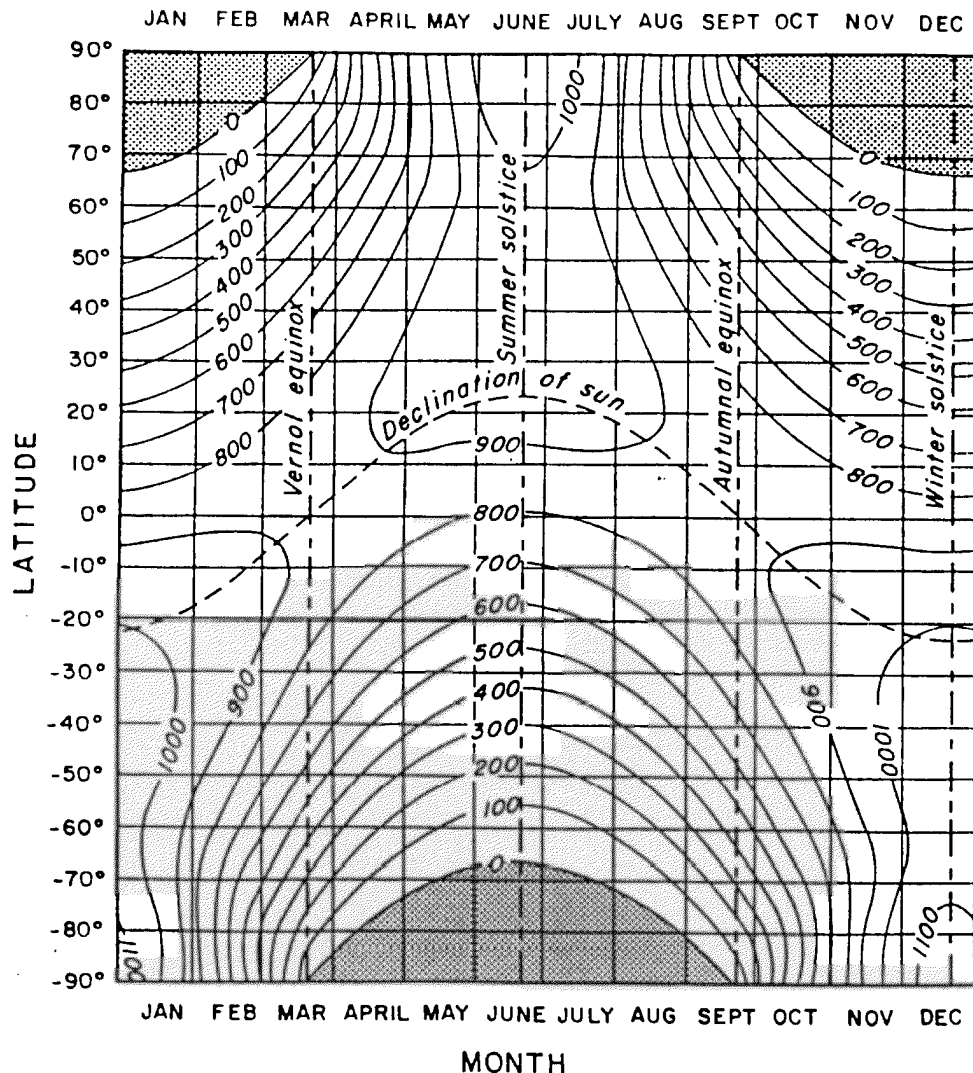
Figure 2. The daily variation of insolation at the top of the atmosphere as a function of latitude and day of the year in units of cal cm^{-2} day^{-1} (1 cal cm^{-2} day^{-1} = 0.4844 W m^{-2}) (after Paltridge and Platt, 1976).

ERBE Narrow FOV on (2.5 deg)^2 grid for 198706-08
erbe_nfov ASW   Area Mean: 0.258E+03
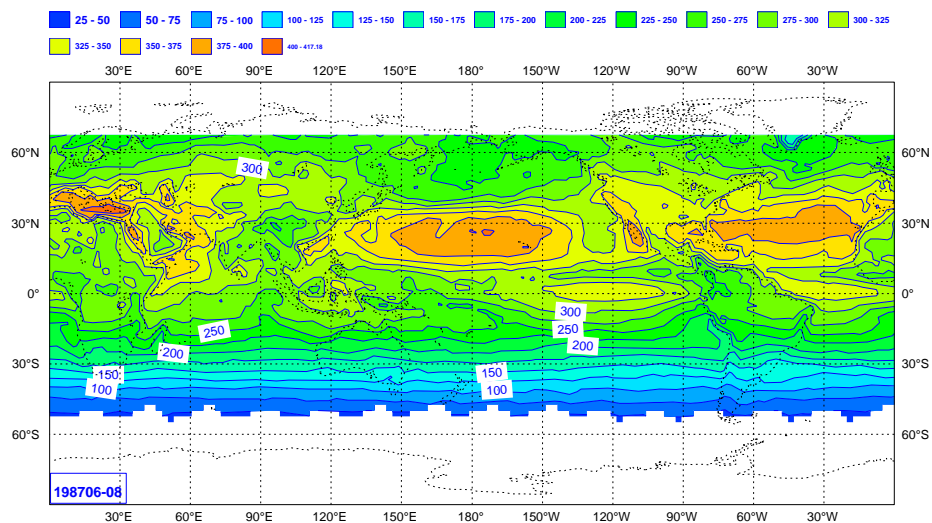
ERBE Narrow FOV on (2.5 deg)^2 grid for 198706-08
**erbe_nfov CSASW   Area Mean: 0.317E+03**
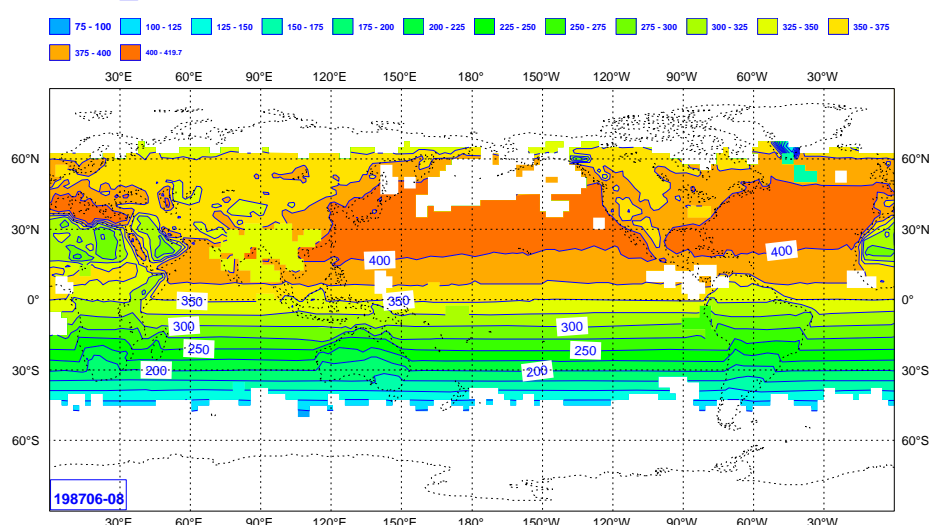
Figure 3. The absorbed shortwave radiation (top) and the clear-sky absorbed shortwave radiation (bottom) (W m^{-2}) derived from Earth Radiation Budget Experiment (ERBE) measurements for the summer 1987.

ERBE Narrow FOV on (2.5 deg)^2 grid for 198706-08
erbe_nfov REF   Area Mean: 0.100E+03
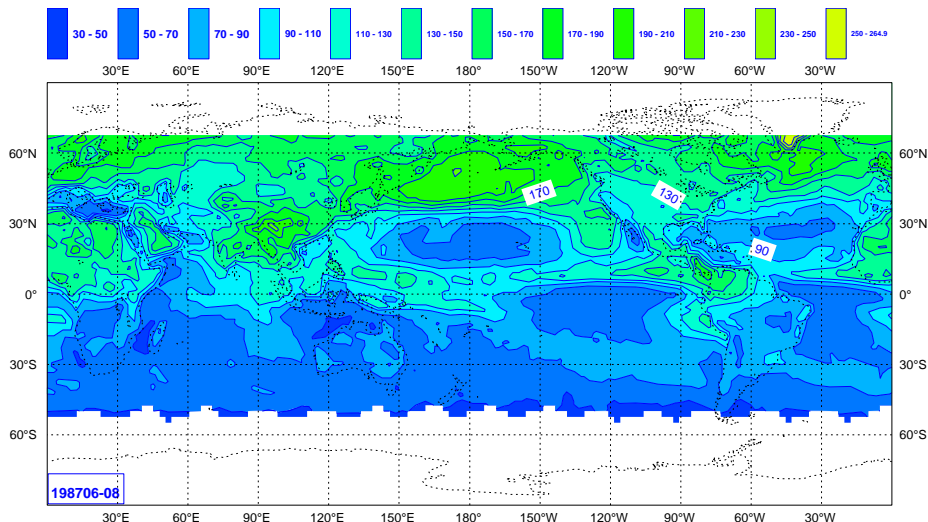
ERBE Narrow FOV on (2.5 deg)^2 grid for 198706-08
erbe_nfov CSREF   Area Mean: 0.519E+02
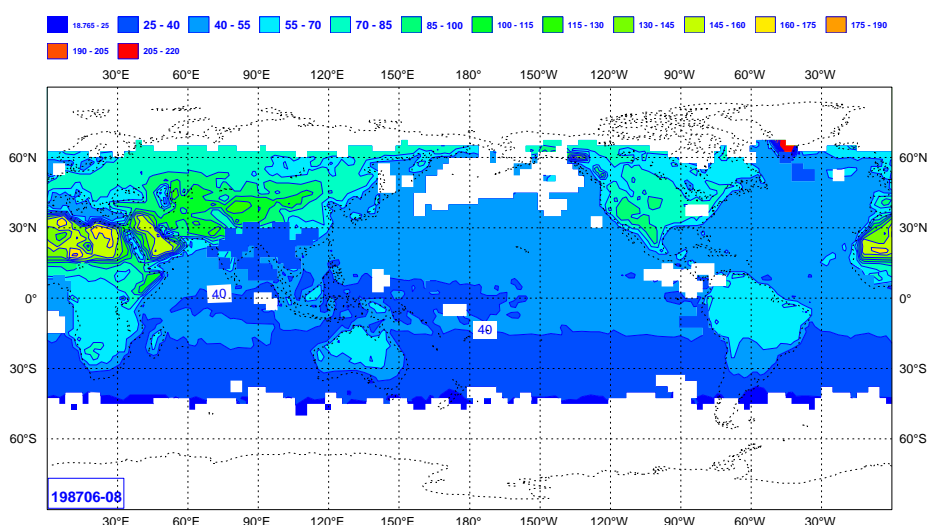
Figure 4. As in Fig. 3 , but in terms of the reflected shortwave radiation at the top of the atmosphere (W m^{-2}).

ERBE Narrow FOV on (2.5 deg)^2 grid for 198706-08
erbe_nfov TTR   Area Mean: -0.243E+03

ERBE Narrow FOV on (2.5 deg)^2 grid for 198706-08
**erbe_nfov CSTTR   Area Mean: -0.278E+03**
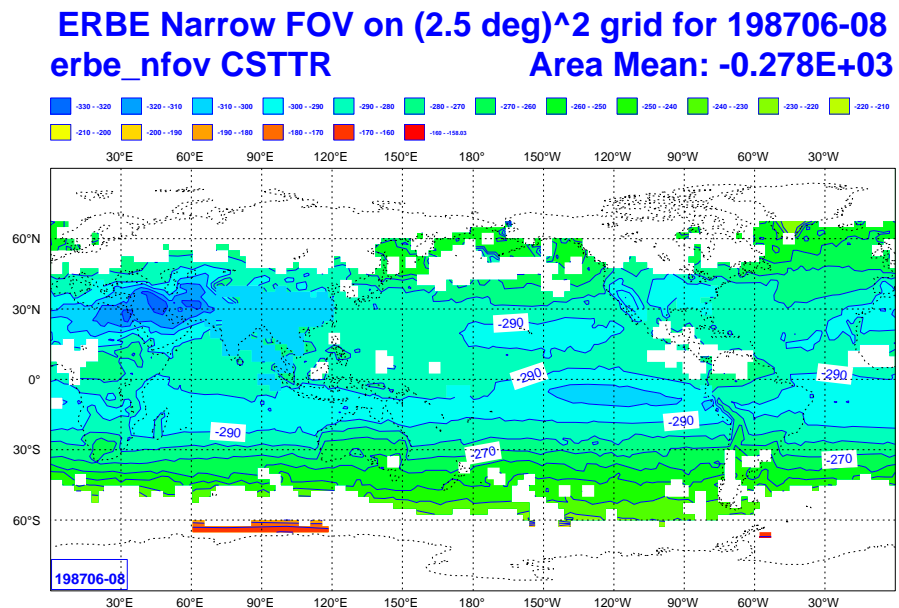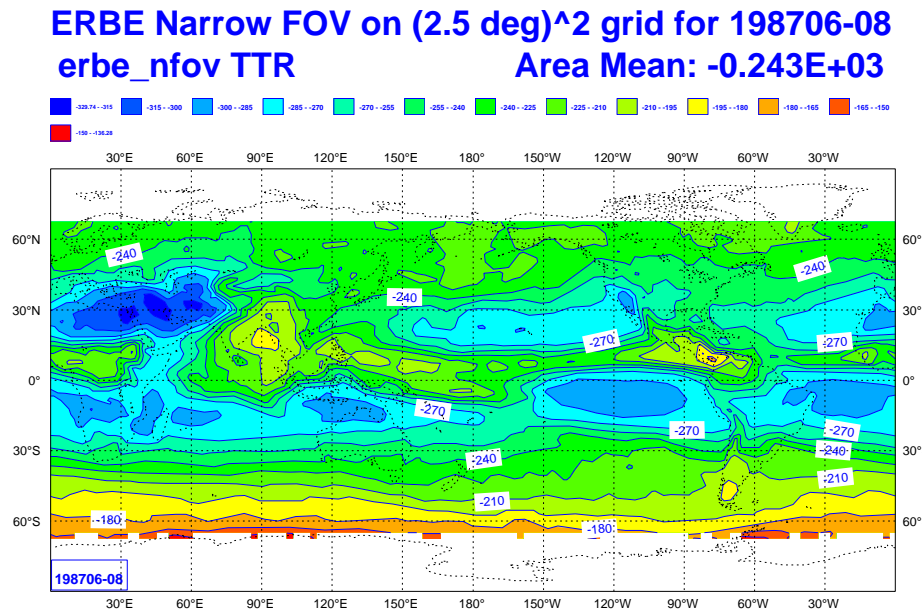
Figure 5. As in Fig. 3 , but for the outgoing longwave radiation at the top of the atmosphere (W m^{-2}).

ERBE Narrow FOV on (2.5 deg)^2 grid for 198706-08
erbe_nfov SWCF   Area Mean: -0.477E+02
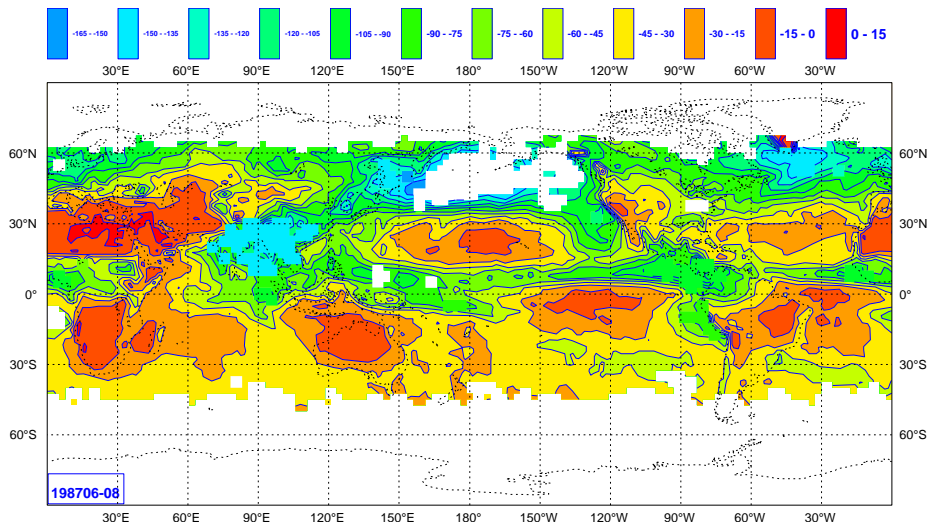
ERBE Narrow FOV on (2.5 deg)^2 grid for 198706-08
erbe_nfov LWCF   Area Mean: 0.288E+02
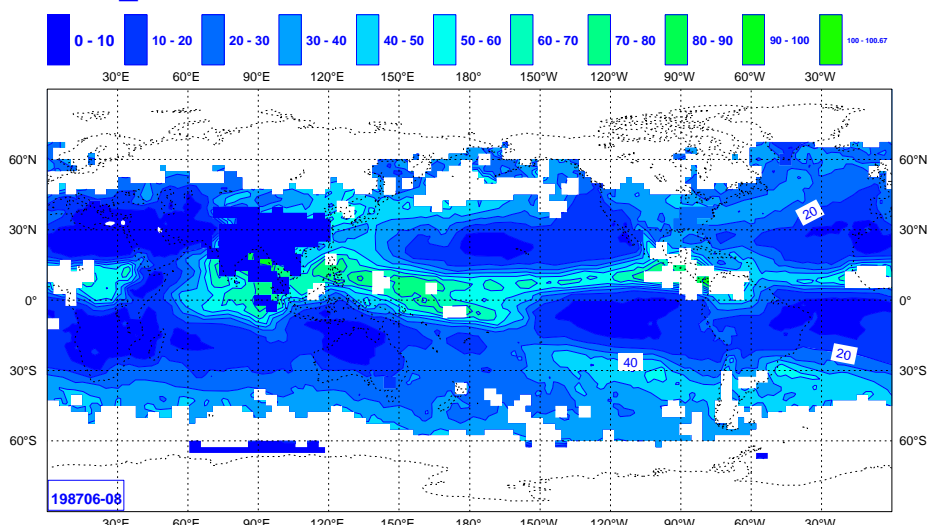
Figure 6. As in Fig. 3 , but for the shortwave (top) and longwave (bottom) radiative cloud "forcing" (W m^{-2}).

3. THE THEORY OF RADIATION TRANSFER

3.1 Terminology

Generally, radiation is considered to be the process of electromagnetic waves propagating through a medium (normally a planetary atmosphere). Some of the associated processes like absorption and thermal emission cannot be

adequately described by classical theory and require the use of quantum mechanics, which treats radiation as the propagation and interaction of photons. One characteristic property of radiation is its wavelength, A classification of radiation according to wavelength is presented in Fig. 7 (from Liou, 1980).

Wavelength λ, frequency ν, and wavenumber v are related through the relation $\lambda = c/\nu = 1/v$, where c is the speed of light ($c = 2.99792458$ m s^{-1}). The sensitivity of the human eye is confined to a rather small interval from 0.4 to 0.7 μm (micrometres) known as the visible region. However, most of the atmospheric exchange of radiative energy occurs from the ultraviolet (from about 0.2 μm) to the infrared (around 100 μm).

In atmospheric studies, two quantities are generally used, the flux per unit area in W m^{-2} and the specific intensity or radiance, i.e., the radiative energy per time through unit area into a given solid angle, in W m^{-2} sr^{-1}.

3.2 Derivation of the monochromatic radiative transfer equation (RTE)

The following discussion concerns the transfer equation for monochromatic radiation in its basic form for a plane-parallel, horizontally homogeneous atmosphere (Chandrasekhar, 1960).

In GCM applications, the radiation field is computed without accounting for polarization effects, and assuming stationarity (no explicit dependence on time). Only the point where radiation is considered, the direction of propagation, and the frequency matter for the problem. Fig. 8 presents schematically the different contributions to the specific intensity at a given point P enclosed by an infinitesimally small cyclindrical element of length $\mathrm{d}l$, of cross-section $\mathrm{d}a$, and of an orientation expressed in terms of two angles, i.e., θ, with respect to the z-axis and ϕ, the angle between the projection of the direction onto the $x-y$ plane and the x-axis itself. For a horizontally homogeneous atmospheric slice, the location of point P is given by its height z above ground (or any other suitable co-ordinate). Let us consider the various sources and sinks of radiative energy in this cyclindrical element:

3.2 (a) Extinction. The radiance $L_\nu(z, \theta, \phi)$ entering the cylinder at one end will be partially extinguished within the volume, proportionally to the amount of matter encountered, thus contributing a negative increment of radiative energy

$$\mathrm{d}Q_{\nu,\,\mathrm{ext}}(z, \theta, \phi) = -\beta_{\nu,\,\mathrm{ext}} L_\nu(z, \theta, \phi) \mathrm{d}a \ \mathrm{d}l \ \mathrm{d}\omega$$

where $B_{\nu,\,\mathrm{ext}}$ is the monochromatic extinction coefficient (units m^{-1}) and $\mathrm{d}\omega$ is the solid angle differential element.

3.2 (b) Scattering. Another contribution to a change in radiative energy in the volume is caused by the scattering of radiation from any other direction into the direction of the considered beam, i.e.,

$$\mathrm{d}Q'_{\nu,\,\mathrm{scat}}(z, \theta, \phi) = \beta_{\nu,\,\mathrm{scat}}\{p_\nu(z, \theta, \phi, \theta', \phi')/4\pi\} L_\nu(z, \theta', \phi') \mathrm{d}a \ \mathrm{d}l \ \mathrm{d}\omega \ \mathrm{d}\omega',$$

where $\beta_{\nu,\,\mathrm{scat}}$ is the monochromatic scattering coefficient, $\mathrm{d}\omega'$ is the solid angle differential element for the originating beam, $p_\nu(z, \theta, \phi, \theta', \phi')$ is the normalized phase function, which represents the probability for a photon incoming from direction (θ', ϕ') to be scattered in direction (θ, ϕ). Since scattered radiation may originate from any direction, we have to integrate over all possible angle combinations of θ' and ϕ'.

$$\mathrm{d}Q_{\nu,\,\mathrm{scat}}(z, \theta, \phi) = \beta_{\nu,\,\mathrm{scat}} \mathrm{d}a \ \mathrm{d}l \ \mathrm{d}\omega \int_{\omega'} L_\nu(z, \theta', \phi')\{p_\nu(z, \theta, \phi, \theta', \phi')/4\pi\} \ \mathrm{d}\omega'.$$

The direct (unscattered) solar beam is generally considered separately and not contained in the intensity of the direction considered. Thus scattering of the solar beam into the direction of interest is as well separate from the scattering of diffuse radiation

$$dQ^0_{\nu,\,\text{scat}}(z, \theta, \phi) = \beta_{\nu,\,\text{scat}}\{p_\nu(z, \theta, \phi, \theta^0\phi^0)/4\pi\}E^0_\nu \exp\left(-\frac{\delta_\nu}{\mu_0}\right)da\ dl\ d\omega,$$

where E^0_ν is the specific intensity of incident solar radiation, θ^0 and ϕ^0 define the direction of the incident solar radiation at ToA, μ_0 is the cosine of the solar zenith angle, and if z_{ToA} is the height of the top of the atmosphere, δ_ν is the optical thickness defined as

$$\delta_\nu = \int_z^{z_{\text{ToA}}} \beta_{\nu,\,\text{ext}}\ dz\ .$$

3.2 (c) Emission. The last contribution to the change in the radiative energy in the volume is the thermal emission:

$$dQ_{\nu,\,\text{emis}}(z, \theta, \phi) = \beta_{\nu,\,\text{abs}}B_\nu(T(z))\ da\ dl\ d\omega,$$

where $\beta_{\nu,\,\text{abs}}$ is the monochromatic absorption coefficient, and B_ν is the monochromatic Planck function.

3.2 (d) Total. The total change of radiative energy in the cyclinder can be written as the sum of the individual contributions

$$dQ_\nu(z, \theta, \phi) = dQ_{\nu,\,\text{ext}} + dQ_{\nu,\,\text{scat}} + dQ^0_{\nu,\,\text{scat}} + dQ_{\nu,\,\text{emis}} = dL_\nu(z, \omega, \phi)\ da\ dl\ d\omega$$

Replacing the length dl of the cylindrical element by the geometrical relation $dl = dz/\cos\theta = dz/\mu$ where $\mu = \cos\theta$, it follows from the expression of the optical thickness that $d\delta_\nu = -\beta_{\nu,\,\text{ext}}\ dz$

If we define κ_ν as the ratio of the absorption to the extinction coefficient $\kappa_\nu = \beta_{\nu,\,\text{abs}}/\beta_{\nu,\,\text{ext}}$ and the single scattering albedo $\omega = 1 - \kappa_\nu = \beta_{\nu,\,\text{scat}}/\beta_{\nu,\,\text{ext}}$, we finally obtain the monochromatic RTE for a plane parallel, horizontally homogeneous atmosphere in the coordinate system given by $((\delta_\nu, \mu = \cos\theta, \phi)$ as

$$\mu\frac{dL_\nu}{d\delta_\nu} = L_\nu(\delta_\nu, \mu, \phi) - (1 - \kappa_\nu)\int_0^{2\pi} d\phi' \int_{-1}^{+1} L_\nu(\delta_\nu, \mu', \phi')\{p_\nu(\delta_\nu, \mu, \phi, \mu', \phi')/4\pi\}\ d\mu'$$

$$- (1 - \kappa_\nu)E^0_\nu \exp\left(-\frac{\delta_\nu}{\mu_0}\right)\{p_\nu(\delta_\nu, \theta, \phi, \theta^0, \phi^0)/4\pi\}$$

$$- \kappa_\nu B_\nu(\delta_\nu).$$

In principle, the RTE derived above allows the complete problem of the radiative transfer in a NWP to be solved if the specific intensities L_ν are known for all model layers, i.e., including the surface, all directions and all wavenumbers of the spectrum. But in this present form, the RTE is much too complicated to be used as such in a NWP or climate GCM. We will now consider various simplications linked either to the basic laws of physics or to the very specific circumstances prevailing in the Earth's atmosphere.

3.3 Basic laws

3.3 (a) Planck's law. The energy of an atomic oscillator is quantized, as is any change of energy state. The change of the energy state by one quantum number corresponds to an amount of energy (either radiated or absorbed) of $\Delta E = h\nu$ where $\nu = c/\lambda$ is the frequency of the atomic oscillator and $h = 6.6260755 \times 10^{-34}$ J s is Planck's constant. For a large sample of atomic oscillators where the distribution of energy levels follows Boltzmann statistics, one can derive Planck's function for the emission of radiant energy by a black body (see details in Liou, 1980)

$$B_\lambda(T) = \frac{2hc^2}{\lambda^5}\left\{\exp\left(\frac{hc}{\lambda kT}\right) - 1\right\} \quad \text{W m}^{-2}\mu\text{m}^{-1},$$

where λ is the wavelength of emission, k is Boltzmann constant, $k = 1.380658 \times 10^{-23}$ J K^{-1}, c is the velocity of light in a vacuum, and T is the absolute temperature of the black body (in K).

3.3 (b) Wien's law. The dependence of $B_\lambda(T)$ on λ for various temperatures is shown in Fig. 9 . The dotted line in the diagram marks the wavelength of the maximum intensity. It increases with the temperature of the black body and its variation follows Wien's displacement law. Extreme values of the Planck function are defined by

$$\frac{dB_{\lambda_{\text{max}}}}{d\lambda} = 0.$$

With $c_1 = 2hc^2$ and $c_2 = hc/k$, and defining $x = c_2/(\lambda T)$ and $\lambda^5 = c_2^5/(x^5 T^5)$, the previous condition can be rewritten as

$$\frac{d}{dx}\left\{\ln\left[\frac{c_1 T^5 x^5}{c_2(\exp(x) - 1)}\right]\right\} = 0.$$

After some manipulation (see, e.g., Liou, 1980), we obtain a transcendental equation $5 - 5\exp(-x) = x$,which can be shown to give $x = 4.9651$ provided that $5\exp(x) < 1$.

This translates into $\lambda_{\text{max}} T_{\text{max}} = 2897$ μm K .

Wien's displacement law considerably simplifies the radiation transfer problem in the Earth's atmosphere. Atmospheric and surface temperatures are typically in the 200–300 K range and the maximum emission occurs in the 10 to 15 μm wavelength range. On the other hand, the Sun, the Earth's external source of radiative energy emits most of its energy at wavelengths around about 0.5 μm corresponding to an equivalent black body at about 6000 K. At the mean Earth–Sun distance of 1.5×10^8 km, the monochromatic radiant intensity received from the Sun over a wide range of the spectrum is much less than the emission by the Earth's atmosphere system at equivalent wavelengths. The cross-over point is approximately at 3.5 μm . For wavelengths lower than 3.5 μm , the terrestrial emission is negligible and so is the energy received from the Sun at ToA for wavelengths larger than 3.5 μm . For this reason, when designing a radiation scheme for application to the Earth's atmosphere, one may separate the transfer problem in two parts, the shortwave and longwave radiative transfer, by dealing independently with the sources and sinks that are important for each part of the spectrum.

3.3 (c) Stefan-Boltzmann law. The total radiant intensity of a black body follows from a spectral integration of the Planck function over all wavelengths, i.e.,

$$B(T) = \int_0^\infty B_\lambda(T) \, d\lambda .$$

Using the same substitutions as when deriving Wien's displacement law, we get

$$B(T) = \frac{2k^4 T^4}{h^3 c^2} \int_0^\infty \left[\frac{x^3}{\exp((x)-1)} \right] dx .$$

The integral term has the value $x^4/15$, so we finally obtain Stefan–Boltzmann law

$$F = \pi B(T) = \sigma T^4 \quad \mathrm{W \, m^{-2}} ,$$

where $\sigma = 5.6697 \times 10^{-8}$ W m^{-2} K^{-4} is Stefan's constant. The total emitted flux given by this equation already implies that the angular integration over the total radiant intensity is performed assuming an isotropic emission by the black body (which is verified), leading to the factor π.

3.3 (d) Kirchhoff's law. The emissivity ε_λ of a medium is the ratio of the emitted energy to the Planck function at the temperature of the medium for a given wavelength λ. If the absorptivity a_λ is defined as the amount of energy absorbed at that wavelength divided by the appropriate Planck function, Kirchhoff's law states that the two quantites are equal, i.e.,

$$\varepsilon_\lambda = a_\lambda .$$

A black body is defined by its ability to absorb all the incoming radiation at a given wavelength and therefore to emit isotropically according to Planck function; then for a black body $\varepsilon_\lambda = a_\lambda = 1$. In contrast, grey bodies absorb and emit only partially with values of ε_λ and a_λ being less than unity.

The Earth's atmosphere is far from being a medium with a uniform temperature distribution. However, the assumption of a thermodynamic equilibrium ($\varepsilon_\lambda = a_\lambda$) is still valid in a local sense, since at least for the lower part of the atmosphere (approximately below 40 km), collision between molecules is a process efficient enough to maintain a local thermodynamic balance.

Name of region	Wavelength (cm)	Frequency (cps)
Gamma rays	10^{-9}	3×10^{19}
x rays	10^{-6}	3×10^{16}
Ultraviolet	3×10^{-5}	10^{15}
Visible		
Infrared	10^{-4}	3×10^{11}
	10^{-1}	
Microwaves	1	3×10^{10}
Spacecraft	10^{2}	3×10^{8}
Television & FM	10^{3}	3×10^{7}
Shortwave	10^{4}	3×10^{6}
AM	10^{5}	3×10^{5}
Radio waves		

Violet
Purple
Blue
Green
Yellow
Orange
Red
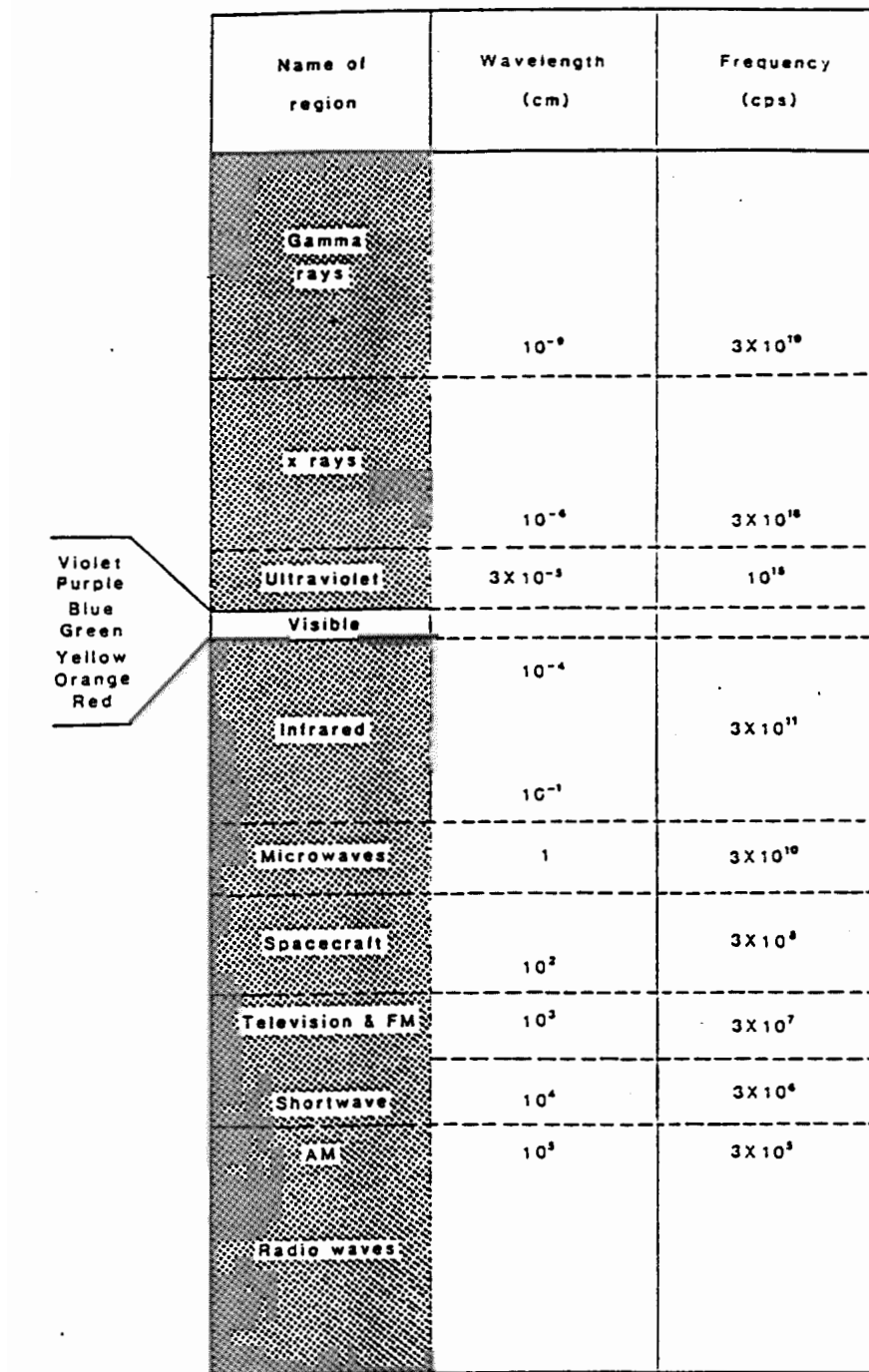
Figure 7. The electromagnetic spectrum
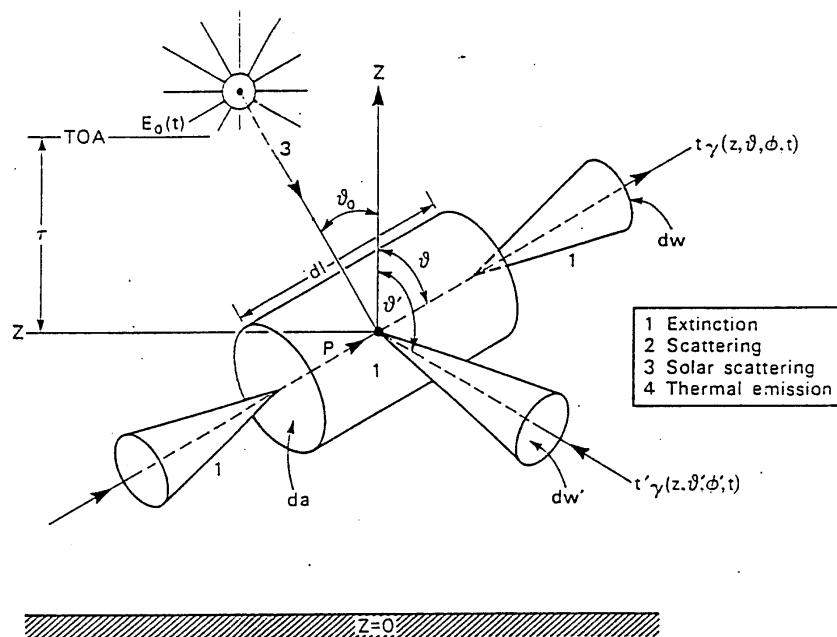
Figure 8.Processes contributing to the radiative transfer in a cylindrical volume
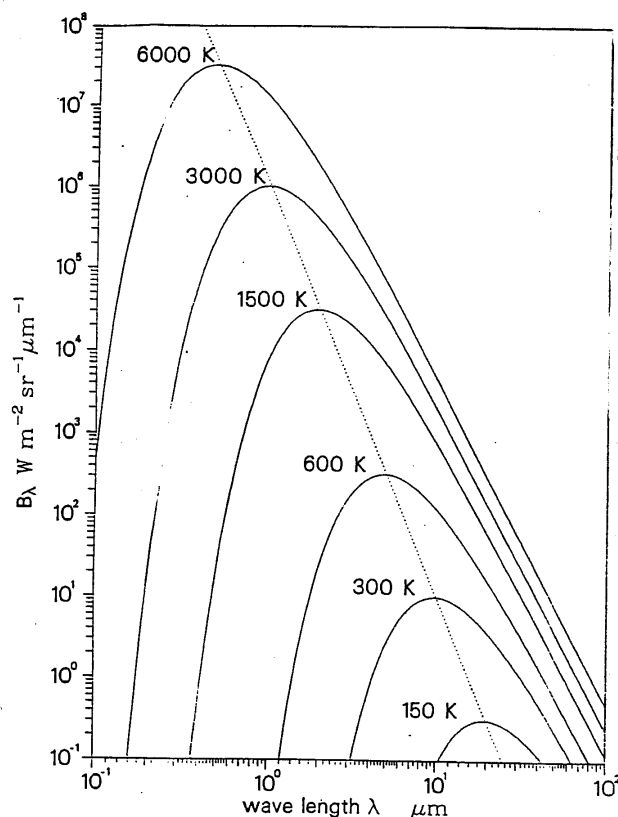
Figure 9. The dependence of the Planck function on wavelength and temperature. Wavelengths of maximum emssion are connected by a dotted line

In Subsection 3.2, the derivation of the RTE and its formal solution were carried out monochromatically. It is now necessary to consider the spectral variations of the various parameters (scattering and extinction coefficients, single scattering albedo and phase function). By contrast with the emission of a black body which displays smooth variations with temperature and wavelength, the absorption, emission and scattering by particles and gases give rise to highly variable spectra of parameters.

3.4 The spectral absorption by gases

Any moving particle has kinetic energy as a result of its motion in space. This energy is equal to $kT/2$ and is not quantized. However molecules have other radiative energy types, which can be described from a mechanical model of the molecules. The absorption of radiative energy by gases is an interaction process between molecules and photons and thus obey quantum mechanics laws. Absorption and emission take place when the atoms and molecules undergo transitions from one energy state to another. In contrast to "grey" absorbers such as solid particles and liquids, which absorb radiation fairly uniformly with respect to wavelengths (a consequence of the dense packing of molecules and atoms in these), the absorption and emission by atmospheric gases are highly selective with regards to wavelength, due to the selection rules that govern the transitions.

The gaseous absorption spectrum can be categorized in three parts according to the total (radiative) energy of the molecules:

The molecule may rotate or revolve about an axis through its centre of gravity. The relatively low rotational energy of the molecules is associated with wavelengths in the far infrared (i.e., $\lambda > 20$ mm). In this spectral region absorption lines are well separated and are related to the transformation from one discrete rotational state into another.

The atoms of the molecule are bounded by certain forces, but the individual atoms can vibrate about their equilibrium position relative to each other. A combination of rotational and vibrational energy transformations causes absorption lines in the 1 to 20 μm region. The coexistence of both types leads to very complex structures (e.g., the the vibration-rotation band of H_2O around 6.3 μm) as an enormous number of lines are involved, which partially overlap each other.

Towards shorter wavelengths, the third form of energy transformation, the change of the energy level of electrons, occurs and this change in the electronic levels of energy increases further the complexity of the spectrum (e.g., O_2 bands in the ultraviolet).

3.4 (a) Line width. Each spectral line corresponds exactly to one form of energy transformation and should in principle be discontinuous due to the discrete energy levels. However, due to Heisenberg's uncertainty principle (natural broadening), the collision between molecules (Lorentz or pressure broadening), and Doppler effects (resulting from the thermal velocity of atoms and molecules), absorbed and emitted emission is not strictly monochromatic, but is rather associated with spectral lines of finite width. Whereas the natural broadening affects the line width only marginally, the other two have a marked impact on the shape of the spectral lines and therefore on the absorption process itself.

The Doppler broadening occurs due to the thermal agitation within the gas. For a molecule of mass m radiating at frequency ν_0, with a velocity component v in the line of sight following a Maxwell–Boltzmann probability distribution

$$P(v)\, dv = \left(\frac{m}{2\pi kT}\right)^{0.5} \exp\left(-\frac{mv^2}{2kT}\right) dv \, ,$$

the absorption coefficient of such a Doppler broadened line is

$$k_D(\nu) = \frac{S_D}{a_D(\pi)^{0.5}} \exp\left\{-\left[\frac{(\nu - \nu_0)}{a_D}\right]^2\right\},$$

with $a_D = \nu_0 / c \ (2kT/m)^{0.5}$.

The pressure broadening is due to collisions between the molecules, which modify their energy levels. The resulting absorption coefficient is

$$k_L(\nu) = \frac{S\alpha_L}{\pi[(\nu - \nu_0)^2 + \alpha_L^2]},$$

with $\alpha_L = \alpha_{L0} P / P_0 \ (T_o/T)^{0.5}$ making it proportional to the frequency of collisions.

Fig. 10 compares typical Lorentz and Doppler line shapes.

3.4 (b) Line intensity. The intensity of a line varies with temperature, due to the variation with T of the statistical population of the energy levels of a molecule.

$$S = S_0\left(\frac{T_0}{T}\right)^{\mathbf{em}} \exp\left\{-\frac{E}{k}\left(\frac{1}{T} - \frac{1}{T_0}\right)\right\},$$

where E is the energy of the lower state of the transition, **em** is an exponent the value of which depends on the shape of the molecule (1 for CO_2, 3/2 for H_2O, 5/2 for O_3) and T_0 is the reference temperature at which the line intensities are known (and compiled, usually 296 K).

An example of the fine scales involved is given in Fig. 11 taken from Fisher (1985). The figure shows the 15 μm band of CO_2 at varying spectral resolution. Even on a wavenumber interval as small as 0.01 cm^{-1} (the 15 μm band covers roughly 450 to 800 cm^{-1}), the absorption varies over the full range from total absorption to total transmission. It is this extreme spectral dependency of gaseous absorption that makes an explicit integration of the monochromatic RTE and subsequent spectral integration of fluxes quite a lengthy task, even on the fast super-computers, and renders it impossible for operational use in a NWP model. Very detailed models of the radiation transfer exist, which performs the spectral integration over wavenumber intervals the width of which is typically smaller than the half-width of an individual line. These so-called "line-by-line" calculations can serve as reference for more approximate methods. At present the number of known spectral lines for gases existing in the Earth's atmosphere is of the order of 300,000 (Rothman et al., 1998).

Figs. 12 to 14 show the spectral dependency of the gaseous absorption coefficient for the three main atmospheric absorbers H_2O, CO_2 and O_3 over the longwave part of the spectrum. The values are derived from an evaluation of spectroscopic data over 5 cm^{-1} intervals between 0 and 1110 cm^{-1}, 10 cm^{-1} between 1110 and 2200 cm^{-1}, and 20 cm^{-1} beyond 2200 cm^{-1}, with the narrow-band model of Morcrette and Fouquart (1985). Similarly, Figs. 15 to 17 show the temperature dependency of the absorption coefficients for the same absorbers in terms of $\log_{10}[k(300 \text{ K})/k(250 \text{ K})]$ and $\log_{10}[k(200 \text{ K})/k(250 \text{ K})]$, with $0 = \log_{10}(1)$ corresponding to $k(250 \text{ K})$, the absorption coefficient at 250 K.

Fig. 18 shows the spectral dependency of the gaseous absorption coefficient for the three main absorbers over the whole range of wavenumbers relevant for atmospheric energy budget. To put the importance of of the absorption lines for the atmospheric transfer in perspective, the normalized Planck function for 6000 K (solar emission) and 255 K (terrestrial emission) are plotted underneath. It is obvious that H_2O is the most important absorber in the terrestrial spectrum leaving a transparent region only around 10 μm. The so called 9.6 μm band of ozone partially

fills this gap. However, as the amount of O_3 in the atmosphere is not very large and is concentrated in the stratosphere, the atmosphere is fairly transparent (with respect to gaseous absorption) in this region of the spectrum called the atmospheric window. Absorption effect of trace gases such as methane (CH_4), nitrous oxide (N_2O) and chlorofluorocarbons (CFC-11 and CFC-12) are mainly felt in this spectral region due to the small background absorption.

Towards longer wavelengths this window is bounded by CO_2 absorption (the 15 µm band) and the H_2O rotation band. Towards shorter wavelengths but still in the terrestrial radiation, we find the vibration-rotation of H_2O around 6.3 µm. At very short wavelengths (in the ultraviolet region below 0.25 µm), ozone absorbs almost completely the solar radiation penetrating the atmosphere. However, in the so called visible (0.4–0.7 µm) and near-infrared (0.7–4 µm) regions of the solar spectrum, solar radiation is weakened only by H_2O and more modestly by CO_2 and other trace gases (NO_2, O_2, CH_4, N_2O, not shown in Fig. 18)
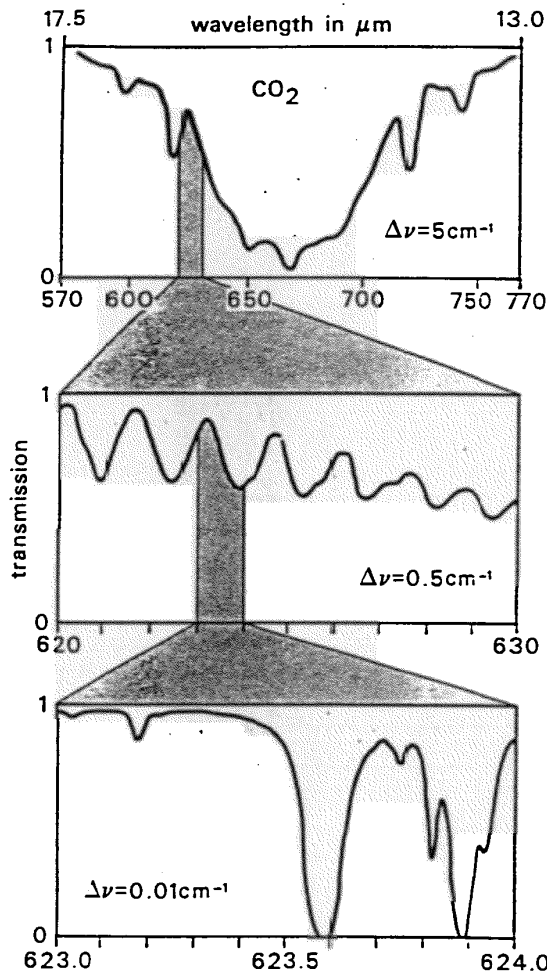
Figure 10. Transmission in the 15 µm band of CO_2 at various spectral resolutions (after Fisher, 1985)
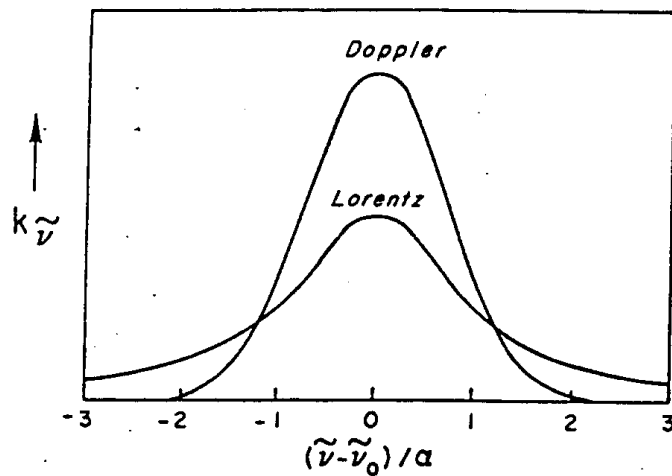
Figure 11. Lorentz and Doppler line shapes for similar intensity and line width (after Liou, 1980)
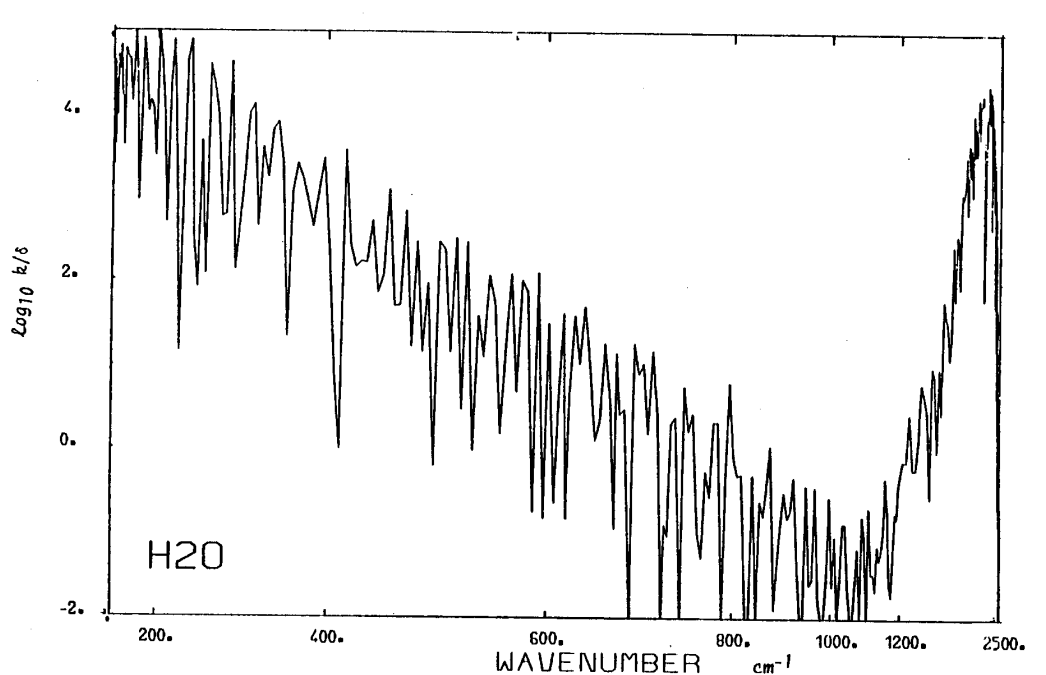

Figure 12. The absorption coefficient $k/\delta = \sum S_i/\Delta\nu$ for H_2O at 250 K as a function of the wavenumber. The abscissa is given by the fraction of the black body function between 0 and ν (in cm^{-1}) divided by the integral of $B_\nu(250\ K)$ between 0 and 2500 cm^{-1}.
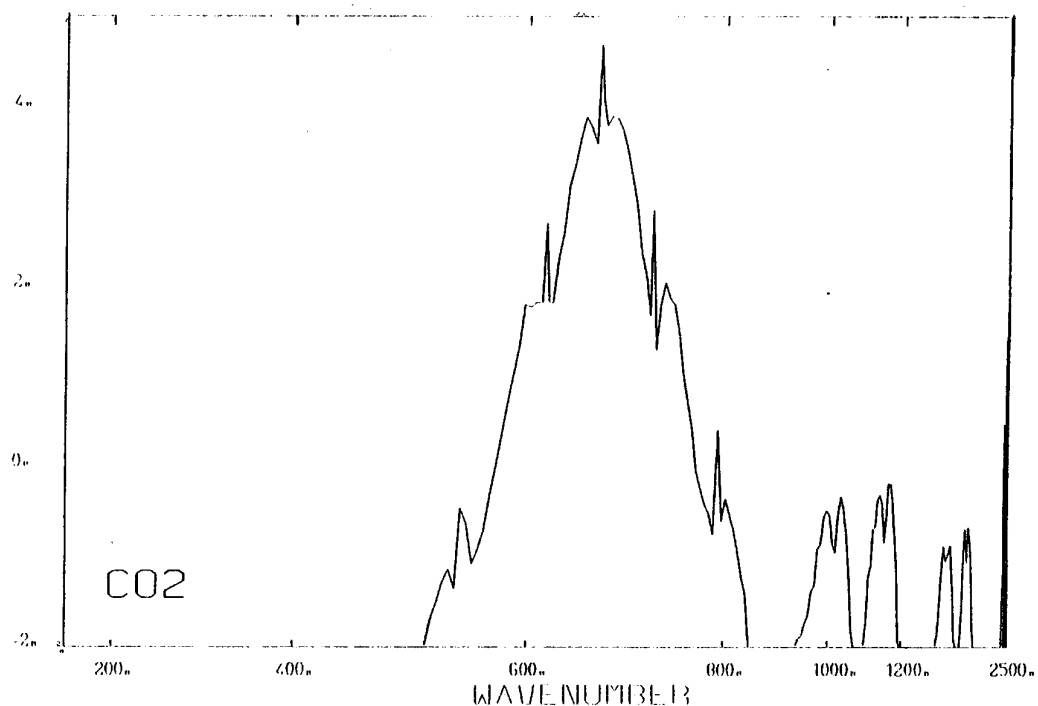
Figure 13. As in Fig. 11 , but for CO_2.
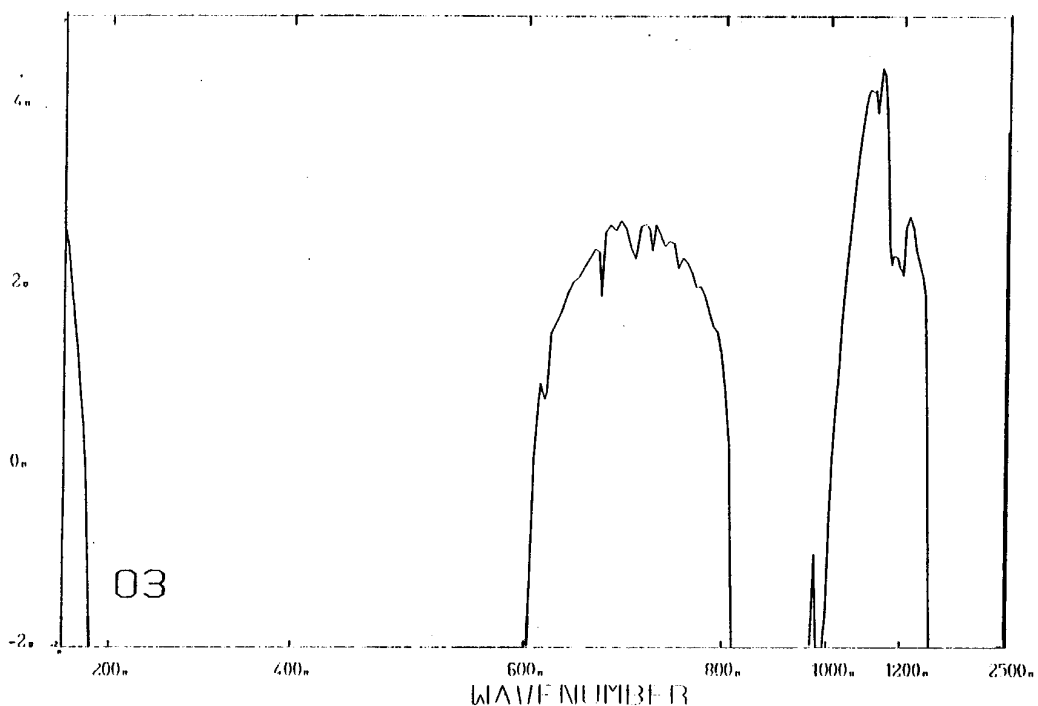
Figure 14. As in Fig. 12 , but for O_3.
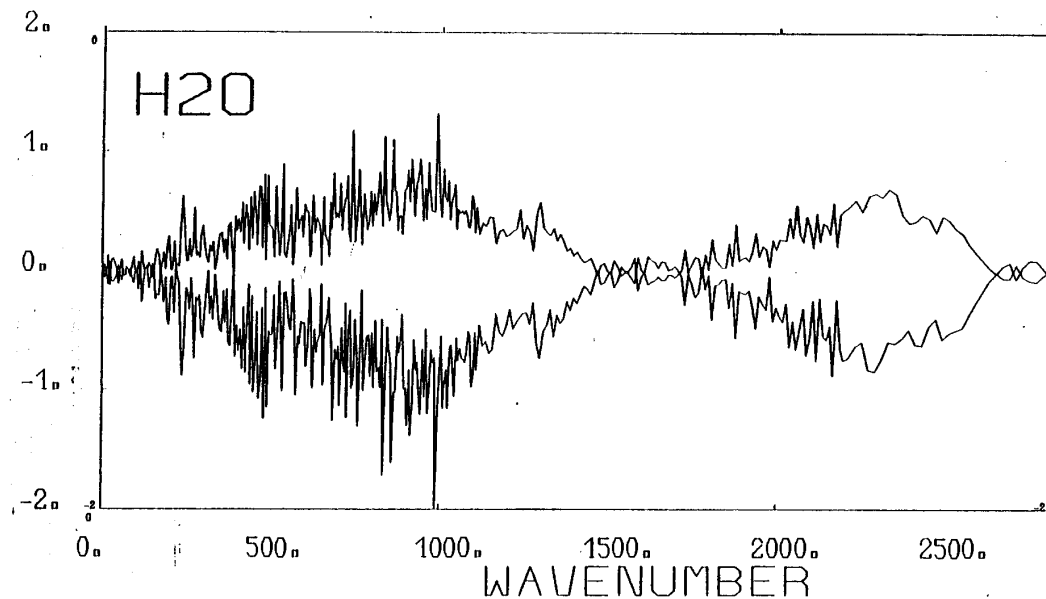
Figure 15. Effect of the temperature of the absorption coefficient for H_2O. The upper curve is for 300 K, the lower one for 200 K.
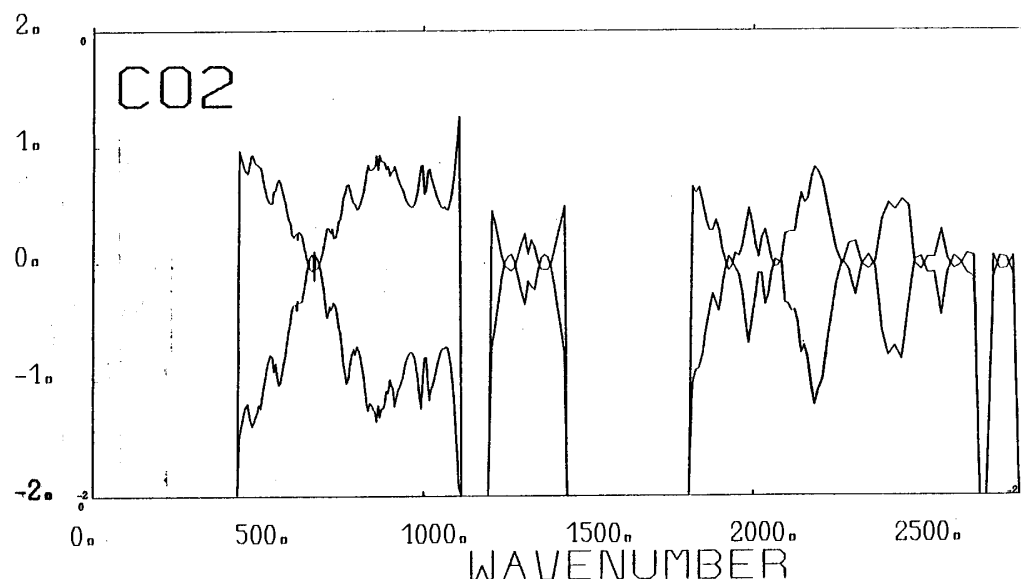

Figure 16. As in Fig. 14 , but for CO_2.
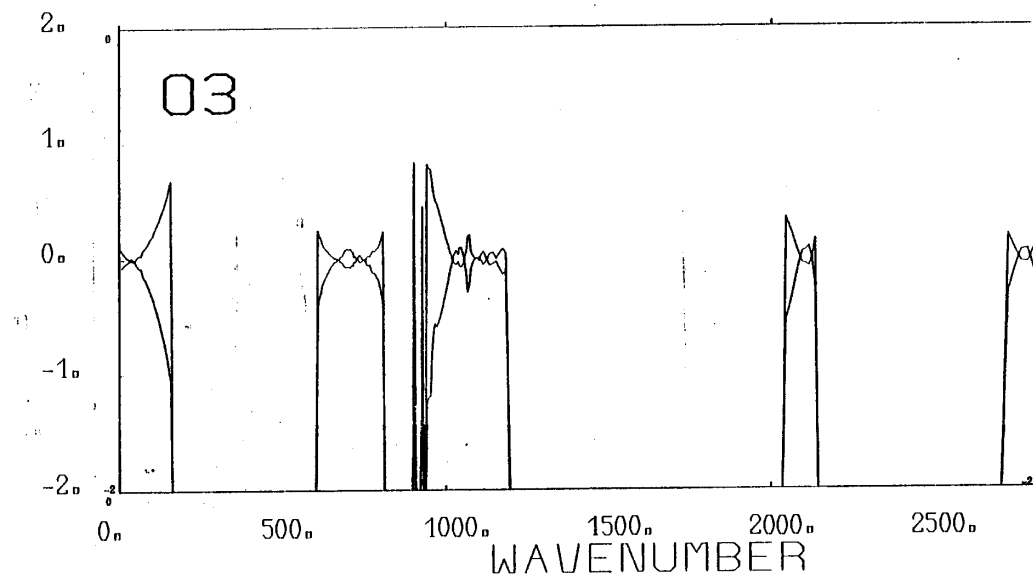
Figure 17. As in Fig. 14 , but for O_3.
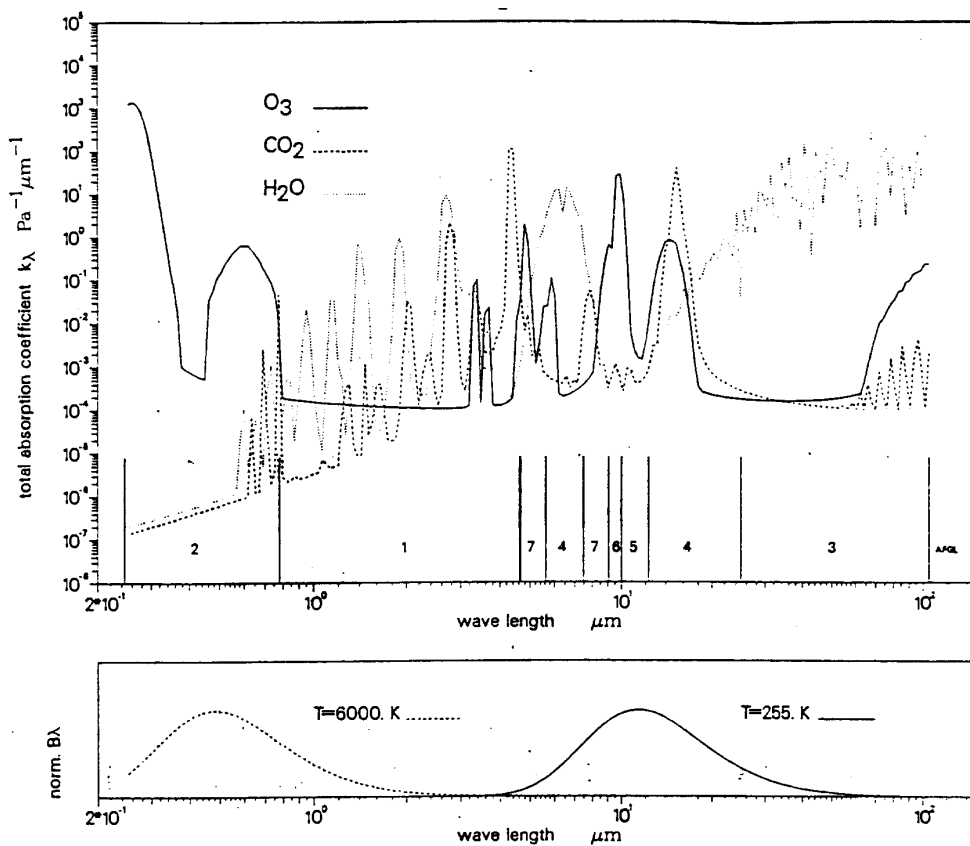
Figure 18. Absorption coefficients of H_2O, O_3 and uniformly mixed gases (indexed as CO_2) at different wavelengths and the normalized Planck functions at 6000 K and 255 K (bottom panel).

3.5 The spectral scattering by particles

A primary electromagnetic wave encountering a particle will excite a secondary wave originating at the particle's location. Such process can occur at all wavelengths covering the whole electromagnetic spectrum. The scattering efficiency will depend on the size, the geometrical shape and on the real part of its complex refractive index, whereas the absorption efficiency will essentially depends on the imaginary part of the refractive index. Particles in the atmosphere are generally at such distances from each other that the radiation originating from individual particles is incoherent (i.e., no interference betwwen scattered radiation from different particles). Therefore the field of scattered radiation due to an ensemble of particles is the sum of the fields from the individual scattering processes. Atmospheric constituents can be separated into different broad categories according to their size: Molecules have a typical radius of 10^{-4} μm, the so called aerosols range from 0.01 to 10 μm, cloud particles from 5 to 200 μm, rain drops and hail particles up to 10^{-2} m.

The relative intensity of the scattering pattern depends on the so-called Mie parameter $\alpha = 2\pi r / \lambda$ where r is the radius of the particle (assumed spherical) and λ is the wavelength.

3.5 (a) Rayleigh scattering. The size of air molecules is small compared to the wavelength of radiation in the Earth's atmosphere. So in a simple model one can assume that molecules interacting with an electromagnetic wave start to vibrate and thereby radiate as linear oscillators. By considering spherical air molecules statistically distributed in a volume, Lord Rayleigh derived (1871) the phase function of such molecules

$$P_R = \frac{3}{4}(1 + \cos^2\theta)$$

Rayleigh scattering being conservative ($\omega = 1$), the integral over the phase function is unity, i.e.,

$$\int_{4\pi} P(\theta) \, d\theta = 1 .$$

It is completely symmetric ($g = 0$) (see Fig. 19), and the scattering coefficient, i.e., the probability of a photon being scattered in a volume is for Rayleigh scattering proportional to the density of air and inversely proportional to the fourth power of the wavelength. The visible consequence of this spectral dependency is the blueness of the sky, caused by the preferential scattering of shorter wavelengths in a clear atmosphere. The rapid decrease of the Rayleigh scattering coefficient with wavelength simplifies the transfer problem for the Earth's atmosphere, since Rayleigh scattering can be completely neglected for the terrestrial part of the spectrum.

3.5 (b) Mie scattering. The size of aerosols and or cloud droplets is comparable to the wavelengths at which the radiative energy is dominant in the Earth's atmosphere. Rayleigh scattering is not applicable anymore. Photons encountering a particle off such size will excite secondary waves in various parts of the particles. These waves are coherent and therefore interference causes partial extinction in some directions and enhancement in others. For this reason, scattering by aerosols and cloud particles is far from being isotropic, with a pronounced preference for the forward direction. Under the assumption of spherical particle shape, Mie theory can be used to derive the phase function (see Subsection 3.2 (b)) for a given size distribution of particles. Unfortunately, there is no analytical solution and the result is obtained in the form of an infinite series of Bessel functions. A normalized phase function for a standard aerosol model (after Quenzel, 1985) is shown in Fig. 20.

For detailed calculations involving radiances (e.g., in remote sensing applications) the phase function is usually developed into Legendre polynomials with up to several hundred terms to get the true angular representation

$$p_v(\delta, \mu, \mu') = \omega_0 \sum (2l + 1)\psi_l P_l(\mu) P_l(\mu').$$

When dealing with the impact of scatterers on fluxes, only the very few terms necessary for an adequate description of the hemispherically integrated fluxes are required and one can use some analytic formula such as Henyey–Greenstein function

$$p_v(\delta, \mu, \mu') = \frac{1 - g^2}{1 + g^2 + 2g\mu\mu'}$$

where g is the asymmetry factor, the first moment of the expansion

$$g = \frac{1}{2} \int_{-1}^{+1} p(\delta, \mu, \mu')\mu \ d\mu.$$

When $g = -1$, all the energy is backscattered, $g = 1$ all energy appears in the forward direction, and $g = 0$ corresponds to an equipartition between the forward and backward spaces defined by a plane perpendicular to the incoming direction

In large-scale atmospheric models, a scattering medium (cloud or aerosols) is usually characterized by its single scattering albedo (see Subsection 3.2 (d)) and its phase function (see Subsection 3.2 (b)) and its optical thickness (see Subsection 3.2 (b)). For very large droplets the laws of geometric optics apply making the calculations very simple. In the Earth's atmosphere a large variety of droplet sizes can be found depending very much on the type of cloud they are embedded in. Stephens (1979) quotes radii ranging from 2.25 μm for stratus clouds to 7.5 μm for stratocumulus. Han et al. (1994) derived radii for water clouds from satellite measurements between 6 and 15 μm. Most radiative transfer schemes in use in GCMs reuiqre only the volume extinction coefficient (related to the optical thickness), the single scattering albedo and the forward scattered fraction of radiation (or asymmetry factor). All these quantities as given by Stephens (1979) are plotted in Figs. 21 to 24 for various cloud types.

The most complex calculation of the phase function is required for the treatment of ice crystals. The application of Mie theory is not possible since the assumption of a spherical shape is certainly invalidated in this case. Ice crystals take all sorts of shapes ranging from thin needles to complex combinations of hollow prisms forming snowflakes. If a specific shape is assumed for the ice crystals, geometrical optics may be used for particles that are large compared to the wavelength (Takano and Liou, 1989; Ebert and Curry, 1992; Fu and Liou, 1993; Fu et al., 1999, 1988, 1999). However, the results depend very much on the orientation of the crystals relative to the direction of propagation of the radiation. At present, it is almost impossible for a GCM-type radiation scheme to take into account such detailed and complicated dependencies of the optical properties, specially as the GCM is still far from providing the reuiqred information necessary to initiate such calculations.

In the cruder form of parametrization currently used, the ice water loading of the clouds is prognosed by the cloud scheme and thus provides an interactive optical thickness. The effective dimension of the particles is diagnosed from temperature and/or the type of process from which the cloud is originating (large-scale condensation or convection), but the single scattering albedo and asymmetry factor are specified.

rayleigh scattering phase function
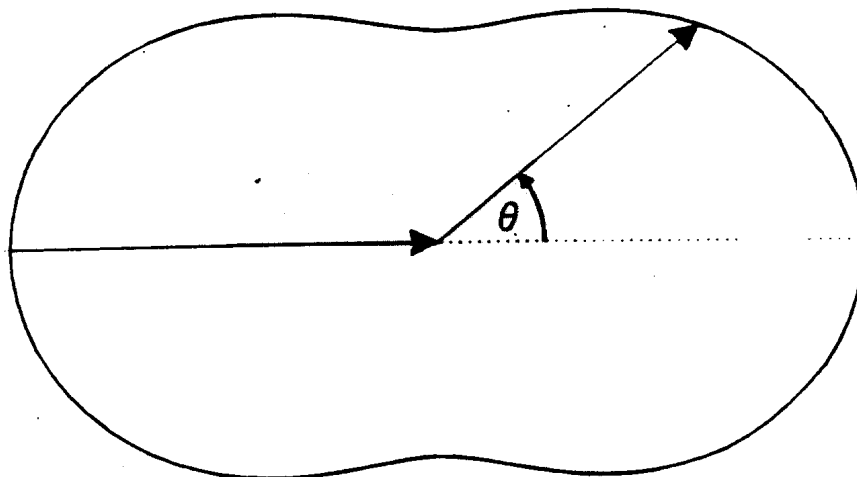
$$p(\theta) = \frac{3}{4} * (1 + \cos^2\theta)$$

Figure 19. Rayleigh phase function for a molecule located at the origin of the polar coordinate system. The probability of scattering in a certain direction is proportional to the length of the arrow for the outgoing beam.
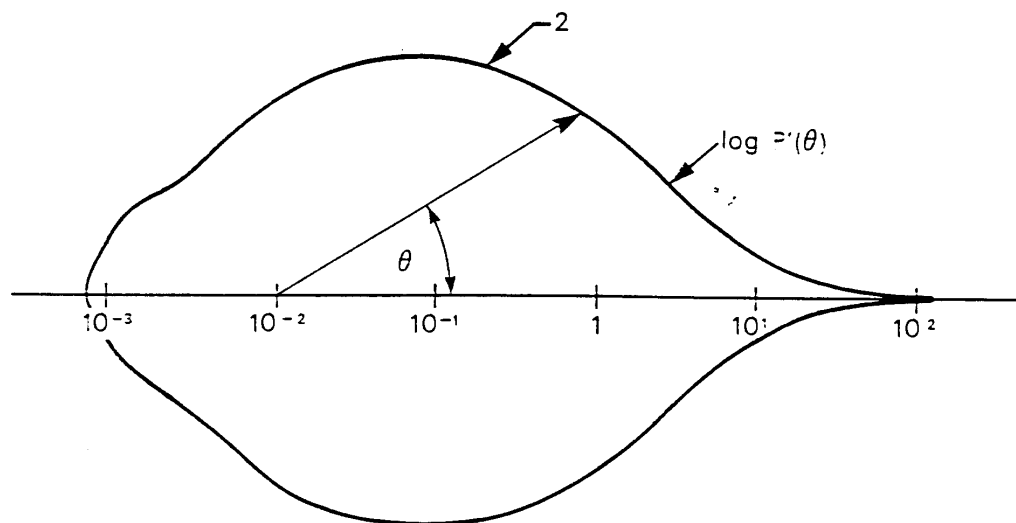

Figure 20. Normalized phase function in polar coordinates with logarithmic axis for a standard aerosol model. Note that the scattering is strongly dominated by the forward peak.
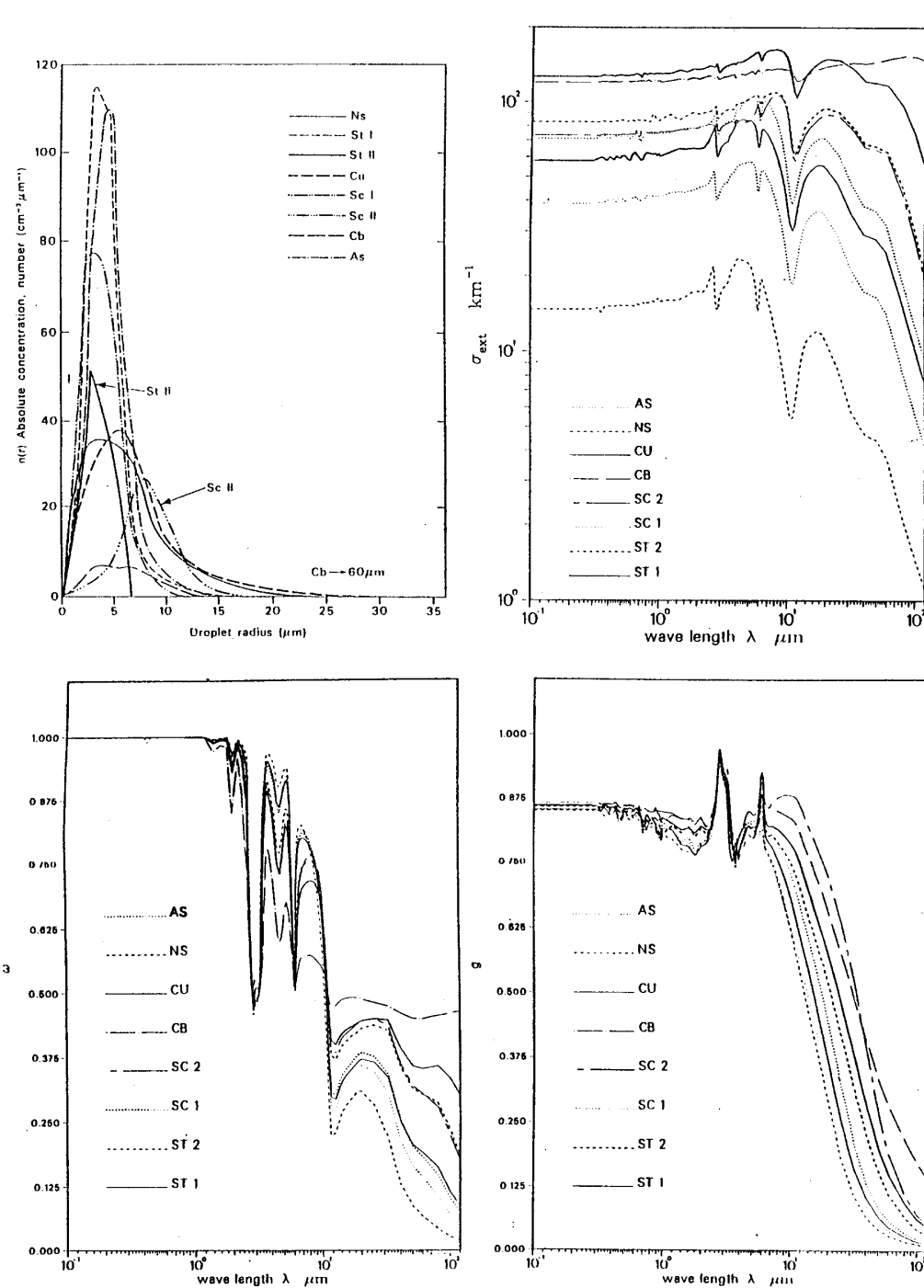
Figure 21. The droplet distribution of eight cloud models (after Stephens, 1979) [top left]

Figure 22. Wavelength dependency of the total extinction coefficient [top right]

Figure 23. Wavelength dependency of the single scattering albedo [bottom left]

Figure 24. Wavelength dependency of the asymmetry factor [bottom right]

4. RADIATION SCHEMES IN USE AT ECMWF

4.1 The operational longwave scheme (as of March 2000)

The longwave radiation is an upgrade from the original scheme defined by Morcrette et al. (1986), Morcrette (1990, 1991, 1993).

Assuming a non-scattering atmosphere in local thermodynamic equilibrium, $\mathcal{F}$ is given by

$$\mathcal{F} = \int_{-1}^{1} \mu \, d\mu \left[\int_{0}^{\infty} dv \left\{ \mathcal{L}_v(p_{\mathrm{surf}}, \mu) t_v(p_{\mathrm{surf}}, p, \mu) + \int_{p' = p_{\mathrm{surf}}}^{0} \mathcal{L}_v(p', \mu) dt_v \right\} \right] \tag{1}$$

where $\mathcal{L}_v(p, \mu)$ is the monochromatic radiance at wavenumber v at level p, propagating in a direction θ (the angle that this direction makes with the vertical), where $\mu = \cos\theta$ and $t_v(p, p'; r)$ is the monochromatic transmission through a layer whose limits are at p and p' seen under the same angle θ, with $r = \sec\theta$. The subscript 'surf' refers to the earth's surface.

After separating the upward and downward components (indicated by superscripts + and –, respectively), and integrating by parts, we obtain the radiation transfer equation as it is actually estimated in the longwave part of the radiation code

$$\mathcal{F}_v^{+}(p) = [B_v(T_{\mathrm{surf}}) - B_v(T_{0+})] t_v(p_{\mathrm{surf}}, p; r) + B_v(T(p)) + \int_{p' = p_{\mathrm{surf}}}^{p} t_v(p, p'; r) dB_v$$

$$\mathcal{F}_v^{-}(p) = [B_v(T_{\infty}) - B_v(T_{\mathrm{top}})] t_v(p, 0; r) + B_v(T(p)) + \int_{p' = p}^{0} t_v(p', p; r) dB_v \tag{2}$$

where, taking benefit of the isotropic nature of the longwave radiation, the radiance $\mathcal{L}_v$ of (5.3) has been replaced by the Planck function $B_v(T)$ in units of flux, W m^{-2} (here, and elsewhere, B_v is assumed to always includes the π factor). T_{surf} is the surface temperature, T_{0+} that of the air just above the surface, $T(p)$ is the temperature at pressure-level p, T_{top} that at the top of the atmospheric model. The transmission t_v is evaluated as the radiance transmission in a direction θ to the vertical such that $r = \sec\theta$ is the diffusivity factor (Elsasser, 1942).

The integrals in (2) are evaluated numerically, after discretization over the vertical grid, considering the atmosphere as a pile of homogeneous layers. As the cooling rate is strongly dependent on local conditions of temperature and pressure, and energy is mainly exchanged with the layers adjacent to the level where fluxes are calculated, the contribution of the distant layers is simply computed using a trapezoidal rule integration, but the contribution of the adjacent layers is evaluated with a two-point Gaussian quadrature, thus at the i-th level,

$$\int_{p' = p_{\mathrm{surf}}}^{p_i} t_v(p, p'; r) \, dB_v =$$

$$\sum_{l = 1}^{2} dB_v(l) w_l t_v(p_i, p_l; r) + \frac{1}{2} \sum_{j = 1}^{i - 2} dB_v(j) [t_v(p_i, p_j; r) + t_v(p_i, p_{j-1}; r)] \tag{3}$$

where p_l is the pressure corresponding to the Gaussian root and w_l is the Gaussian weight. $\mathrm{d}B_\nu(j)$ and $\mathrm{d}B_\nu(l)$ are the Planck function gradients calculated between two interfaces, and between mid-layer and interface, respectively.

The longwave spectrum is divided into six spectral regions.

1) $0 - 350 \ \mathrm{cm}^{-1}$ & $1450 - 1880 \ \mathrm{cm}^{-1}$

2) $500 - 800 \ \mathrm{cm}^{-1}$

3) $800 - 970 \ \mathrm{cm}^{-1}$ & $1110 - 1250 \ \mathrm{cm}^{-1}$

4) $970 - 1110 \ \mathrm{cm}^{-1}$

5) $350 - 500 \ \mathrm{cm}^{-1}$

6) $1250 - 1450 \ \mathrm{cm}^{-1}$ & $1880 - 2820 \ \mathrm{cm}^{-1}$

corresponding to the centres of the rotation and vibration-rotation bands of H_2O, the 15 μm band of CO_2, the atmospheric window, the 9.6 μm band of O_3, the 25 μm "window" region, and the wings of the vibration-rotation band of H_2O, respectively.

Integration of (2) over wavenumber ν within the $k - $ th spectral region gives the upward and downward fluxes as

$$\mathcal{F}_k^{\ +}(p) = \{B_k(T_{\mathrm{surf}}) - B_k(T_{0+})\}t_{B_k}\{r\,\mathcal{U}(p_{\mathrm{surf}}, p), T_{\mathcal{U}}(p_{\mathrm{surf}}, p)\} + B_k(T_p)$$

$$+ \int_{p'=p_{\mathrm{surf}}}^{p} t_{\mathrm{dB}_k}\{r\,\mathcal{U}(p, p'), T_{\mathcal{U}}(p, p')\}\mathrm{d}B_k \tag{4}$$

$$\mathcal{F}_k^{\ -}(p) = \{B_k(T_0) - B_k(T_\infty)\}t_{B_k}\{r\,\mathcal{U}(p, 0), T_{\mathcal{U}}(p, 0)\} - B_k(T_p)$$

$$- \int_{p'=p}^{0} t_{\mathrm{dB}_k}\{r\,\mathcal{U}(p', p), T_{\mathcal{U}}(p', p)\}\mathrm{d}B_k \tag{5}$$

The formulation accounts for the different temperature dependencies involved in atmospheric flux calculations, namely that on T_p, the temperature at the level where fluxes are calculated, and that on $T_{\mathcal{U}}$, the temperature that governs the transmission through the temperature dependence of the intensity and half-widths of the lines absorbing in the concerned spectral region.

The band transmissivities are non-isothermal accounting for the temperature dependence that arises from the wavenumber integration of the product of the monochromatic absorption and the Planck function. Two normalized band transmissivities are used for each absorber in a given spectral region: the first one for calculating the first right-hand-side. term in (2), involving the boundaries; it corresponds to the weighted average of the transmission function by the Planck function

$$t_B(\overline{Up}, T_p, T_u) = \frac{\int_{\nu_1}^{\nu_2} B_\nu(T_p) t_\nu(\overline{Up}, T_u) d\nu}{\int_{\nu_1}^{\nu_2} B_\nu(T_p) d\nu} \qquad (6)$$

the second one for calculating the integral term in (2) is the weighted average of the transmission function by the derivative of the Planck function

$$t_{dB}(\overline{Up}, T_p, T_u) = \frac{\int_{\nu_1}^{\nu_2} \{dB(T_p)/dT\} t_\nu(\overline{Up}, T_u) d\nu}{\int_{\nu_1}^{\nu_2} \{dB(T_p)/dT\} d\nu} \qquad (7)$$

where $\overline{Up}$ is the pressure weighted amount of absorber.

In the scheme, the actual dependence on T_p is carried out explicitly in the Planck functions integrated over the spectral regions. Although normalized relative to $B(T_p)$ or $dB(T_p)/dT$, the transmissivities still depend on T_u, both through Wien's displacement of the maximum of the Planck function with temperature and through the temperature dependence of the absorption coefficients. For computational efficiency, the transmissivities have been developed into Pade approximants

$$t(\overline{Up}, T_u) = \frac{\sum_{i=0}^{2} c_i U_{\text{eff}}^{i/2}}{\sum_{j=0}^{2} d_j U_{\text{eff}}^{j/2}} \qquad (8)$$

where $U_{\text{eff}} = r(\overline{Up}) \Psi(T_u, \overline{Up})$ is an effective amount of absorber which incorporates the diffusivity factor r, the weighting of the absorber amount by pressure $\overline{Up}$, and the temperature dependence of the absorption coefficients.

The function $\Psi(T_u, \overline{Up})$ takes the form

$$\Psi(T_u, \overline{Up}) = \exp[a(\overline{Up})(T_u - 250) + b(\overline{Up})(T_u - 250)^2] \qquad (9)$$

The temperature dependence due to Wien's law is incorporated although there is no explicit variation of the coefficients c_i and d_j with temperature. These coefficients have been computed for temperatures between 187.5 and 312.5 K with a 12.5 K step, and transmissivities corresponding to the reference temperature the closest to the pressure weighted temperature T_u are actually used in the scheme.

The effect on absorption of the Doppler broadening of the lines (important only for pressure lower than 10 hPa) is included simply using the pressure correction method proposed by Fels (1979) and incorporated by Giorgetta and Morcrette (1995).

The incorporation of the effects of clouds on the longwave fluxes follows the treatment discussed by *Washington and Williamson* (1977). Whatever the state of the cloudiness of the atmosphere, the scheme starts by calculating

the fluxes corresponding to a clear-sky atmosphere and stores the terms of the energy exchange between the different levels (the integrals in (5.4) Let $\mathcal{F}_0^+(i)$ and $\mathcal{F}_0^-(i)$ be the upward and downward clear-sky fluxes. For any cloud layer actually present in the atmosphere, the scheme then evaluates the fluxes assuming a unique overcast cloud of emissivity unity. Let $\mathcal{F}_n^+(i)$ and $\mathcal{F}_n^-(i)$ the upward and downward fluxes when such a cloud is present in the nth layer of the atmosphere. Downward fluxes above the cloud, and upward fluxes below the cloud, are assumed to be given by the clear-sky values

$$\mathcal{F}_n^+(i) = \mathcal{F}_0^+(i) \text{ for } i \le n$$
$$\mathcal{F}_n^-(i) = \mathcal{F}_0^-(i) \text{ for } i > n \tag{10}$$

Upward fluxes above the cloud ($\mathcal{F}_n^+(k)$ for $k \ge n + 1$) and downward fluxes below it ($\mathcal{F}_n^-(k)$ for $k > n$) can be expressed with expressions similar to (3) provided the boundary terms are now replaced by terms corresponding to possible temperature discontinuities between the cloud and the surrounding air

$$\mathcal{F}_n^+(k) = \{\mathcal{F}_{\text{cld}}^+ - B(n+1)\}t(p_k, p_{n+1}; r) + B(k) + \int_{p' = p_{n-1}}^{p_k} t(p_k, p'; r)\mathrm{d}B$$

$$\mathcal{F}_n^-(k) = \{\mathcal{F}_{\text{cld}}^- - B(n)\}t(p_k, p_n; r) + B(k) + \int_{p' = p_k}^{p_n} t(p_k, p'; r)\mathrm{d}B \tag{11}$$

where $B(i)$ is now the total Planck function (integrated over the whole longwave spectrum) at level i, and $\mathcal{F}_{\text{cld}}^+$ and $\mathcal{F}_{\text{cld}}^-$ are the longwave fluxes at the upper and lower boundaries of the cloud. Terms under the integrals correspond to exchange of energy between layers in clear-sky atmosphere and have already been computed in the first step of the calculations. This step is repeated for all cloudy layers. The fluxes for the actual atmosphere (with semi-transparent, fractional and/or multi-layered clouds) are derived from a linear combination of the fluxes calculated in previous steps with some cloud overlap assumption in the case of clouds present in several layers. Let N be the index of the layer containing the highest cloud, $C_{\text{cld}}(i))$ the fractional cloud cover in layer i, with $C_{\text{cld}}(0) = 1$ for the upward flux at the surface, and with $C_{\text{cld}}(N+1) = 1$ and $\mathcal{F}_{N+1}^- = \mathcal{F}_0^-$ to have the right boundary condition for downward fluxes above the highest cloud.

The maximum-random overlap assumption is operationally used in the ECMWF model, and the cloudy upward $\mathcal{F}^+$ and downward $\mathcal{F}^-$ fluxes are obtained as

$$\mathcal{F}^+(i) = \mathcal{F}_0^+(i) \qquad\qquad\qquad\qquad \text{for } i = 1$$

$$\mathcal{F}^-(i) = C_{\text{cld}}(i-1)\mathcal{F}_{i-1}^+(i) + \sum_{n=0}^{i-2} C_{\text{cld}}(n)\mathcal{F}_n^+(i) \prod_{l=n+1}^{i-1} \{1 - C_{\text{cld}}(l)\} \text{ for } 2 \le i \le N+1 \tag{12}$$

$$\mathcal{F}^+(i) = C_{\text{cld}}(N)\mathcal{F}_N^+(i) + \sum_{n=0}^{N-1} C_{\text{cld}}(n)\mathcal{F}_n^+(i) \prod_{l=n+1}^{N} \{1 - C_{\text{cld}}(l)\} \qquad \text{for } i \ge N+2$$

In case of semi-transparent clouds, the fractional cloudiness entering the calculations is an effective cloud cover equal to the product of the emissivity due to the condensed water and the gases in the layer by the horizontal coverage of the cloud layer, with the emissivity, ε_{cld}, related to the condensed water amount by

$$\epsilon_{\text{cld}} = 1 - \exp(-k_{\text{abs}} \mathcal{U}_{\text{LWP}}) \tag{13}$$

where k_{abs} is the condensed water mass absorption coefficient (in m^2kg^{-1}) following *Smith and Shi* (1992) for water clouds and Ebert and Curry (1992) for ice clouds.

4.2 The operational SW scheme

The rate of atmospheric heating by absorption and scattering of shortwave radiation is

$$\frac{\partial T}{\partial t} = \frac{g}{c_p}\frac{\partial \mathcal{F}_{\text{SW}}}{\partial p} \tag{14}$$

where $\mathcal{F}_{\text{SW}}$ is the net total shortwave flux (the subscript SW will be omitted in the remainder of this section).

$$\mathcal{F}(\delta) = \int_0^\infty d\nu \left[\int_0^{2\pi} d\phi \left\{ \int_{-1}^{+1} \mu \mathcal{L}_\nu(\delta, \mu, \phi) d\mu \right\} \right] \tag{15}$$

is the diffuse radiance at wavenumber ν, in a direction given by the azimuth angle, ϕ, and the zenith angle, θ, with $\mu = \cos\theta$. In (15), we assume a plane parallel atmosphere, and the vertical coordinate is the optical depth δ, a convenient variable when the energy source is outside the medium

$$\delta(p) = \int_p^0 \beta_\nu^{\text{ext}}(p')\, dp' \tag{16}$$

$\beta_\nu^{\text{ext}}(p)$ is the extinction coefficient, equal to the sum of the scattering coefficient β_ν^{sca} of the aerosol (or cloud particle absorption coefficient β_ν^{abs}) and the purely molecular absorption coefficient k_ν. The diffuse radiance L_ν is governed by the radiation transfer equation

$$\mu\frac{d\mathcal{L}_\nu(\delta, \mu, \phi)}{d\delta} = \mathcal{L}_\nu(\delta, \mu, \phi) - \frac{\varpi_\nu(\delta)}{4}P_\nu(\delta, \mu, \phi, \mu_0, \phi_0)\mathcal{E}_\nu^0\exp(-\delta/\mu_r)$$
$$-\frac{\varpi_\nu(\delta)}{4}\int_0^{2\pi} d\phi'\left\{\int_{-1}^{+1}\Phi_\nu(\delta, \mu, \phi, \mu', \phi')\mathcal{L}_\nu(\delta, \mu', \phi')d\mu'\right\} \tag{17}$$

$\mathcal{E}_\nu^0$ is the incident solar irradiance in the direction $\mu_0 = \cos\theta_0$, ϖ_ν is the single scattering albedo $(= \beta_\nu^{\text{sca}}/k_\nu)$ and $\Phi(\delta, \mu, \phi, \mu', \phi')$ is the scattering phase function which defines the probability that radiation coming from direction (μ', ϕ') is scattered in direction (μ, ϕ). The shortwave part of the scheme, originally developed by *Fouquart and Bonnel* (1980) solves the radiation transfer equation and integrates the fluxes over the whole shortwave spectrum between 0.2 and 4 μm. Upward and downward fluxes are obtained from the reflectance and transmittances of the layers, and the photon-path-distribution method allows to separate the parametrization of the scattering processes from that of the molecular absorption.

Solar radiation is attenuated by absorbing gases, mainly water vapour, uniformly mixed gases (oxygen, carbon dioxide, methane, nitrous oxide) and ozone, and scattered by molecules (Rayleigh scattering), aerosols and cloud particles. Since scattering and molecular absorption occur simultaneously, the exact amount of absorber along the photon path length is unknown, and band models of the transmission function cannot be used directly as in longwave radiation transfer (see Subsection 4.1). The approach of the photon path distribution method is to calculate

the probability $\Pi(\mathcal{U})d\mathcal{U}$ that a photon contributing to the flux $\mathcal{F}_{\text{cons}}$ in the conservative case (i.e., no absorption, $\omega_v = 1$, $k_v = 0$) has encountered an absorber amount between $\mathcal{U}$ and $\mathcal{U} + d\mathcal{U}$. With this distribution, the radiative flux at wavenumber v is related to $\mathcal{F}_{\text{cons}}$ by

$$\mathcal{F}_v = \mathcal{F}_{\text{cons}} \int_0^\infty \Pi(\mathcal{U}) \exp(-k_v \mathcal{U}) d\mathcal{U} \tag{18}$$

and the flux averaged over the spectral interval Δv can then be calculated with the help of any band model of the transmission function $t_{\Delta v}$

$$\mathcal{F} = \frac{1}{\Delta v} \int_{\Delta v} \mathcal{F}_v dv = \mathcal{F}_{\text{cons}} \int_0^\infty \Pi(\mathcal{U}) t_{\Delta v}(\mathcal{U}) dv \tag{19}$$

To find the distribution function $\Pi(\mathcal{U})$, the scattering problem is solved first, by any method, for a set of arbitrarily fixed absorption coefficients k_1, thus giving a set of simulated fluxes $\mathcal{F}_{k_1}$. An inverse Laplace transform is then performed on (4.19) (*Fouquart*, 1974). The main advantage of the method is that the actual distribution $\Pi(\mathcal{U})$ is smooth enough that (4.19) gives accurate results even if $\Pi(\mathcal{U})$ itself is not known accurately. In fact, $\Pi(\mathcal{U})$ need not be calculated explicitly as the spectrally integrated fluxes are

$$\mathcal{F} = \mathcal{F}_{\text{cons}} t_{\Delta v}(\langle \mathcal{U} \rangle) \qquad \text{in the limiting case of weak absorption}$$

$$\mathcal{F} = \mathcal{F}_{\text{cons}} t_{\Delta v}(\langle \mathcal{U}^{1/2} \rangle) \quad \text{in the limiting case of strong absorption}$$

where $\langle \mathcal{U} \rangle = \int_0^\infty \Pi(\mathcal{U}) \mathcal{U} d\mathcal{U}$ and $\langle \mathcal{U}^{1/2} \rangle = \int_0^\infty \Pi(\mathcal{U}) \mathcal{U}^{1/2} d\mathcal{U}$.

The atmospheric absorption in the water vapour bands is generally strong, and the scheme determines an effective absorber amount $\mathcal{U}_e$ between $\langle \mathcal{U} \rangle$ and $\langle \mathcal{U}^{1/2} \rangle$ derived from

$$\mathcal{U}_e = \ln(\mathcal{F}_{k_e}/\mathcal{F}_{\text{cons}})/k_e \tag{20}$$

where k_e is an absorption coefficient chosen to approximate the spectrally averaged transmission of the clear sky atmosphere

$$k_e = \frac{1}{\mathcal{U}_{\text{tot}}/\mu_0} \ln(t_{\Delta v}(\mathcal{U}_{\text{tot}}/\mu_0)) \tag{21}$$

where $\mathcal{U}_{\text{tot}}$ is the total amount of absorber in a vertical column and $\mu_0 = \cos\theta_0$. Once the effective absorber amounts of H_2O and uniformly mixed gases are found, the transmission functions are computed using Pade approximants

$$t_{\Delta v}(\mathcal{U}) = \frac{\displaystyle\sum_{i=0}^N a_i \mathcal{U}^{i-1}}{\displaystyle\sum_{j=0}^N b_j \mathcal{U}^{j-1}} \tag{22}$$

Absorption by ozone is also taken into account, but since ozone is located at low pressure levels for which molecular scattering is small and Mie scattering is negligible, interactions between scattering processes and ozone absorption are neglected. Transmission through ozone is computed using (22) where $\mathcal{U}_{O_3}$ the amount of ozone is

$$\mathcal{U}^{d}_{O_3} = M \int_{p}^{0} d\mathcal{U}_{O_3} \qquad \text{for the downward transmission of the direct solar beam}$$

$$\mathcal{U}^{u}_{O_3} = r \int_{p_s}^{0} d\mathcal{U}_{O_3} + \mathcal{U}^{d}_{O_3}(p_{surf}) \qquad \text{for the upward transmission of the diffuse radiation}$$

$r = 1.66$ is the diffusivity factor (see Subsection 4.1), and M is the magnification factor (*Rodgers,* 1967) used instead of r to account for the sphericity of the atmosphere at very small solar elevations

$$M = 35/\sqrt{\mu_0^2 + 1} \tag{23}$$

To perform the spectral integration, it is convenient to discretize the solar spectral interval into subintervals in which the surface reflectance can be considered as constant. Since the main cause of the important spectral variation of the surface albedo is the sharp increase in the reflectivity of the vegetation in the near infrared, and since water vapour does not absorb below 0.68 μm, the shortwave scheme considers two spectral intervals, one for the visible (0.2–0.68 μm), one for the near infrared (0.68–4.0 μm) parts of the solar spectrum. This cut-off at 0.68 μm also makes the scheme more computationally efficient, in as much as the interactions between gaseous absorption (by water vapour and uniformly mixed gases) and scattering processes are accounted for only in the near-infrared interval.

4.2 (a) Vertical integration. Considering an atmosphere where a fraction C_{cld}^{tot} (as seen from the surface or the top of the atmosphere) is covered by clouds (the fraction C_{cld}^{tot} depends on which cloud-overlap assumption is assumed for the calculations), the final fluxes are given as a weighted average of the fluxes in the clear sky and in the cloudy fractions of the column

$$\mathcal{F}^-(j) = C_{cld}^{tot} \, \mathcal{F}_{cld}^-(j) \; + (1 - C_{cld}^{tot}) \mathcal{F}_{clr}^-$$

where the subscripts 'clr' and 'cld' refer to the clear-sky and cloudy fractions of the layer, respectively. In contrast to the scheme of *Geleyn and Hollingsworth* (1979), the fluxes are not obtained through the solution of a system of linear equations in a matrix form. Rather, assuming an atmosphere divided into homogeneous layers, the upward and downward fluxes at a given layer interface j are given by

$$\mathcal{F}^-(j) = \mathcal{F}_0 \prod_{k=j}^{N} \mathcal{T}_{bot}(k)$$

$$\mathcal{F}^+(j) = \mathcal{F}^-(j)\mathcal{R}_{top}(j-1) \tag{24}$$

where $\mathcal{R}_{top}(j)$ and $\mathcal{T}_{bot}(j)$ are the reflectance at the top and the transmittance at the bottom of the jth layer. Computations of $\mathcal{R}_{top}$'s start at the surface and work upward, whereas those of $\mathcal{T}_{bot}$'s start at the top of the atmosphere and work downward. $\mathcal{R}_{top}$ and $\mathcal{T}_{bot}$ account for the presence of cloud in the layer

$$\mathcal{R}_{top} = C_{cld}\mathcal{R}_{cld} + (1 - C_{cld})\mathcal{R}_{clr}$$

$$\mathcal{T}_{bot} = C_{cld}\mathcal{T}_{cld} + (1 - C_{cld})\mathcal{T}_{clr} \tag{25}$$

where C_{cld} is the cloud fractional coverage of the layer within the cloudy fraction $C_{\text{cld}}^{\text{tot}}$ of the column.

4.2 (b) Cloudy fraction of the layer. $\mathcal{R}_{t_{\text{cdy}}}$ and $\mathcal{T}_{b_{\text{cdy}}}$ are the reflectance at the top and transmittance at the bottom of the cloudy fraction of the layer calculated with the Delta-Eddington approximation. Given δ_c, δ_a, and δ_g, the optical thicknesses for the cloud, the aerosol and the molecular absorption of the gases, respectively, and $(= k_e U)$, and g_c and g_a the cloud and aerosol asymmetry factors, $\mathcal{R}_{t_{\text{cdy}}}$ and $\mathcal{T}_{b_{\text{cdy}}}$ are calculated as functions of the total optical thickness of the layer

$$\delta = \delta_c + \delta_a + \delta_g \tag{26}$$

of the total single scattering albedo

$$\varpi^* = \frac{\delta_c + \delta_a}{\delta_c + \delta_a + \delta_g} \tag{27}$$

of the total asymmetry factor

$$g^* = \frac{\delta_c}{\delta_c + \delta_a} g_c + \frac{\delta_a}{\delta_c + \delta_a} \mathbf{g}_a \tag{28}$$

of the reflectance $\mathcal{R}_-$ of the underlying medium (surface or layers below the j th interface), and of the cosine of an effective solar zenith angle $\mu_{\text{eff}}(j)$ which accounts for the decrease of the direct solar beam and the corresponding increase of the diffuse part of the downward radiation by the upper scattering layers

$$\mu_{\text{eff}}(j) = [(1 - C_{\text{cld}}^{\text{eff}}(j))/\mu + r \, C_{\text{cld}}^{\text{eff}}(j)]^{-1} \tag{29}$$

with $C_{\text{cld}}^{\text{eff}}(j)$ the effective total cloudiness over level j

$$C_{\text{cld}}^{\text{eff}}(j) = 1 - \prod_{i = j+1}^{N} (1 - C_{\text{cld}}(i)E(i)) \tag{30}$$

and

$$E(i) = 1 - \exp\left[-\frac{(1 - \varpi_c(i)g_c(i)^2)\delta_c(i)}{\mu}\right] \tag{31}$$

$\delta_c(i)$, $\varpi_c(i)$ and $g_c(i)$ are the optical thickness, single scattering albedo and asymmetry factor of the cloud in the i th layer, and r is the diffusivity factor. The scheme follows the Eddington approximation first proposed by *Shettle and Weinman* (1970), then modified by *Joseph et al.* (1976) to account more accurately for the large fraction of radiation directly transmitted in the forward scattering peak in case of highly asymmetric phase functions. Eddington's approximation assumes that, in a scattering medium of optical thickness δ^*, of single scattering albedo ω, and of asymmetry factor g, the radiance $\mathcal{L}$ entering (15) can be written as

$$\mathcal{L}(\delta, \mu) = \mathcal{L}_0(\delta) + \mu \mathcal{L}_1(\delta) \tag{32}$$

In that case, when the phase function is expanded as a series of associated Legendre functions, all terms of order greater than one vanish when (15) is integrated over μ and ϕ. The phase function is therefore given by

$$P(\Theta) = 1 + \beta_1(\Theta)\mu$$

where Θ is the angle between incident and scattered radiances. The integral in (15) thus becomes

$$\int_0^{2\pi} d\phi' \left\{ \int_{-1}^{+1} P(\mu, \phi, \mu', \phi') \mathcal{L}(\mu', \phi') d\mu' \right\} = 4\pi(\mathcal{L}_0 + \pi\mathcal{L}_1) \tag{33}$$

where

$$g = \frac{\beta_1}{3} = \frac{1}{2}\int_{-1}^{+1} P(\Theta)\mu \ d\mu$$

is the asymmetry factor.

Using (33) in (15) after integrating over μ and dividing by 2π, we get

$$\mu\frac{d}{d\delta}(\mathcal{L}_0 + \mu\mathcal{L}_1) = -(\mathcal{L}_0 + \mu\mathcal{L}_1) + \varpi(\mathcal{L}_0 + g\mu\mathcal{L}_1) \\ +1/4\varpi\mathcal{F}_0\exp(-\delta/\mu_0)(1 + 3g\mu_0\mu) \tag{34}$$

We obtain a pair of equations for $\mathcal{L}_0$ and $\mathcal{L}_1$ by integrating (34) over μ

$$\frac{d\mathcal{L}_0}{d\delta} = -3(1-\varpi)\mathcal{L}_0 + \frac{3}{4}\varpi\mathcal{F}_0\exp(-\delta/\mu_0) \\ \frac{d\mathcal{L}_1}{d\delta} = -(1-\varpi g)\mathcal{L}_1 + \frac{3}{4}\varpi g\mu_0\mathcal{F}_0\exp(-\delta/\mu_0) \tag{35}$$

For the cloudy layer assumed non-conservative ($\varpi < 1$), the solutions to(4.35), for $0 \leq \delta \leq \delta^*$, are

$$\mathcal{L}_0(\delta) = C_1\exp(-K\delta) + C_2\exp(+K\delta) - \alpha\exp(-\delta/\mu_0) \\ \mathcal{L}_1(\delta) = P\{C_1\exp(-K\delta) - C_2\exp(+K\delta) - \beta\exp(-\delta/\mu_0)\} \tag{36}$$

where

$$K = \{3(1-\varpi)(1-\varpi g)\}^{1/2} \\ P = \{3(1-\varpi)/(1-\varpi g)\}^{1/2} \\ \alpha = 3\varpi\mathcal{F}_0\mu_0\{1 + 3g(1-\varpi)\}/\{4(1-K^2\mu_0^2)\} \\ \beta = 3\varpi\mathcal{F}_0\mu_0\{1 + 3g(1-\varpi)\mu_0^2\}/(4(1-K^2\mu_0^2))$$

The two boundary conditions allow to solve the system for C_1 and C_2; the downward directed diffuse flux at the top of the atmosphere is zero, i.e.,

$$\mathcal{F}^-(0) = \left[\mathcal{L}_0(0) + \frac{2}{3}\mathcal{L}_1(0)\right] = 0$$

which translates into

$$(1 + 2P/3)C_1 + (1 - 2P/3)C_2 = \alpha + 2\beta/3 \tag{37}$$

The upward directed flux at the bottom of the layer is equal to the product of the downward directed diffuse and direct fluxes and the corresponding diffuse and direct reflectance ($\mathcal{R}_d$ and $\mathcal{R}_-$, respectively) of the underlying medium

$$\mathcal{F}^+(\delta^*) = \left\{ \mathcal{L}_0(\delta^*) - \frac{2}{3}\mathcal{L}_1(\delta^*) \right\}$$

$$= \mathcal{R}_- \left\{ \mathcal{L}_0(\delta^*) + \frac{2}{3}\mathcal{L}_1(\delta^*) \right\} + \mathcal{R}_d \mu_0 \mathcal{F}_0 \exp(-\delta^*/\mu_0)$$

which translates into

$$\{ 1 - \mathcal{R}_- - 2(1 + \mathcal{R}_-)P/3 \}C_1 \exp(-K\delta^*)$$
$$+ \{ 1 - \mathcal{R}_- + 2(1 + \mathcal{R}_-)P/3 \}C_2(+ K\delta^*)$$
$$= \{ (1 - \mathcal{R}_-)\alpha - 2(1 + \mathcal{R}_-)\beta/3 + \mathcal{R}_d \mu_0 \mathcal{F}_0 \} \exp(-\delta^*/\mu_0) \tag{38}$$

In the Delta-Eddington approximation, the phase function is approximated by a Dirac delta function forward-scatter peak and a two-term expansion of the phase function

$$P(\theta) = 2f(1 - \mu) + (1 - f)(1 + 3g'\mu)$$

where f is the fractional scattering into the forward peak and g' the asymmetry factor of the truncated phase function. As shown by *Joseph et al.* (1976), these parameters are

$$f = g^2$$
$$g' = g/(g + 1) \tag{39}$$

The solution of the Eddington's equations remains the same provided that the total optical thickness, single scattering albedo and asymmetry factor entering (36) to (38) take their transformed values

$$\delta'^* = (1 + \varpi f)\delta^*$$
$$\omega' = \frac{(1 - f)\varpi}{1 - \varpi f} \tag{40}$$

Practically, the optical thickness, single scattering albedo, asymmetry factor and solar zenith angle entering (4.36) to (4.38) are δ^*, ϖ^*, g^* and μ_{eff} defined in (39) and (40).

4.2 (c) Clear-sky fraction of the layers. In the clear-sky part of the atmosphere, the shortwave scheme accounts for scattering and absorption by molecules and aerosols. The following calculations are practically done

twice, once for the clear-sky fraction ($1 - C_{cld}^{tot}$) of the atmospheric column with μ equal to μ_0, simply modified for the effect of Rayleigh and aerosol scattering, the second time for the clear-sky fraction of each individual layer within the fraction C_{cld}^{tot} of the atmospheric column containing clouds, with μ equal to μ_e.

As the optical thickness for both Rayleigh and aerosol scattering is small, $\mathcal{R}_{clr}(j-1)$ and $\mathcal{T}_{clr}(j)$, the reflectance at the top and transmittance at the bottom of the j th layer can be calculated using respectively a first and a second-order expansion of the analytical solutions of the two-stream equations similar to that of *Coakley and Chylek* (1975). For Rayleigh scattering, the optical thickness, single scattering albedo and asymmetry factor are respectively δ_R, $\varpi_R = 1$, and $g_R = 0$, so that

$$
\begin{aligned}
\mathcal{R}_R &= \frac{\delta_R}{2\mu + \delta_R} \\
\mathcal{T}_R &= \frac{2\mu}{(2\mu + \delta_R)}
\end{aligned}
\tag{41}
$$

The optical thickness δ_R of an atmospheric layer is simply

$$
\delta_R = \delta_R^* \{ p(j) - p(j-1) \} / p_{surf}
\tag{42}
$$

where δ_R^* is the Rayleigh optical thickness of the whole atmosphere parametrized as a function of the solar zenith angle (*Deschamps et al.,* 1983)

For aerosol scattering and absorption, the optical thickness, single scattering albedo and asymmetry factor are respectively δ_a, ϖ_a, with $1 - \varpi_a \ll 1$ and g_a, so that

$$
\begin{aligned}
den &= 1 + \{1 - \varpi_a + back(\mu_e)\varpi_a\}(\delta_a/\mu_e) \\
&\quad + (1 - \varpi_a)\{1 - \varpi_a + 2 back(\mu_e)\varpi_a\}(\delta_a^2 /\mu_a^2)
\end{aligned}
\tag{43}
$$

$$
\begin{aligned}
\mathcal{R}(\mu_e) &= \frac{(back(\mu_e)\varpi_a\delta_a)/\mu_a}{den} \\
\mathcal{T}(\mu_e) &= 1/den
\end{aligned}
\tag{44}
$$

where $back(\mu_e) = (2 - 3\mu_e g_a)/4$ is the backscattering factor.

Practically, $\mathcal{R}_{clr}$ and $\mathcal{T}_{clr}$ are computed using (41) and the combined effect of aerosol and Rayleigh scattering comes from using modified parameters corresponding to the addition of the two scatterers with provision for the highly asymmetric aerosol phase function through Delta-approximation of the forward scattering peak (as in (39) and (40))

$$
\begin{aligned}
\delta^+ &= \delta_R + \delta_a(1 - \varpi_a g_a^2) \\
g^+ &= \frac{g_a}{1 + g_a} \frac{\delta_a}{(\delta_R + \delta_a)} \\
\varpi^+ &= \frac{\delta_R}{\delta_R + \delta_a}\varpi_R + \frac{\delta_a}{\delta_R + \delta_a} \frac{\varpi_a(1 - g_a^2)}{1 - \varpi_a g_a^2}
\end{aligned}
\tag{45}
$$

As for their cloudy counterparts, $\mathcal{R}_{\text{clr}}$ and $\mathcal{T}_{\text{clr}}$ must account for the multiple reflections due to the layers underneath

$$\mathcal{R}_{\text{clr}} = \mathcal{R}(\mu_e) + \mathcal{R}_- \mathcal{T}(\mu_e)/(1 - \mathcal{R}^* \mathcal{R}_-) \tag{46}$$

and $\mathcal{R}_-$ is the reflectance of the underlying medium $\mathcal{R}_- = \mathcal{R}_t(j-1)$ and r is the diffusivity factor.

Since interactions between molecular absorption and Rayleigh and aerosol scattering are negligible, the radiative fluxes in a clear-sky atmosphere are simply those calculated from (24) and (41) attenuated by the gaseous transmissions (22).

4.2 (d) Multiple reflections between layers. To deal properly with the multiple reflections between the surface and the cloud layers, it should be necessary to separate the contribution of each individual reflecting surface to the layer reflectance and transmittances in as much as each such surface gives rise to a particular distribution of absorber amount. In case of an atmosphere including N cloud layers, the reflected light above the highest cloud consists of photons directly reflected by the highest cloud without interaction with the underlying atmosphere, and of photons that have passed through this cloud layer and undergone at least one reflection on the underlying atmosphere. In fact, (17) should be written

$$\mathcal{F} = \sum_{i=0}^{N} \mathcal{F}_{\text{cl}} \int_0^\infty \mathcal{P}_1(\mathcal{U}) t_{\Delta\nu}(\mathcal{U}) \text{d}\nu \tag{47}$$

where $\mathcal{F}_{\text{cl}}$ and $\mathcal{P}_1(\mathcal{U})$ are the conservative fluxes and the distributions of absorber amount corresponding to the different reflecting surfaces.

Fouquart and Bonnel (1980) have shown that a very good approximation to this problem is obtained by evaluating the reflectance and transmittance of each layer (using (34) and (40)) assuming successively a non-reflecting underlying medium ($\mathcal{R}_- = 0$), then a reflecting underlying medium ($\mathcal{R}_- \neq 0$). First calculations provide the contribution to reflectance and transmittance of those photons interacting only with the layer into consideration, whereas the second ones give the contribution of the photons with interactions also outside the layer itself.

From those two sets of layer reflectance and transmittances ($\mathcal{T}_{t0}$, $\mathcal{T}_{b0}$) and ($\mathcal{R}_{t\neq}$ $\mathcal{T}_{b\neq}$) respectively, effective absorber amounts to be applied to computing the transmission functions for upward and downward fluxes are then derived using (18) and starting from the surface and working the formulas upward

$$U_{e0}^- = \ln(\mathcal{T}_{b0}/\mathcal{T}_{bc})/k_e$$

$$U_{e\neq}^- = \ln(\mathcal{T}_{b\neq}/\mathcal{T}_{bc})/k_e$$

$$U_{e0}^+ = \ln(\mathcal{R}_{t0}/\mathcal{R}_{tc})/k_e \tag{48}$$

$$U_{e\neq}^+ = \ln(\mathcal{R}_{t\neq}/\mathcal{R}_{tc})/k_e$$

where $\mathcal{R}_{tc}$ and $\mathcal{T}_{bc}$ are the layer reflectance and transmittance corresponding to a conservative scattering medium.

Finally the upward and downward fluxes are obtained as

$$\mathcal{F}^{+}(j) = \mathcal{F}_0\{\mathcal{R}_{t0}t_{\Delta v}(\mathcal{U}_{e0}^{+}) + (\mathcal{R}_{t\neq} - \mathcal{R}_{t0})t_{\Delta v}(\mathcal{U}_{e\neq}^{+})\}$$

$$\mathcal{F}^{-}(j) = \mathcal{F}_0\{\mathcal{T}_{b0}t_{\Delta v}(\mathcal{U}_{e0}^{+}) + (\mathcal{T}_{b\neq} - \mathcal{T}_{b0})t_{\Delta v}(\mathcal{U}_{e\neq}^{-})\}$$

4.2 (e) Cloud shortwave optical properties. As seen in (36), the cloud radiative properties depend on three different parameters: the optical thickness δ_c, the asymmetry factor g_c, and the single scattering albedo ϖ_c.

Presently the cloud optical properties are derived from *Fouquart* (1987) for the water clouds, and *Ebert and Curry* (1992) for the ice clouds

δ_c is related to the cloud liquid water amount $\mathcal{U}_{LWP}$ by

$$\delta_c = \frac{3\,\mathcal{U}_{LWP}}{2r_e}$$

where r_e is the mean effective radius of the size distribution of the cloud water droplets. Presently r_e is parametrized as a linear function of height from 10 μm at the surface to 45 μm at the top of the atmosphere, in an empirical attempt at dealing with the variation of water cloud type with height. Smaller water droplets are observed in low-level stratiform clouds whereas larger droplets are found in mid-level cumuliform water clouds.

In the two spectral intervals of the shortwave radiation scheme, g_c is fixed to 0.865 and 0.910, respectively, and ω_c is given as a function of δ_c following *Fouquart* (1987)

$$\varpi_{c1} = 0.9999 - 5 \times 10^{-4}\exp(-0.5\delta_c)$$

$$\varpi_{c2} = 0.9988 - 2.5 \times 10^{-3}\exp(-0.05\delta_c)$$

(49)

These cloud shortwave radiative parameters have been fitted to in situ measurements of stratocumulus clouds (*Bonnel et al.*, 1983).

For the optical properties of ice clouds, we have

$$\delta_{ci} = IWP(a_i + b_i/r_e)$$

$$\varpi_i = c_i - d_i r_e$$

$$g_i = c_i + f_i r_e$$

(50)

where the coefficients have been derived from *Ebert and Curry* (1992) for the two intervals of the shortwave radiation scheme, and r_e is fixed at 40 μm.

5. COMPARISONS WITH OBSERVATIONS

As for the representation of clouds, there is an imperative need to perform at least some of the validation on short-time and limited space scales, before the drift in the GCM climate makes comparison with observations very difficult to interpret. Relative to other physical processes, the existence of reference models (LbLs) that have been or can be validated against highly spectrally detailed measurements (such as those of spectrometer and interferometer, present on ARM sites, or embarked on Nimbus-3) offers a very useful tool for validation. However, although currently done for LW, this approach is not really used for SW, because of the relative lack of highly spectrally detailed measurements in the SW compared to LW, and therefore of carefully validated LbL models in the SW (Ramas-

wamy and Freidenreich, 1992).

The approach discussed above could also be used, albeit with more difficulties, for cloudy atmospheres. However, for years, most of the validation effort for radiation transfer in cloudy atmospheres has dealt with comparison of radiation fluxes at TOA with satellite-derived fluxes (Nimbus-7 Earth Radiation Budget, Earth Radiation Budget Experiment). More often than not, this was often done without considering at the same time a validation of the cloud characteristics so that tweaking the cloud properties (particularly, the relationships giving the cloud fraction and cloud water loading in diagnostic cloud schemes) allowed an easy agreement with TOA fluxes, specially over monthly mean time-scales. With the availability of carefully calibrated measurements of the radiation fluxes at the surface (Baseline Station Radiation Network (*Ohmura et al*., 1998), Global Energy Balance Archive, NOAA-ARL SURFace RADiation network), or as is the case with the ARM program, of radiation fluxes and relatively detailed information on the state of the overlying atmosphere and some information on the cloud structure, systematic verification of the radiation fields produced by the ECMWF model at various stages in the forecasts can now be carried out.

In the following, we present one example of such validation for a site where good quality surface radiation measurements are available with a high frequency (such sites are available as part of the BSRN, SURFRAD or ARM projects). For a weather forecast system, it is often preferable to use measurements not too remote in time, as the analysis and forecast system undergoes regular improvement over the years. In this respect, the NOAA-ARL SURFace RADiation network offers real-time availability of surface radiation measurements over 6 sites in the U.S. Figure 5.1 compares the downward and upward LW radiation over Goodwin Creek, Mississippi, over the period 17 November to 15 December 1997, when a new physical parametrisation package was being tested. Fig. 26 shows the corresponding downward SW radiation. As can be seen from the LW comparisons, the model is rather successful at producing the observed variability in temperature at the surface (as seen from the upward LW radiation in Fig. 25 , bottom panel) and in temperature, humidity, and cloud fraction in the lowest layers of the atmosphere (as seen from the downward LW radiation in Fig. 25 , top panel). On the other hand, it appears less successful at handling the amount of condensed water in clouds, with too small optical thickness translating in too large downward SW radiation at the surface (Fig. 26). Next stage in this type of comparisons is to make sure that the fluxes are computed for the proper vertical profiles of radiatively important quantities. Albeit obvious, this statement is very difficult to be put in practice, as a comprehensive knowledge of all the atmospheric profiles is rarely attained (and attainable). The ARM program is the best try in this direction, with, over the South Great Plains site in Oklahoma, long time-series of surface radiation flux measurements, radiosoundings, synoptic observations, vertically integrated water vapour and cloud water measurements from a microwave radiometer, and vertical profiles of temperature, humidity, and cloud water from the inversion of interferometer and cloud radar measurements. Figure 5.3 presents the total column water vapour and cloud liquid water in December 1997 as observed by the Microwave Radiometer and produced by the ECMWF model in a series of 31 operational forecasts all starting at 12 UTC. Between the 13 and 17 December, the sky is essentially clear. Fig. 28 compares the surface downward LW radiation observed during these 5 days and computations by different radiation schemes from the forecast fields of temperature and humidity. A difference of 5 to 8 W m^{-2} is systematically found between the pre-December'97 ECMWF radiation scheme (old_EC) and the RRTM scheme. However, even this state-of-the-art radiation scheme underestimates the observed flux by 10–15 W m^{-2}, showing that, even this thought-to-be-simple comparison exercise is not straightforward. It is very likely that the model low-level temperature and humidity profiles are at the origin of these discrepancies.

Another validation exercise involving the model radiation scheme is the verification of the cloud signature on TOA radiances. Fig. 29 illustrates such comparison for the ERICA storm: the longwave window channel brightness temperature/radiance is simulated from the model cloud, temperature and humidity fields using the methodology of *Morcrette* (1991a).

Goodwin Creek, Mississippi
Surface Down LW: SURFRAD, ECMWF First Guess

Goodwin Creek, Mississippi
### Surface up LW: SURFRAD, ECMWF First Guess
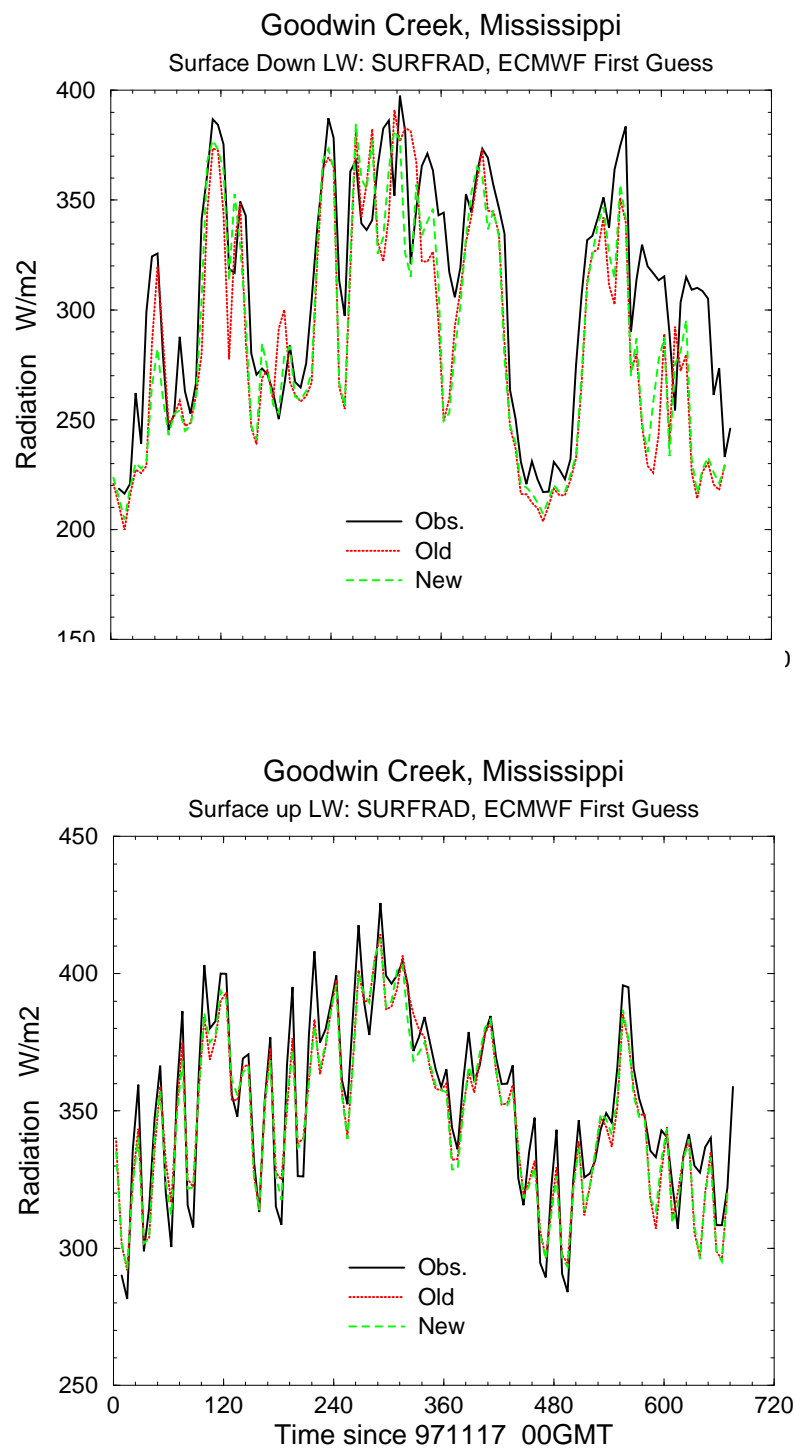
Figure 25. Downward (top) and upward LW radiation from the ECMWF 6-hour first-guess forecasts compared to the SURFRAD measurements in Goodwin Creek, Mississippi over the period 971117 00 UTC to 971215 00 UTC.

Goodwin Creek, Mississippi
Surface Down SW: SURFRAD, ECMWF First Guess
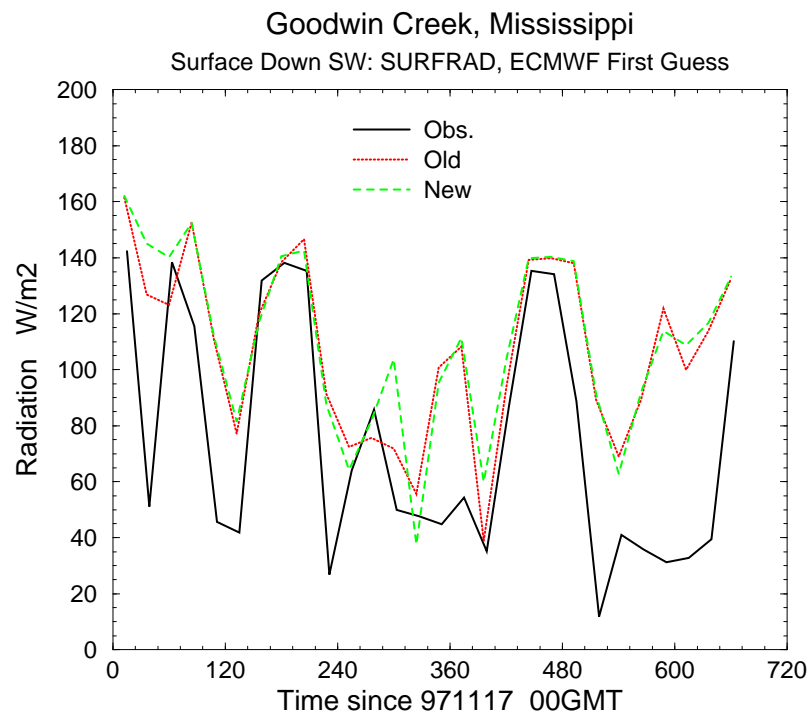
Figure 26. As in Fig. 25 , but for the downward SW radiation at the surface averaged over 24-hour periods.

SGP – Total column water vapour

ECMWF vs ARM–MWR – December 1997

SGP – Liquid water path

ECMWF vs ARM–MWR – December 1997
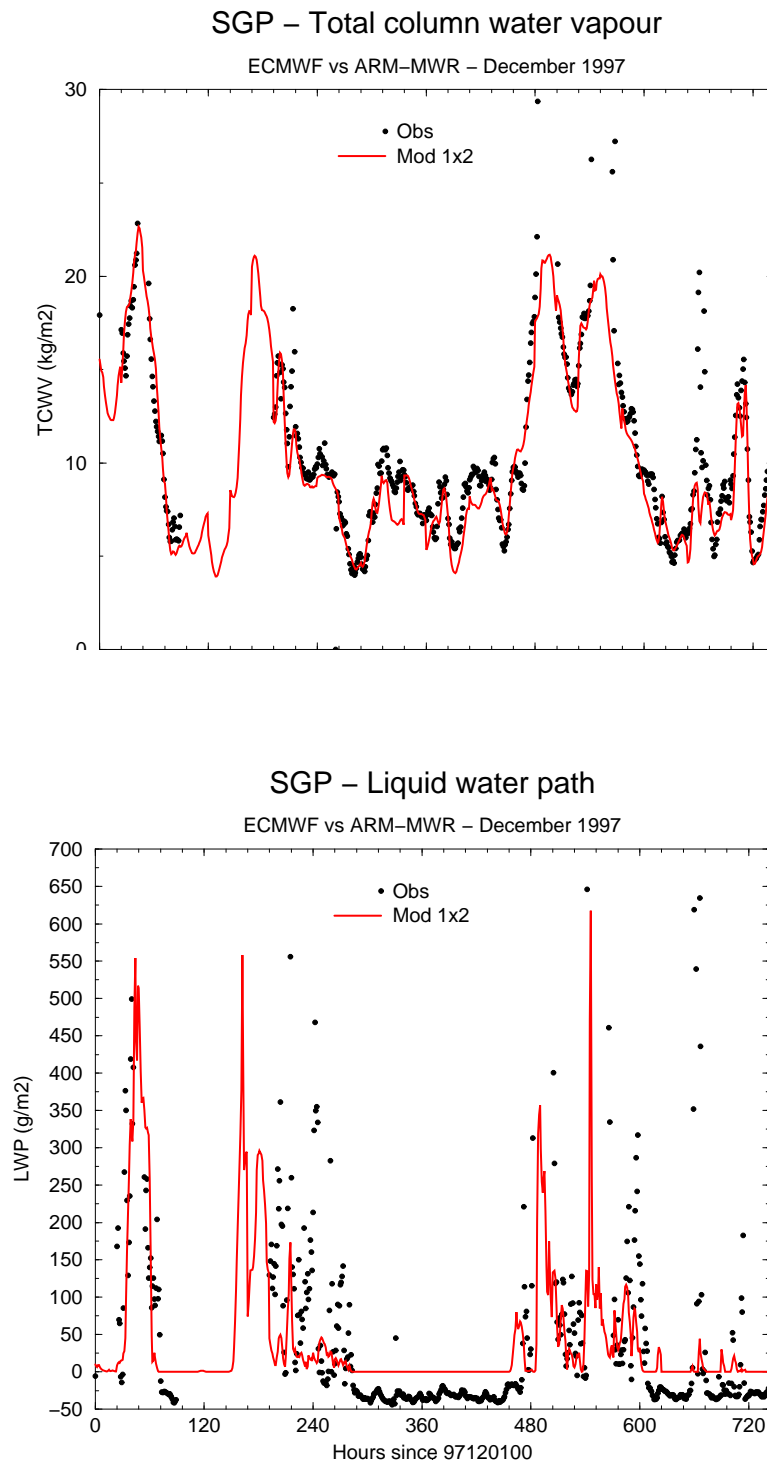
Figure 27. The total column water vapour (top) and total column cloud liquid water over the ARM-SGP site in December 1997 from a series of 31 forecasts all starting at 12 UTC. Points represent hourly averaged values of TCWV and TCCLW derived from Microwave Radiometer measurements.

ARM−SGP December 1997

ICRCCM−type comparison of Surface Downward LW Flux
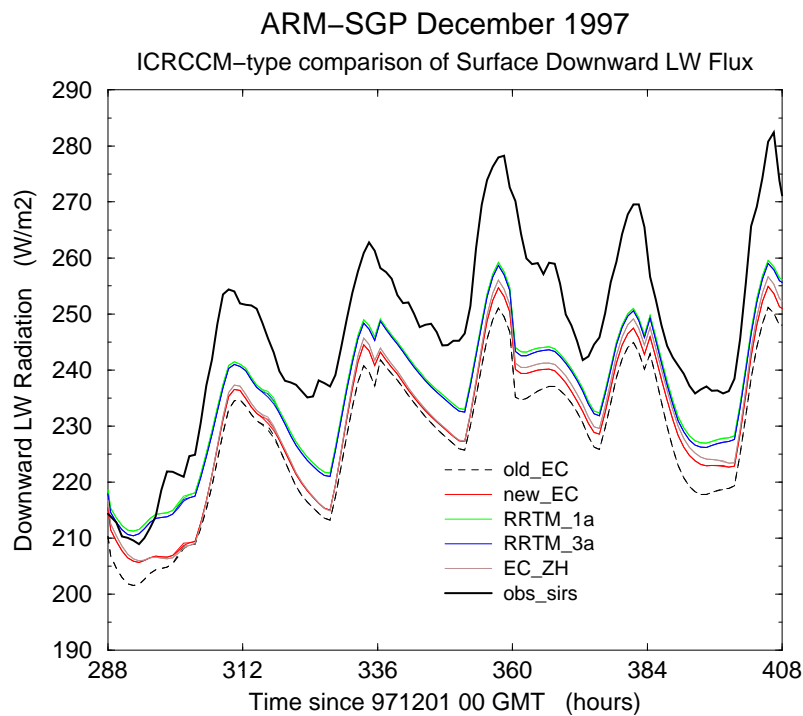
Figure 28. The surface downward LW radiation during 5 clear-sky days over the ARM-SGP site. The upper curve is the SIRS observation, the lower curves are computed by different radiation schemes from T and q fields operationally produced from forecasts between 12 and 35 hours, all starting at 12 UTC.
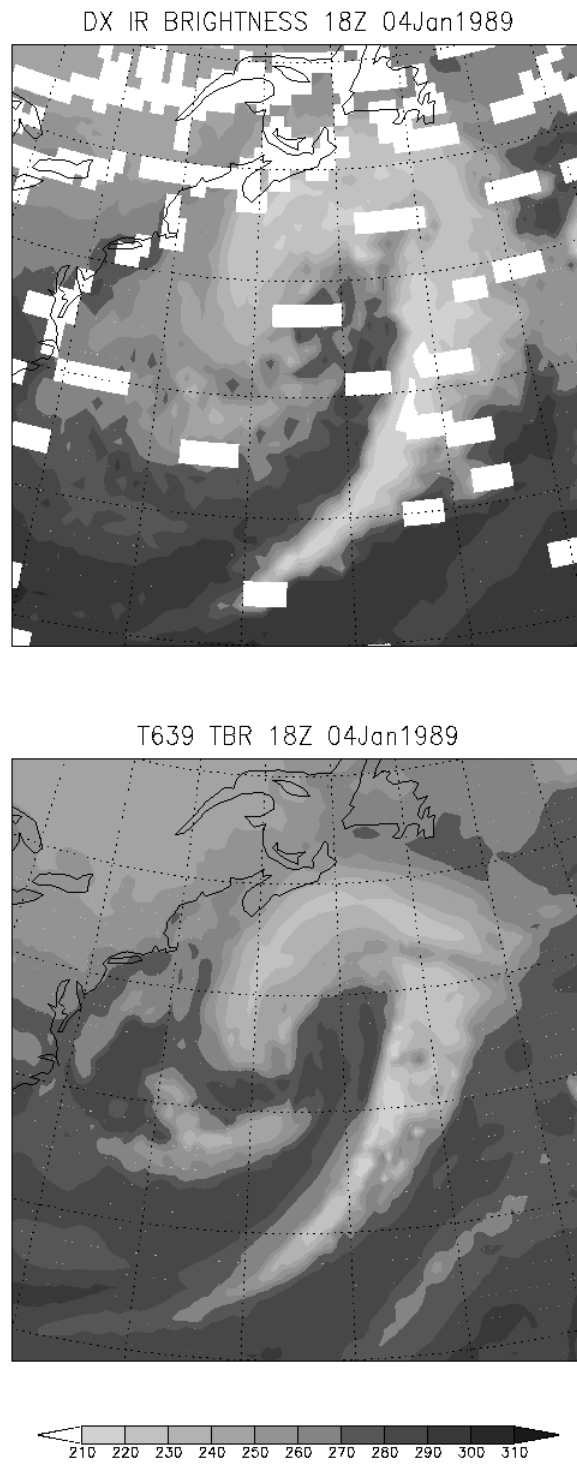
Figure 29. The GOES longwave window channel brightness temperature over the ERICA storm. Top panel is the ISCCP-DX image for 18 UTC 4 January 1989, bottom is the radiance simulated from the ECMWF $T_L 639$ model after a 18 hour forecast starting at 00 UTC 4 January 1989.

6. CONCLUSIONS AND PERSPECTIVES

Recent studies have focussed at the direct and/or indirect radiative impact of aerosols in climate simulations (*Joussaume*, 1990; *Genthon*, 1992; *Boucher and Lohmann*, 1995; *Chylek et al.*, 1995; *Mitchell et al.*, 1995; *Lohmann and Feichter*, 1997; *Tegen et al.*, 1997; *Timmreck et al.*, 1997; *Cusack et al.*, 1998; *Le Treut et al.*, 1998; *Schulz et al.*, 1998). Since the pioneering work of *Tanre et al.* (1984), the ECMWF model has included an annual mean, but geographically distributed climatology of aerosols. The geographical distribution of the maritime, continental, urban and desert aerosols are given in Figs. 30 and 31, where as the vertical distribution is illustrated in Fig. 32. As discussed in *Cusack et al.* (1998), the presence of these aerosols in the ECMWF model is certainly one of the reasons why the surface downward SW radiation is less overestimated in the ECMWF model than in other leading climate GCMs (*Garratt*, 1994; *Garratt et al.*, 1998). However, a monthly specification of the aerosol distributions or better a prognosed aerosol loading is a possible future development for the ECMWF model.

Recent studies by *Wang and Rossow* (1995, 1998) and *Stubenrauch et al.* (1997) have focussed at the potentially large impact on the atmospheric circulation linked to uncertainties in the vertical distribution of clouds and related radiative heating/cooling rates. Similar results were also obtained with the ECMWF model (*Morcrette and Jakob*, 2000). Fig. 33 presents the cloud overlaps that the operational radiation scheme can handle. One-dimensional calculations are performed for different cloud configurations often encountered in three-dimensional simulations. The first one corresponds to a typical convective system and includes a convective tower of fractional cover 0.15 from 820 to 290 hPa topped by stratiform anvil of cover 0.4 and 70 hPa thick. The second case includes three layers of stratiform cloud of cover 0.3 between 890 and 820 hPa (low-level), 640 and 545 hPa (middle-level), and 290 and 220 hPa (high-level), respectively. The profiles of the cloud longwave, shortwave and net radiative forcing for these two cases are presented in Fig. 34, left and right panels respectively. The cloud forcing term is simply the difference between the heating obtained for the cloudy atmosphere minus the clear-sky heating. The different COAs are treated exactly in the LW part and only approximately in the SW part of the radiation scheme. Therefore, the LW MRN and MAX results are essentially the same for case 1, and the same holds for the LW MRN and RAN results for case 2. In the SW, the agreement on the SW forcing profiles is also very good. In the first case (see Fig. 34, left panels), the anvil produces a strong LW cooling whereas a relative heating is found in the rest of the convective tower below. Compared to MRN/MAX, the RAN LW shows a smaller cooling peak in the anvil, smaller heating below within the tower, and larger warming in the clear PBL. All these features are consistent with the larger effective cloudiness that the RAN assumption produces between any two cloudy layers. This larger effective cloudiness (i) prevents the radiation from the lower atmospheric layers from escaping to space, thus the heating in the PBL, (ii) decreases the possible radiative exchanges within the tower, thus the smaller radiative heating, and (iii) decreases the upward LW flux at the base of the anvil, hence the smaller LW divergence in the anvil. Similarly, a stronger SW heating is linked in RAN to the larger cloud fraction available to screen the downward radiation and to the more diffuse character of this radiation in the cloudy fraction of the column. Consequently a smaller amount of SW radiation is available below the cloud base and this translates into a relative cooling. The smaller heating of the anvil in RAN is linked to the smaller SW flux divergence through a larger upward radiation due to the increased reflection on the larger effective amount of lower level clouds.

In the second case (see Fig. 34, right panels), each of the three stratiform cloud layers produces a LW cooling inside and a LW heating immediately underneath. Differences between MAX and MRN/RAN results are consistent with the smaller total effective cloudiness given by MAX. The cooling in the low-level cloud is reduced in MAX because the middle- and high-level clouds prevent the radiation at the top of the low-level cloud from escaping to space. Similarly, the cooling in the high-level cloud is increased in MRN/RAN because the low- and middle-level clouds prevent the warmer radiation from the lower layers to reach the base of the high-level cloud. The smaller total cloudiness in MAX also explains the smaller LW heating below the lowest cloud. In the SW, the difference in heating is very small within the clouds. The slightly larger relative cooling immediately below the clouds in MAX

comes from the larger fraction of radiation being directly transmitted, as, in MRN/RAN, the radiation in the cloudy fraction of the column is more diffuse and therefore more likely to be absorbed. The smaller SW heating of the upper cloud with MRN/RAN is again linked to the increased reflection. These one-dimensional computations show the validity of the treatment of the different COAs in the ECMWF radiation scheme. They also show the larger impact of a change of COA on the LW than on the SW radiative profiles.

Fig. 35 presents the total cloudiness (TCC) averaged over the last three months (DJF) of the EPR simulations with the MRN, MAX and RAN COAs. Not surprisingly, the set of MAX simulations display the minimum total cloud cover at 0.609, followed by the MRN at 0.639, whereas the RAN simulations have a much larger total cloud cover at 0.714. The increase from MRN to RAN (respectively, the decrease from MRN to MAX) is apparent over most of the globe, but is more pronounced over the sub-tropics, particularly those of the Southern hemisphere. Are these changes simply reflecting the different geometrical distribution of the cloud elements on the vertical or are they linked to actual changes in the volume of the cloud elements? A simple check whether the cloud volume is actually modified is obtained by diagnosing the total cloud cover for all sets of simulations and applying the operational maximum-random overlap assumption to the various cloud elements. Fig. 36 presents the MRN-equivalent TCC for the EPR experiments. The main result is that most of the change in TCC is not reflected in the MRN-equivalent TCC, showing that a large fraction of the signal is due to the geometrical overlapping in the radiation scheme, and not to a real significant change in the cloud volume.

Radiation transfer parametrisation is generally the most expensive in computer time among the physical parametrisations used in a GCM. In the ECMWF operational forecast model, full radiation computations are performed only every 3 hours and on a reduced grid (1 point out of 4 along the longitude direction). Even so, radiation accounts for about 15%t of the total cost of the model. Although such spatial and temporal sampling of the radiation forcing does not appear detrimental on the short time scales encompassed in the operational analyses of meteorological observations and the 10-day forecasts made with the high resolution (T_L319) ECMWF weather forecast model (Fig. 37 for the anomaly correlation of the geopotential at 500 hPa, Figs. 38 and 39 for the mean error in temperature at 850, 500, 200 and 50 hPa), the impact becomes systematic and (possibly) detrimental on seasonal time-scales and/or at lower resolution (*Morcrett*e, 2000). For example, Figures 6.11 and 6.12 present the zonal mean cloudiness and temperature, with the operational configuration (S4T3h = spatial sampling 1 point out of 4 in the tropics, full radiation calculation only every 3 hours), and the difference with configurations for which radiation is either called at every grid point (S1) and/or for every time step (T1). When the radiation calculations are synchronous with the rest of the physics (and of the model), the stability in the ITCZ is decreased, with a resultant (small) increase in high-level clouds (Fig. 40), but a more spatially extensive decrease in stratospheric temperatures (Fig. 41).

New algorithms are being tested based on the neural network approach of *Cheruy et al.* (1996) and *Chevallier et al.* (2000a, 2000b), or on the linearized approach proposed by *Chou and Neelin* (1996), both of which introduce major savings in computer time. They would therefore allow for more frequent and/or non spatially sampled radiation calculations. For example, Fig. 42 present the bias and standard deviation of the LW cooling rates computed by a neural network method relative to the operational LW scheme, whereas. Figs. 43 and 44 display standard objective scores, the anomaly correlation of the geopotential at 500 hPa (Fig. 43) and the mean error in temperature at various levels in the atmosphere (Fig. 44). Such results indicate that the neural network approach is potentially a viable replacement. for traditional LW parametrizations.

Other areas of development concern the role of the cloud inhomo/heterogeneity on the model horizontal sub-grid scale, and that of the vertical overlapping of cloud layers. On the first point, (not equivalent to a full account of the three-dimensional cloud-induced radiative effects, but going away from the plane-parallel approach used over the last 25 years), *Tiedtke* (1996) proposed a simple parametrisation of this effect, while *Barker* (1996, 1998) modified a SW scheme similar to the ECMWF one and incorporated an approximate treatment of the impact of the liquid

water inhomogeneities via a gamma-distribution approach. Figs. 45 and 46 present the differences in transmissivity, reflectivity and absorptivity for some standard liquid and ice water clouds in the two spectral intervals of the SW scheme. The impact is important over most of the range of optical thickness and for all quantities. Such an "horizontal" effect, to be accounted for also in the LW part of the spectrum is likely to change the effect of the clouds on the radiative distribution within the whole atmospheric column. In view of the large effects of the sub-grid scale distribution of the condensed water on the radiative fluxes, it is likely that, in the coming years, GCMs will incorporate an equation to at least diagnose this sub-grid scale variability and account for its effect on the radiation fields.

Up to now, the validation of the large-scale radiative fields produced by a climate or a weather forecast GCM has mainly consisted of checks on the total cloud cover, and related top of the atmosphere and surface longwave and shortwave radiation fields. These fields (for example, *Darnell et al.*, 1992; *Gupta et al.*, 1993; *Laszlo and Pinker*, 1993; *Li and Leighton*, 1993; *Rossow*, 1993; *Zhang et al.*, 1995) are provided by dedicated satellite observations such as ERB (*Stowe et al.*, 1989), ERBE (*Harrison et al.*, 1988), ScaRaB (*Kandel et al.*, 1998), CERES (*Wielicki et al.*, 1996) and/or operational satellite observations as part of ISCCP (*Rossow et al.*, 1987). Although very useful, these essentially two-dimensional (3-D if time history is considered) validation efforts are only a first step towards what would really be required to ascertain the adequacy of the representation of the cloud-radiation interactions: the 4-dimensional distribution of cloud volume and cloud water loading together with relevant 4-dimensional radiation parameters: a real challenge for the future!

Climatological Aerosols in the ECMWF Forecast System
Relative Weight
Maritime
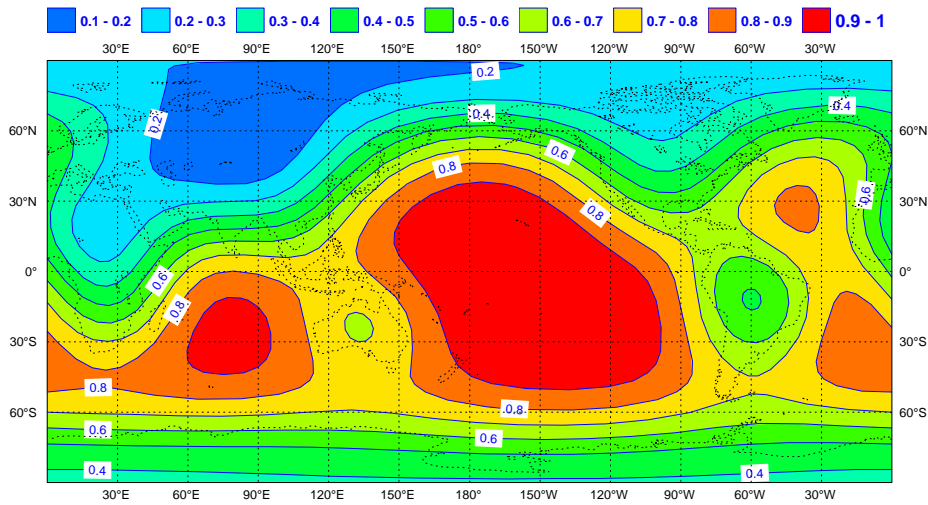
Climatological Aerosols in the ECMWF Forecast System
**Relative Weight**
Continental
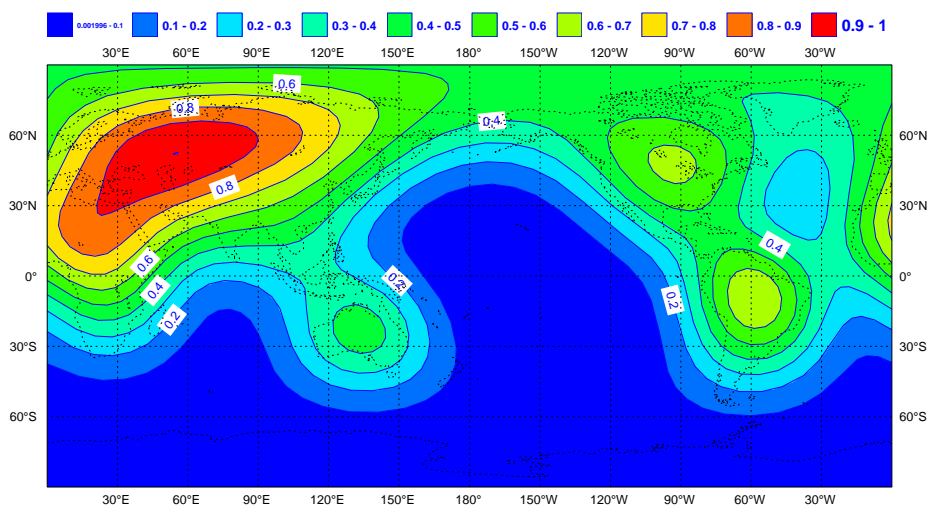
Figure 30. The annual mean climatological distribution of maritime and continental aerosols in the ECMWF operational system. The relative weight has to be multiplied by the optical thickness, i.e., 0.05 for maritime, and 0.2 for continental aerosols.

Climatological Aerosols in the ECMWF Forecast System
Relative Weight
Urban
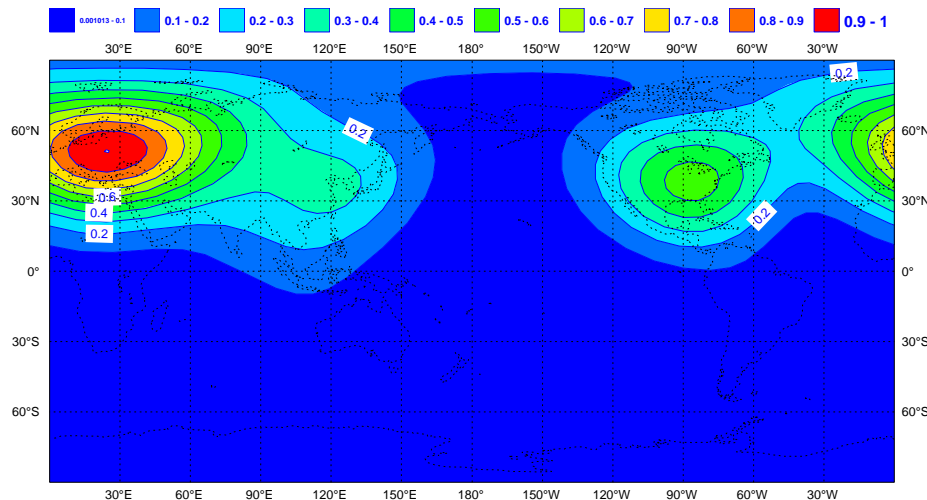
Climatological Aerosols in the ECMWF Forecast System
Relative Weight
Desert
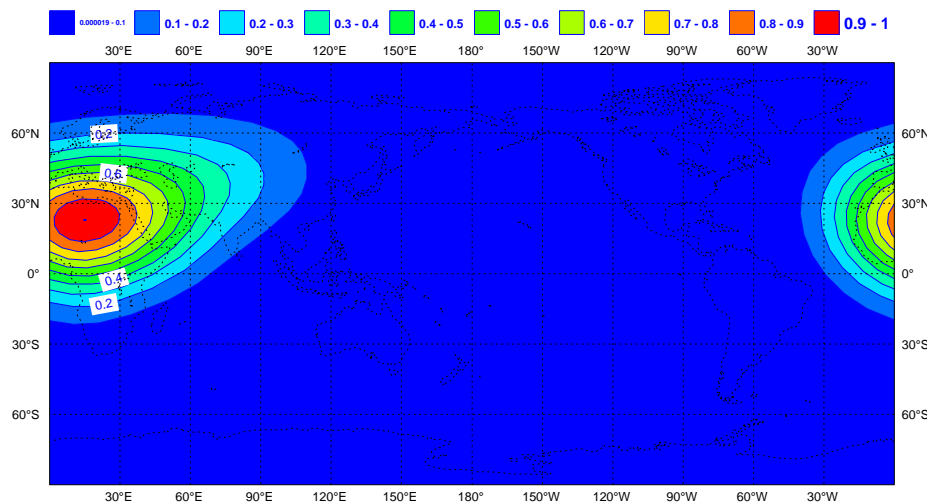
Figure 31. As in Fig. 30 , but for the urban and desert-type aerosols. Relevant optical thickness is 0.1 for urban, and 1.9 for desert aerosols.

Relative Vertical Distribution of Aerosol Types
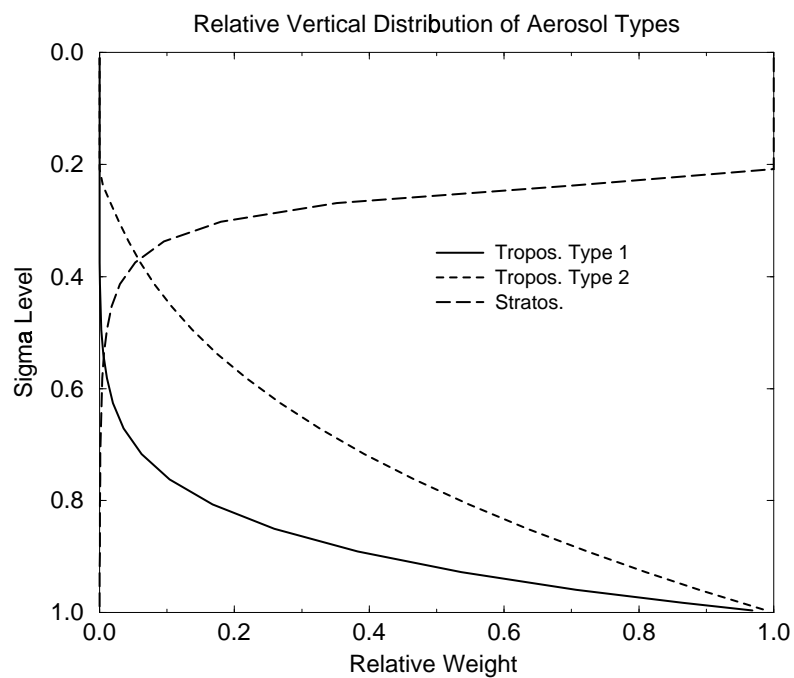
Figure 32. The vertical distribution of aerosols. Urban aerosols follow type 1 distribution, all other tropospheric aerosols follow type 2.
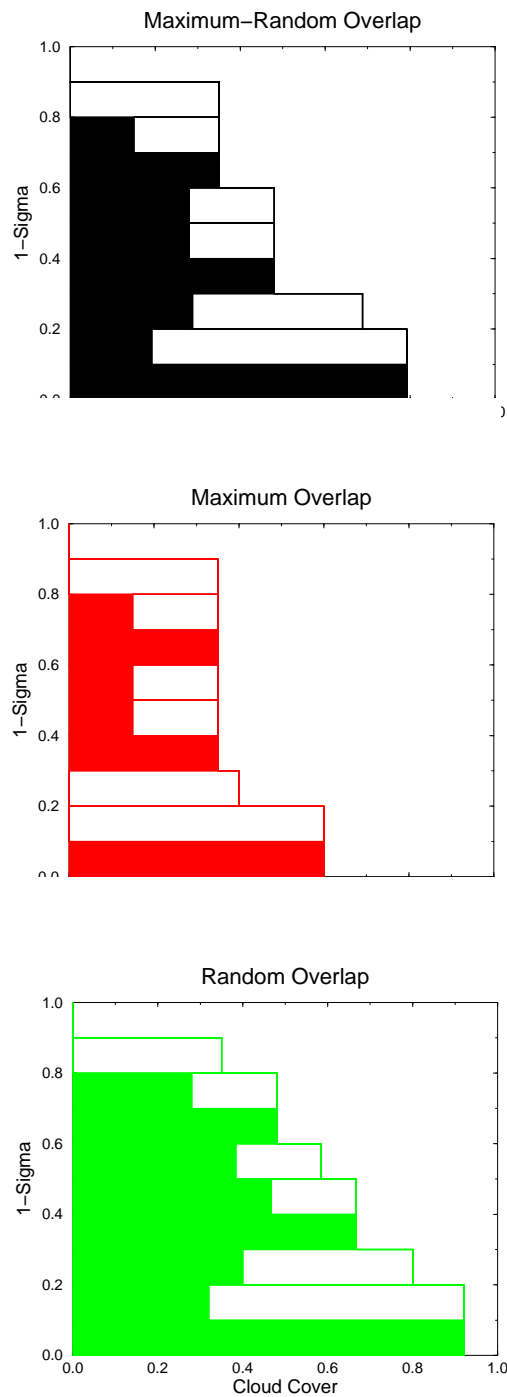
Figure 33. Schematics of the various cloud overlap assumptions used in this study. The clouds are shown as rectangular blocks filling the vertical extent of a layer. The total cloud fraction from the top of the atmosphere down to a given level is given by the line on the right delineating the clouds and the shaded area below them. The cloud overlap configurations are, from top to bottom, the maximum-random, maximum, and random cloud overlap.
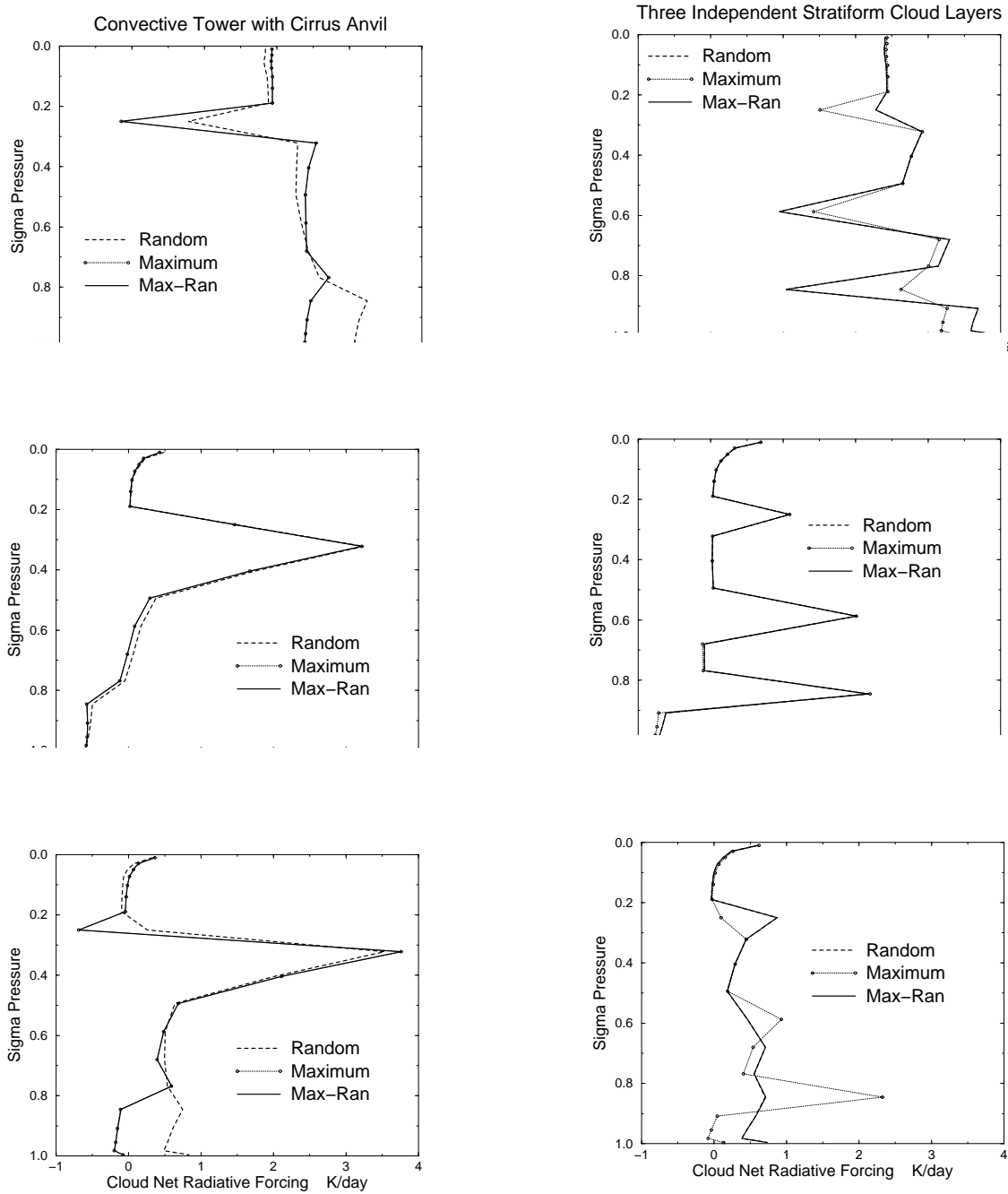
Figure 34. The longwave (top), shortwave (middle), and net cloud radiative forcing profiles for an atmosphere with a anvil-topped convective tower (left panels) and three independent stratiform cloud layers (right panels).

Impact of Cloud Overlap Assumption: EPR
Total Cloud Cover %   Between 3024- 720 Hours
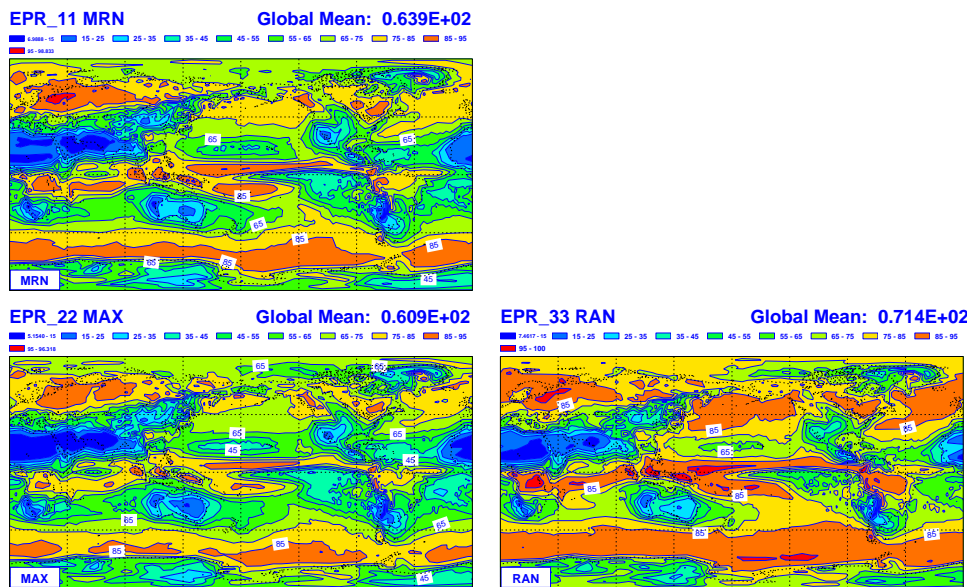
Figure 35. The total cloudiness (TCC) averaged over the last three months (DJF) of the RAD simulations with the maximum-random (MRN), maximum (MAX) and random (RAN) cloud overlap assumption (COA).

Impact of Cloud Overlap Assumption: EPR
Total Cloud Cover seen as MRN %   Between 3024- 720 Hours
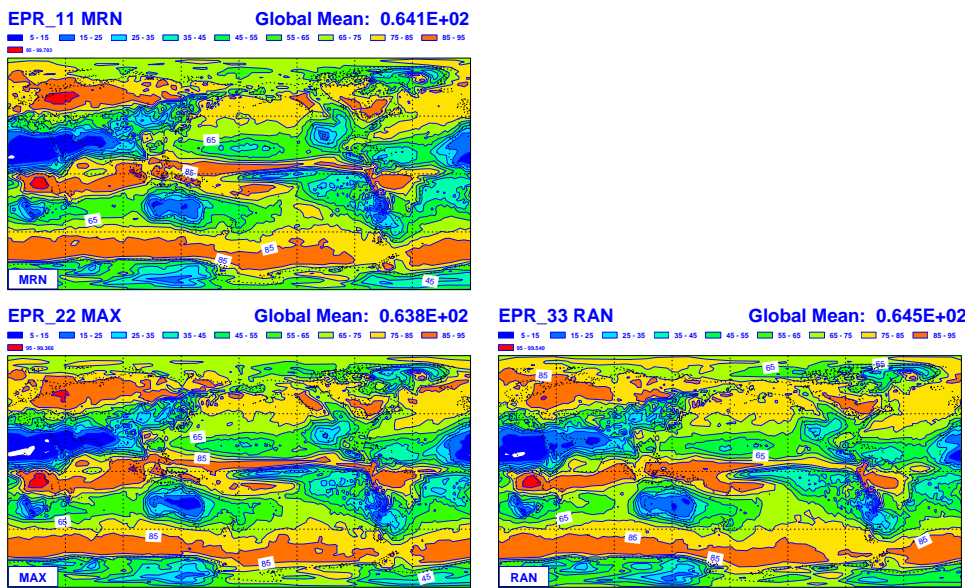
Figure 36. The maximum-random-equivalent total cloudiness of the simulations with the MRN, MAX and RAN COAs
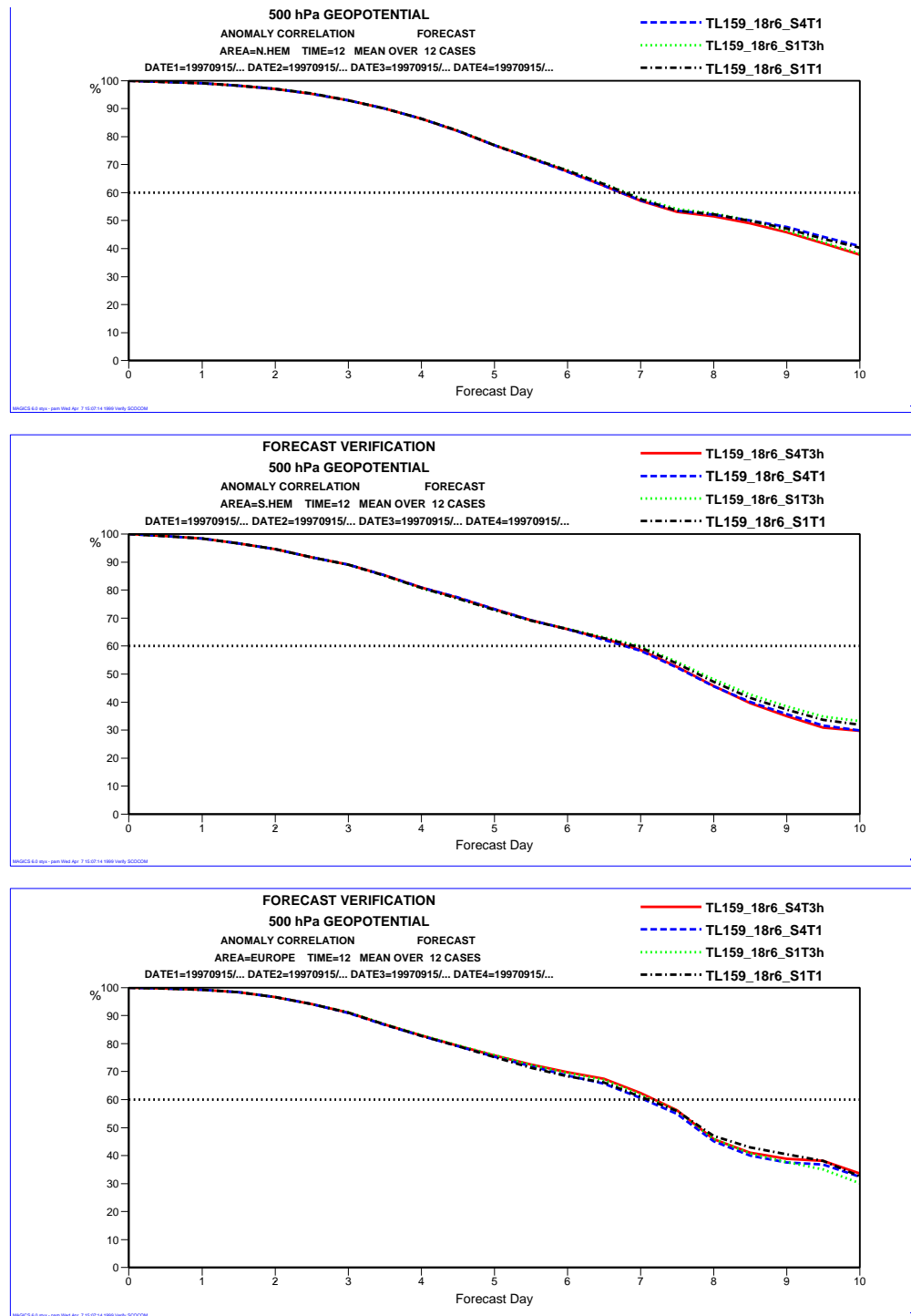
Figure 37. The anomaly correlation of the geopotential at 500 hPa for the various time-space configurations for the Northern (top panels) and Southern (middle panels) hemispheres, and the tropical region (bottom panels). Full line is S4T3h, long dash line is S4T1, dotted line is S1T3h, and dot-dash line is S1T1.
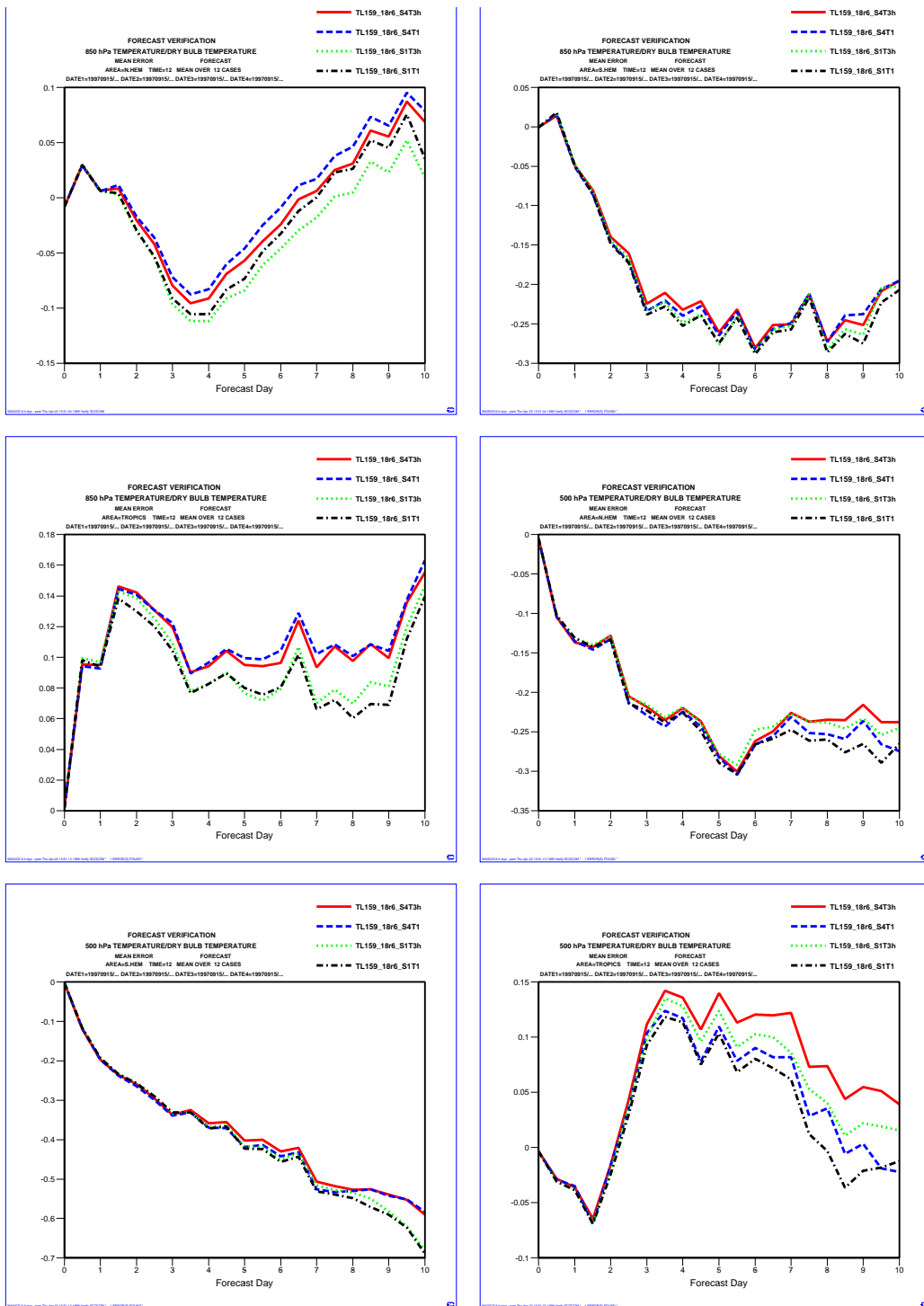
Figure 38. The mean error of the temperature at 850 and 500 hPa for the various time-space configurations for the Northern and Southern hemispheres, and the tropical region. Panels are read from left to right, and top to bottom.
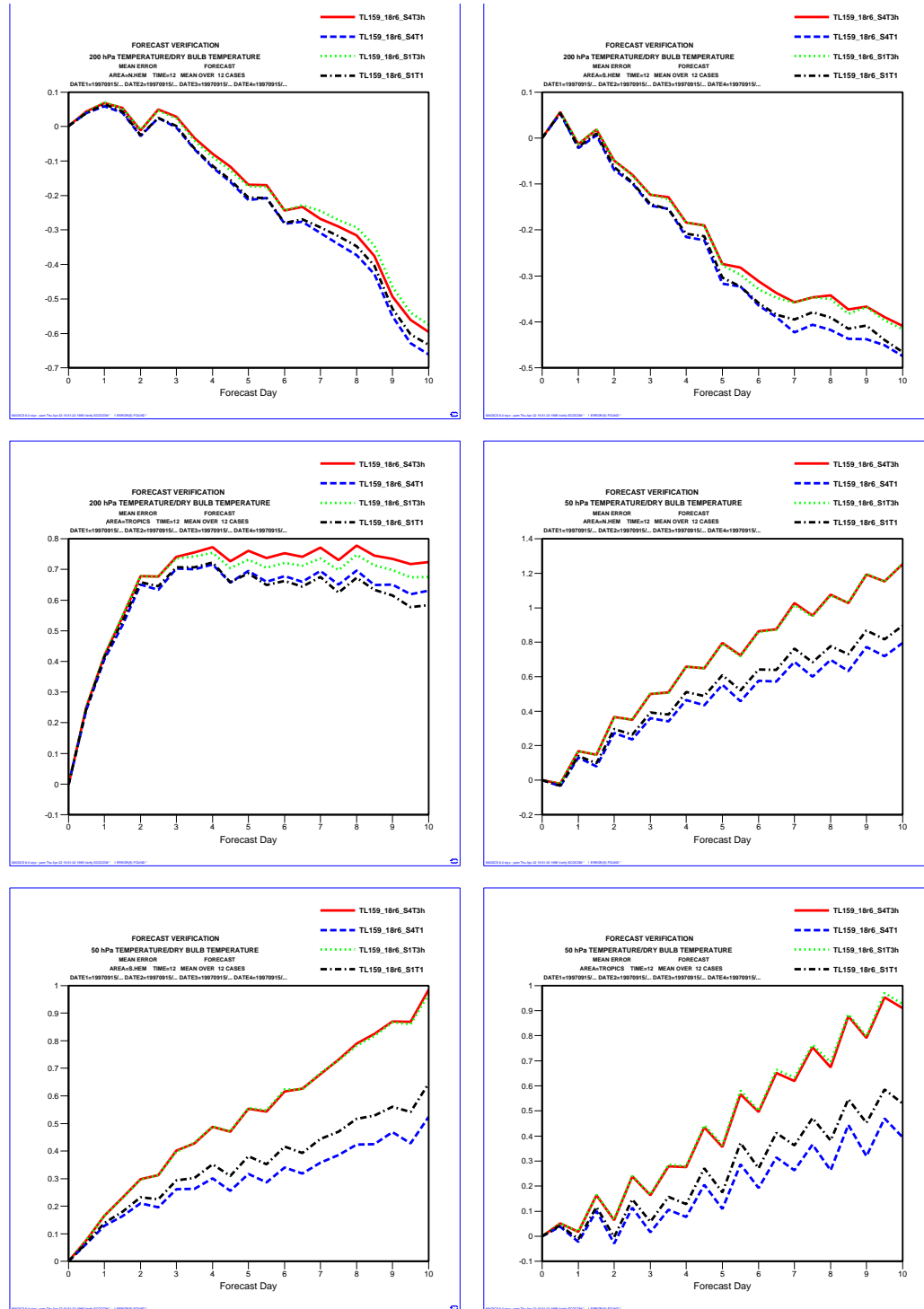
Figure 39. As in Fig. 38 , but for the mean error of the temperature at 200 and 50 hPa.

Time-Space Interpolation: REF
ECMWF TL95 L31: 4/3h, 4/1, 1/3h, 1/1
8706-8708 Cloud Fraction (%) Zonal M Diff. to OPE
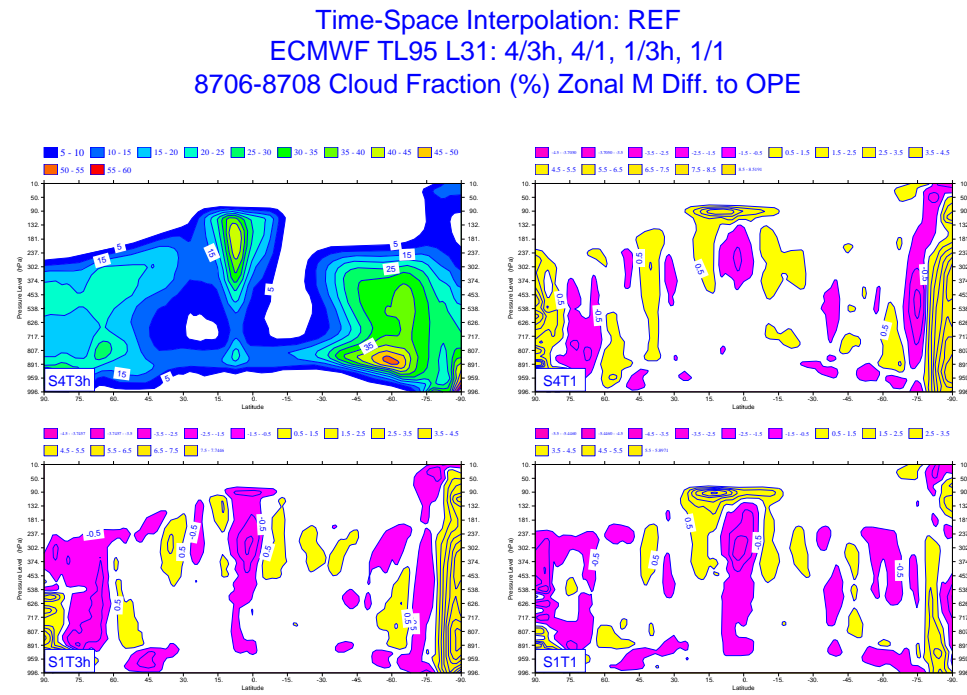
Figure 40. The zonal mean distribution of the cloud fraction averaged over the last 3 months of $T_L 95$ L31 simulations (in percent). Top left panel is the operational configuration (S4T3h), top right is the difference S4T1-S4T3h, bottom left is the difference S1T3h-S4T3h bottom right is the difference S1T1-S4T3h.

Time-Space Interpolation: REF
ECMWF TL95 L31: 4/3h, 4/1, 1/3h, 1/1
8706-8708 Temperature (K) Zonal M Difference to OPE
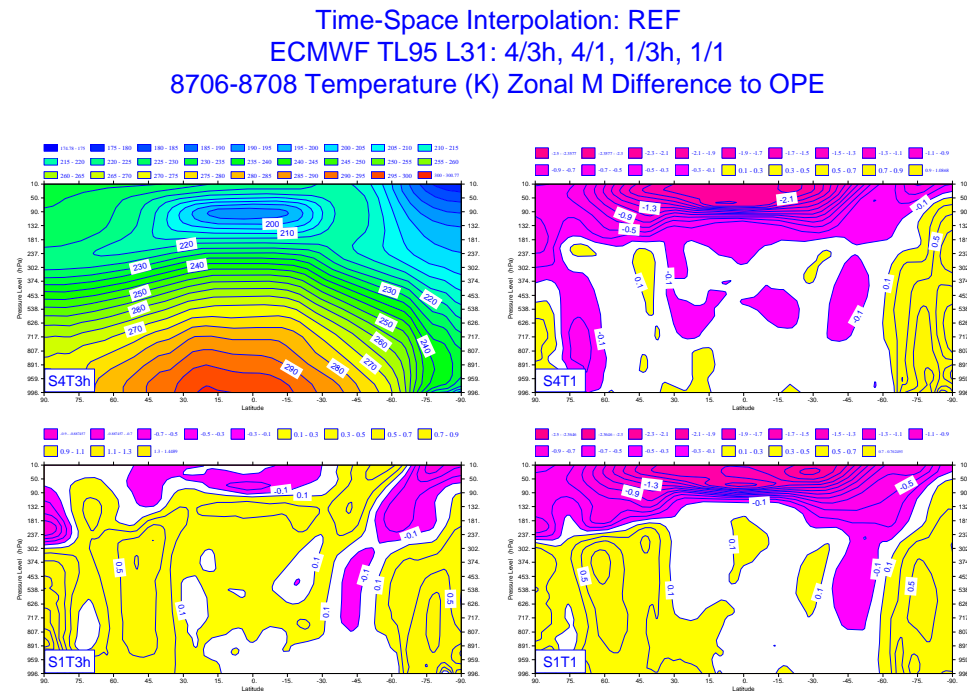
Figure 41. As in Fig. 40 , but for the zonal mean temperature (in degrees Kelvin).

Bias

Standard deviation
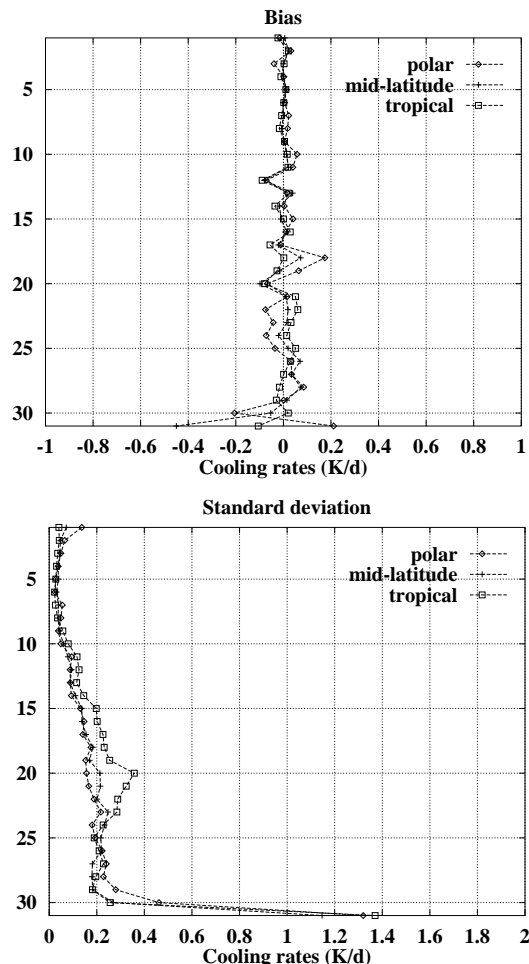
Figure 42. The bias and standard deviation of the longwave cooling rates computed with the neural network approach with respect to those computed with the operational longwave scheme, for an ensemble of profiles sampled out of the first days of the months during one year, with the T_L319 L31 operational model.

**500hPa geopotential (m)**
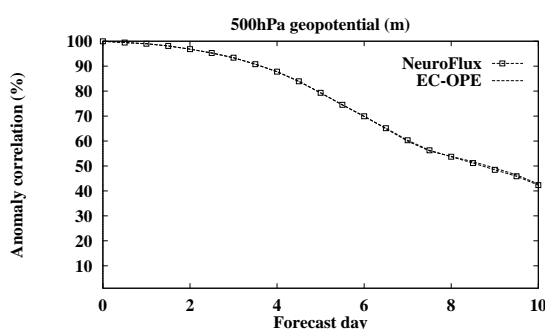
Figure 43. The anomaly correlation of the geopotential at 500 hPa for a set of experiments starting on the 15th of the month for one year. EC-OPE uses the operational LW radiation scheme, Neuro-Flux the neural network version of it.
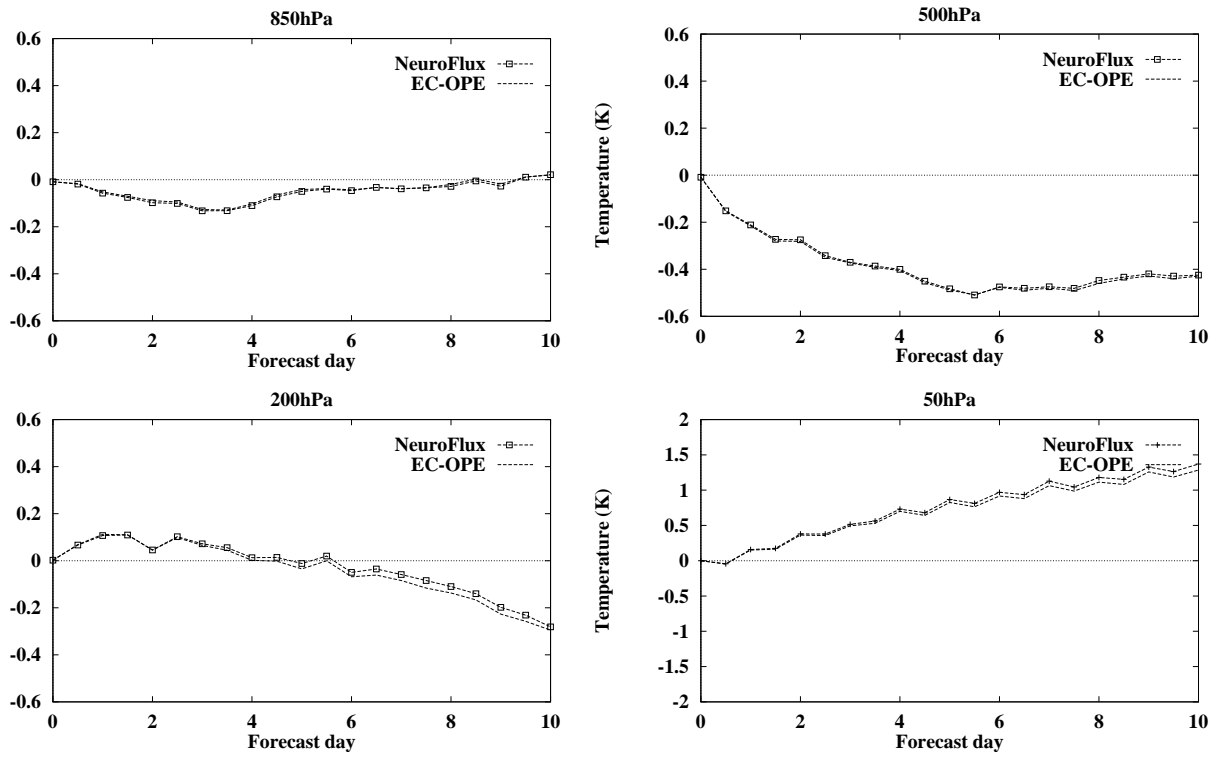
Figure 44. As in Fig. 43 , but for the mean error in temperature at 850, 500, 200 and 50 hPa.

Comparison IPA vs. Plane–Parallel / Ebert–Curry Ice Cloud

Spectral Interval: 0.25 – 0.68   CSZA=1.0   Sigma= tau/sqrt(1.0)   Fmt=0.7

Comparison IPA vs. Plane–Parallel / Ebert–Curry Ice Cloud

Spectral Interval: 0.68 – 4.00   CSZA=1.0   Sigma= tau/sqrt(1.0)   Fmt=0.7
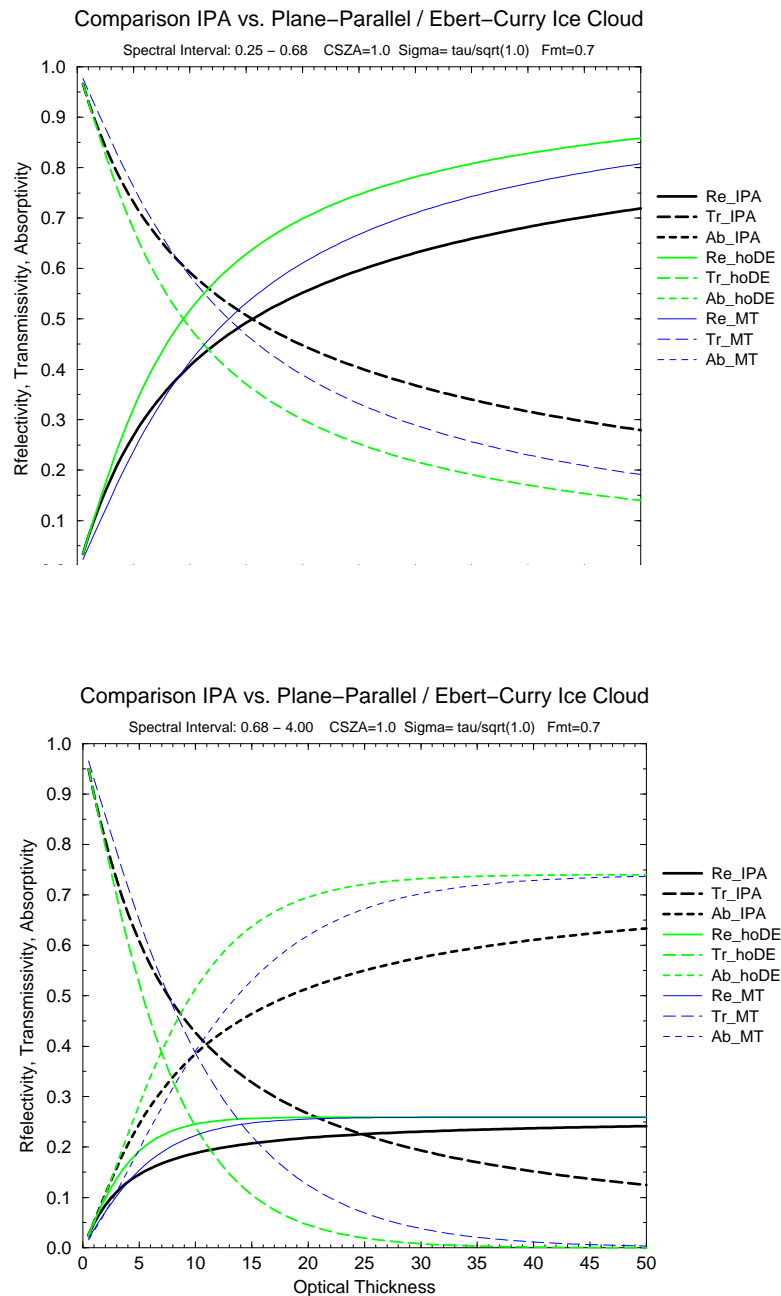
Figure 45. The transmissivity, reflectivity and absorptivity for ice clouds with optical properties from Ebert and Curry (1992), computed with Barker's (1996) IPA, the Delta-Eddington approximation and a Delta-Eddington approximation accounting for Tiedtke's (1996) inhomogeneity factor.
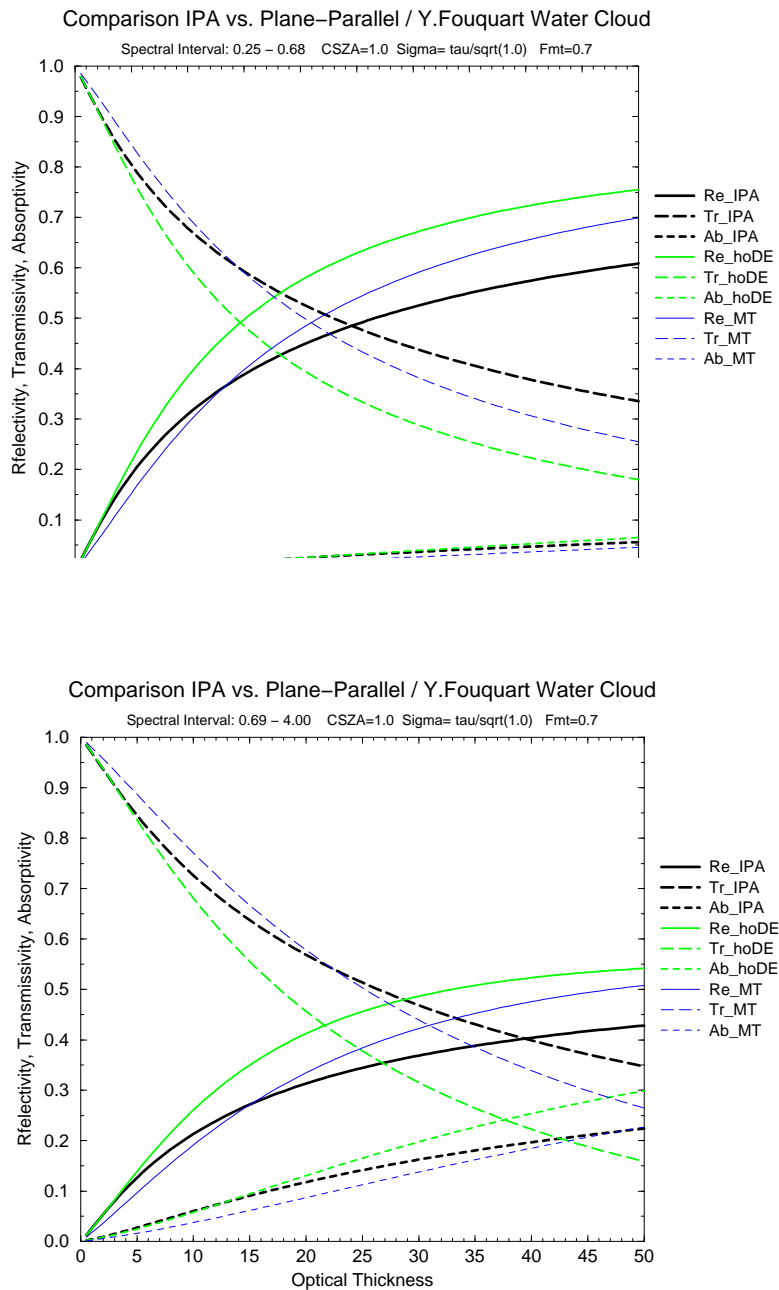
Figure 46. As in Fig. 45 , but for water clouds with optical properties from Fouquart (1987).

REFERENCES

Baer, F., N. Arsky, J.J. Charney, and R.G. Ellingson, 1996: Intercomparison of heating rates generated by global climate model longwave radiation codes. J. Geophys. Res., 101D, 26,589-26,603.

Barker, H.W., 1996: A parameterization for computing grid-averaged solar fluxes for inhomogeneous

marine boundary layer clouds. Part I: Methodology and homogeneous biases. J. Atmos. Sci., 53, 2289-2303.

Barker, H.W., J.-J. Morcrette, and D. Alexander, 1998: Broadband solar fluxes and heating rates for atmospheres with 3D broken clouds. Quart. J. Royal Meteor. Soc., 124, 1245-1271.

Barkstrom, B.R., and G.L. Smith, 1986: The Earth Radiation Budget Experiment: Science and implementation. Rev. Geophys., 24, 379-390.

Bonnel, B., Y. Fouquart, J.-C. Vanhoutte, C. Fravalo, and R. Rosset, 1983: Radiative properties of some African and mid-latitude stratocumulus clouds. Beitr. Phys. Atmosph., 56, 409-428.

Boucher, O., and U. Lohmann, 1995: The sulfate-CCN-cloud albedo effect: A sensitivity study using two general circulation models. Tellus, 47B, 281-300.

Cairns B., A.A. Lacis, and B.E. Carlson, 2000: Absorption within inhomogeneous clouds and its parameterization in general circulation models. J. Atmos. Sci., 57, 700-714.

Cess, R.D., M.H. Zhang, P. Minnis, L. Corsetti, E.G. Dutton, B.W. Forgan, D.P. Garber, W.L. Gates, J.J. Hack, E.F. Harrison, X. Jing, J.T. Kiehl, C.N. Long, J.-J. Morcrette, G.L. Potter, V. Ramanathan, B. Subasilar, C.H. Whitlock, D.F. Young, Y. Zhou, 1995: Absorption of solar radiation by clouds: Observations versus models. Science, 267, 496-499.

Chandrasekhar, S., 1935: The radiation equilibrium of the outer layer of a star with special reference to the blanquening effect of the reverse layer. Mon. Not. Roy. Astron. Soc., 95, 21.

Chandrasekhar, S., 1958: On the diffuse reflection of a pencil of radiation by a plane parallel atmosphere. Proc. Nat. Acad. Sci. USA, 44, 933-940.

Chandrasekhar, S., 1960: Radiative transfer. Dover Publications, New York.

Cheruy, F., F. Chevallier, J.-J. Morcrette, N. A. Scott, and A. Chedin, 1996: A fast method using neural networks for computing the vertical distribution of the thermal component of the Earth radiative budget. C.R.Acad.Sci., 322, IIb (in French)

Chevallier, F., A. Chedin, F. Cheruy, and J.-J. Morcrette, 2000a: TIGR-like atmospheric profile databases for accurate radiative-flux computation. Quart. J. Roy. Meteor. Soc., 126, 777-785. (also ECMWF Technical Memorandum No. 275, March 1999, 21 pp)

Chevallier, F., J.-J. Morcrette, F. Cheruy, and N.A. Scott, 2000b: Use of a neural-network-based longwave radiative transfer scheme in the ECMWF atmospheric model. Quart. J. Roy. Meteor. Soc., 126, 761-776. (also ECMWF Technical Memorandum No. 276, March 1999, 21 pp)

Chia Chou, and J. D. Neelin, 1996: Linearization of a longwave radiation scheme for intermediate tropical atmospheric models. J. Geophys. Res., 101D, 15129-151146

Chylek, P., G. Videen, D. Ngo, R.G. Pinnick, and J.D. Klett, 1995: Effect of black carbon on the optical

properties and climate forcing of sulphate aerosols. J. Geophys. Res., 100D, 16,325-16,332.

Coakley, J.A., Jr., and P. Chylek, 1975: The two-stream approximation in radiation transfer: Including the angle of the incident radiation. J. Atmos. Sci., 32, 409-418.

Curtis, A.R., 1952: Discussion. Quart. J. Roy. Meteor. Soc., 78, 638-640.

Curtis, A.R., 1956: The computation of radiative heating rates in the atmosphere. Proc. Roy. Soc., A 236, 148-156.

Cusack, S., A. Slingo, J.M. Edwards, and M. Wild, 1998: The radiative impact of a simple aerosol climatology on the Hadley Centre atmospheric GCM. Quart. J. Roy. Meteor. Soc., 124A, 2517-2526.

Darnell, W.L., W.F. Staylor, S.K. Gupta, N.A. Ritchey, and A.C. Wilber, 1992: Seasonal variation of surface radiation budget derived from ISCCP-C1 data. J. Geophys. Res., 97D, 15,741-15,760.

Deschamps, P.-Y., M. Herman, and D. Tanre, 1983: Modelisation du rayonnement solaire reflechi par l'atmosphere et la Terre, entre 0.35 et 4 microns. Rapport ESA 4393/80/F/DC(SC), 156 pp.

Ebert, E.E., and J.A. Curry, 1992: A parametrisation of ice cloud optical properties for climate models. J. Geophys. Res., 97D, 3831-3836.

Edwards, J.M., and A. Slingo, 1996: Studies with a flexible new radiation code: I: Choosing a configuration for a large-scale model. Quart. J. Roy. Meteor. Soc., 122A, 689-720.

Ellingson, R.E., J. Ellis, and S.B. Fels, 1991: The Intercomparison of Radiation Codes used in Climate Models: Longwave results. J. Geophys. Res., 96D, 8929-8954.

Elsasser, W.M., 1938: Mean absorption and equivalent absorption coefficient of a band spectrum. Phys. Rev., 54, 126-129.

Elsasser, W.M., 1942: Heat transfer by infrared radiation in the atmosphere. Harvard Meteorological Studies No.6, 107 pp.

Fels, S.B., 1979: Simple strategies for inclusion of Voigt effects in infrared cooling rate calculations.Appl. Opt., 18, 2634-2637.

Fisher, H., 1985: Absorption and emission. Promet., 15, 2/3 16-19

Fouquart, Y., 1974: Utilisation des approximants de Pade pour l'etude des largeurs equivalentes de raies formees en atmosphere diffusante. J. Quant. Spectros. Radiat. Transfer., 14, 497-508.

Fouquart, Y., and B. Bonnel, 1980: Computations of solar heating of the earth's atmosphere: a new parameterization. Beitr. Phys. Atmosph., 53, 35-62.

Fouquart, Y., 1987: Radiative transfer in climate models. NATO Advanced Study Institute on Physically-Based Modelling and Simulation of Climate and Climatic Changes. Erice, Sicily, 11-23 May 1986. M.E.

Schlesinger, Ed., Kluwer Academic Publishers, 223-284.

Fouquart, Y., B. Bonnel, and V. Ramaswamy, 1991: Intercomparing shortwave radiation codes for climate studies. J. Geophys. Res., 96D, 8955-8968.

Qiang Fu, and K.-N. Liou, 1993: Parameterization of the radiative properties of cirrus clouds. J. Atmos. Sci., 50, 2008-2025.

Qiang Fu, 1996: An accurate parameterization of the solar radiative properties of cirrus clouds for climate studies. J. Climate, 9, 2058-2082.

Qiang Fu, P. Yang, and W.B. Sun, 1998: An accurate parameterization of the infrared radiative properties of cirrus clouds of climate models. J. Climate, 11, 2223-2237.

Qiang Fu, W.B. Sun, and P. Yang, 1999: Modeling of scattering and absorption by nonspherical cirrus ice particles at thermal infrared wavelengths. J. Atmos. Sci., 56, 2937-2947.

Garratt, J.R., 1994: Incoming shortwave fluxes at the surface: A comparison of GCM results with observations. J. Climate, 7, 72-80.

Garratt, J.R., A.J. Prata, 1996: Downwelling longwave fluxes at continental surfaces - A comparison of observations with GCM simulations and implications for the global land-surface radiation budget. J. Climate, 9, 646-655.

Garratt, J.R., A.J. Prata, L.D. Rotstayn, B.J. McAvaney, and S. Cusack, 1998: The surface radiation budget over oceans and continents. J. Climate, 11, 1951-1968.

Geleyn, J.-F., and A. Hollingsworth, 1979: An economical analytical method for the computation of the interaction between scattering and line absorption of radiation. Beitr. Phys. Atmosph., 52, 1-16.

Genthon, C., 1992: Simulations of desert dust and sea-salt aerosols in Antarctica with a general circulation model of the atmosphere. Telles, 44B, 371-389.

Giorgetta, M.A., and J.-J. Morcrette, 1995: Voigt line approximation in the ECMWF radiation scheme. Mon. Wea. Rev., 123, 3381-3383.

Godson, W.L., 1953: The evaluation of infrared radiative fluxes due to atmospheric water vapour. Quart. J. Roy. Meteor. Soc., 79, 367-379.

Goody, R.M., 1952: A statistical model for water vapour absorption. Quart. J. Roy. Meteor. Soc., 78, 165-169.

Goody, R.M., 1964: Atmospheric Radiation. I: Theoretical Basis. Clarendon Press, Oxford.

Gupta, S.K., A.C. Wilber, W.L. Darnell, and J.T. Suttles, 1993: Longwave surface radiation over the globe from satellite data: An error analysis. Intern. J. Remote Sensing, 14, 95-114.

Qingyuan Han, W.B. Rossow, and A. Lacis, 1994: Near-global survey of effective droplet radii in liquid water clouds using ISCCP data. J. Climate, 7, 465-497.

Harrison, E.F., D.R. Brooks, P. Minnis, B.A. Wielicki, W.F. Staylor, G.G. Gibson, D.F. Young, F.M. Denn, and the ERBE Science Team, 1988: First estimates of the diurnal variation of longwave radiation from the multiple-satellite Erath Radiation Budget Experiment (ERBE), 1988: Bull. Amer. Meteor. Soc., 69, 1144-1151.

Harrison, E.F., P. Minnis, B.R. Barkstrom, V. Ramanathan, R.D. Cess, and G.G. Gibson, 1990: Seasonal variation of cloud radiative forcing derived from the Earth Radiation Budget Experiment. J. Geophys. Res., 95D, 18,687-18,704.

Joseph, J.H., W.J. Wiscombe, and J.A. Weinman, 1976: The Delta-Eddington approximation for radiative flux transfer. J. Atmis. Sci., 33, 2452-2459.

Joussaume, S., 1990: Three-dimensional simulations of the atmospheric cycle of desert dust particles using a general circulation model. J. Geophys. Res., 95, 1909-1941.

Kandel, R.S., M. Viollier, P. Raberanto, J.-Ph. Duvel, L.A. Pakhomov, V.A. Golovko, A.P. Trishchenko, J. Mueller, E. Raschke, R. Stuhlmann, and the International ScaRaB Scientific Working Group. 1998 Bull. Amer. Meteor. Soc., 79, 765-783.

Laszlo, I., and R.T. Pinker, 1993: Shortwave cloud-radiative forcing at the top of the atmosphere, at the surface and of the atmospheric column as determined from ISCCP C1 data. J. Geophys.Res., 98D, 2703-2718.

Le Treut, H., M. Forichon, O. Boucher, and Z.-X. Li, 1998: Sulfate aerosol indirect effect and CO2 greenhouse forcing: Equilibrium response of the LMD GCM and associated cloud feedbacks. J. Climate, 11, 1673-1684

Li, Zhanqing, and H.G. Leighton, 1993: Global climatologies of solar radiation budgets at the surface and in the atmosphere from 5 years of ERBE data. J. Geophys. Res., 98D, 4919-4930.

Liou, K.-N., 1980: An Introduction to Atmospheric Radiation. International Geophysics Series, Vol. 25, Academic Press, 392 pp.

Liou, K.-N., 1992: Radiation and cloud processes in the atmosphere Oxford University Press, Oxford, New York, 487 pp.

Lohmann, U. and J. Feichter, 1997: Impact of sulfate aerosols on albedo and lifetime of clouds: A sensitivity study with the ECHAM4 GCM, J. Geophys. Res., 102, 13,685-13,700.

Malkmus, W., 1967: Random Lorentz band model with exponential tailed 1/S line intensity. J. Optic. Soc. Amer., 57, 323-329.

Mitchell, J.F.B., T.C. Johns, J.M. Gregory, and S.F.B. Tett, 1995: Climate response to increasing levels of greenhouse gases and sulphate aerosols. Nature, 376, 6540, 501-504.

Mlawer, E.J., S.J. Taubman, P.D. Brown, M.J. Iacono, and S.A. Clough, 1997: Radiative transfer for inhomogeneous atmospheres: RRTM, a validated correlated-k model for the longwave. J. Geophys. Res., 102D, 16,663-16,682.

Morcrette, J.-J. , and Y. Fouquart, 1985: On systematic errors in parametrized calculations of longwave radiation transfer. Quart.J.Roy.Meteor.Soc., 111, 691-708.

Morcrette, J.-J., L. Smith, and Y. Fouquart, 1986: Pressure and temperature dependence of the absorption in longwave radiation parameterizations. Beitr. Phys. Atmosph., 59, 455-469.

Morcrette, J.-J., 1990: Impact of changes to the radiation transfer parameterizations plus cloud optical properties in the ECMWF model. Mon. Wea. Rev., 118, 847-873.

Morcrette, J.-J., 1991a: Radiation and cloud radiative properties in the ECMWF operational weather forecast model. J. Geophys. Res., 96D, 9121-9132.

Morcrette, J.-J., 1991b: Evaluation of model-generated cloudiness: Satellite observed and model-generated diurnal variability of brightness temperature. Mon. Wea. Rev., 119, 1205-1224.

Morcrette, J.-J., 1993: Revision of the clear-sky and cloud radiative properties in the ECMWF model. ECMWF Newsletter, 61, 3-14.

Morcrette, J.-J., 2000: On the effects of the temporal and spatial sampling of radiation fields on the ECMWF forecasts and analyses. Mon. Wea. Rev., 128, 876-887. (also ECMWF Technical Memorandum No. 277)

Morcrette, J.-J., and Ch. Jakob, 2000: Response of the ECMWF model to changes in cloud overlap assumption. Mon. Wea. Rev., 128, to appear. (also ECMWF Technical Memorandum No. 278)

Ohmura, A., E.G. Dutton, B. Forgan, C. Frohlich, H. Gilgen, H. Hegner, A. Heimo, G. Konig-Langlo, B. McArthur, G. Muller, R. Philipona, R. Pinker, C.H. Whitlock, K. Dehne, and M. Wild, 1998: Baseline Surface Radiation Netweork (BSRN/WCRP): New precision radiometry for climate research. Bull. Amer. Meteor. Soc., 79, 2115-2136.

Paltridge, G. W., and C. M. R. Platt, 1976: "Radiative processes in meteorology and climatology". Elsevier, New York, 318 pp.

Pilewskie, P., and F. Valero, 1995: Direct observations of excess soalr absorption by clouds. Science, 267, 1626-1629.

Quenzel, H., 1985: Radiation from molecules and aerosol particles. Promet., 15, 2/3, 7-9.

Ramanathan, V., 1987: The role of Earth Radiation Budget studies in climate and general circulation research. J. Geophys. Res., 92D, 4075-4096.

Ramaswamy, V., and S.M. Freidenreich, 1992: A study of broadband parameterizations of the solar radiative interactions with water vapor and water drops. J. Geophys. Res., 97D, 11,487-11,512.

Ramanathan, V., B. Subalisar, G.J. Zhang, W.C. Conant, R.D. Cess, J.T. Kiehl, H. Grassl, and L. Shi, 1995: Warm pool heat budget and short wave cloud forcing. A missing physics. Science, 267, 499-503.

Rodgers, C.D., 1967: The use of emissivity in atmospheric radiation calculations. Quart. J. Roy. Meteor. Soc., 93, 43-54.

Rodgers, C.D., and C.D. Walshaw, 1966: The computation of the infrared cooling rate in planetary atmospheres. Quart. J. Roy. Meteor. Soc., 92, 67-92.

Rossow, W.B., 1993: Satellite observations of radiation and clouds to diagnose energy exchanges in the climate. in Energy and Water Cycles in the Climate System. E. Raschke, D. Jacob, Eds., NATA ASI Vol. 15, Springer-Verlag Berlin Heidelberg, 123-141 (Part I); 143-164 (Part II).

Rossow, W.B., E. Kinsella, A. Wolf, and L. Garder, 1987: International Satellite Cloud Climatology Project (ISCCP): Description of Reduced Resolution Radiance Data. July 1985 (revised July 1987). WMO/TD-No.58, World Meteorological Organization, Geneva, 143 pp.

Rothman, L.S., et al., 1998: The HITRAN molecular spectroscopic database and HAWKS: 1996 Edition. J.Quant. Spectros. Radiat. Transfer, 60, 665-710.

Schulz, M., Y.J. Balkanski, W. Guelle, and F. Dulac, 1998: Role of aerosol size distribution and source location in a three-dimensional simulation of a Saharan dust episode tested against satellite-derived optical thickness. J. Geophys. Res., 103D, 10,579-10,592.

Schultz, F.M., K. Stamnes, and J.J. Stamnes, 1999: Shape dependence of the optical properties in size-shape distributions of randomly oriented prolate spheroids, including highly elongated shapes. J. Geophys. Res., 104D, 9413-9422.

Shettle, E.P., and J.A. Weinman, 1970: The transfer of solar irradiance through inhomogeneous turbid atmospheres evaluated by Eddington's approximation. J. Atmos. Sci., 27, 1048-1055.

Smith, E. A., and Lei Shi, 1992: Surface forcing of the infrared cooling profile over the Tibetan plateau. Part I: Influence of relative longwave radiative heating at high altitude. J. Atmos. Sci., 49, 805-822.

Stephens, G.L., 1979: Optical properties of eight water cloud types. C.S.I.R.O. Div. Atmos. Phys., Tech. Paper No. 36, 1-36.

Stephens, G.L., 1988: Radiative transfer through arbitrarily shaped optical media: Part I: A general method of solution. J. Atmos. Sci., 45, 1818-1836. Part II: Group theory and simple closures. J. Atmos. Sci., 45, 1837-1848.

Stephens, G.L., 1984: The parameterization of radiation for numerical weather prediction and climate models. Mon. Wea. Rev., 112, 826-867.

Stephens, G.L., 1996: How much solar radiation do clouds absorb? Science, 271, 1131-1134.

Stephens, G.L., and P.J. Webster, 1979: Sensitivity of radiative forcing to variable cloud and moisture. J. Atmos. Sci., 36, 1542-1556.

Stowe, L.L., et al., 1989: Nimbus-7 Global Cloud Climatology. Part II: First year results. J. Climate, 2, 671-709.

Stubenrauch, C.J., A.D. Del Genio, and W.B. Rossow, 1997: Implementation of subgrid cloud vertical structure inside a GCM and its effect on the radiation budget. J. Climate, 10, 273-287.

Takano, Y., and K.-N. Liou, 1989: Solar radiative transfer in cirrus clouds. Part I: Single scattering and optical properties of hexagonal ice crystals. J. Atmos. Sci., 46, 3-19. Part II: Theory and computations of multiple scattering in an anisotropic medium. J. Atmos. Sci., 46, 20-36. Radiative transfer in cirrus clouds. Part III: Light scattering by irregular ice crystals. J. Atmos. Sci., 52, 818-837.

Tanre, D. J.-F. Geleyn, and J. Slingo, 1984: First results of the introduction of an advanced aerosol-radiation interaction in the ECMWF low resolution global model. in Aerosols and Their Climatic Effects, H.E. Gerber and A. Deepak, Eds., A. Deepak Publ., Hampton, Va., 133-177.

Tegen, I., P. Hollrigl, M. Chin, I. Fung, D. Jacob, and J. Penner, 1997: Contribution of different aerosol species to the global aerosol extinction optical thickness: Estimates from model results, J. Geophys. Res., 102, 23,895-23.915.

Tiedtke, M., 1996: An extension of cloud-radiation parameterization in the ECMWF model: The representation of sub-grid scale variations of optical depth. Mon. Wea. Rev., 124, 745-750.

Timmreck, C., J. Feichter, H-F. Graf, I. Kirchner and E. Manzini, 1997: Interactive simulations of Mt. Pinatubo stratospheric aerosol, J. Aerosol. Sci., 28, Suppl. 1, 5723-5724.

Wang Junhong, and W.B. Rossow, 1995: Determination of cloud vertical structure from upper-air observations. J. Appl. Meteor., 34, 2243-2258.

Washington, W.M., and D.L. Williamson, 1977: A description of the NCAR GCMs. "GCMs of the atmosphere". J. Chang, Ed., Methods in computational physics, Vol. 17, Academic Press, 111-172.

Webster, P.J., and G.L. Stephens, 1980: Tropical upper tropospheric extended clouds: Inferences from Winter MONEX. J. Atmos. Sci., 37, 1521-1541.

Wielicki, B.A., et al., 1996: Clouds and the Earth's Radiation Energy System (CERES): An Earth Observing System experiment. Bull. Amer. Meteor. Soc., 77, 853-868.

Wyser, K., 1998: The effective radius of ice clouds. J. Climate, 11, 1793-1802.

Zhang, Y.-C., W.B. Rossow, and A.A. Lacis, 1995: Calculation of surface and top of the atmosphere radiative fluxes from physical quantities based on ISCCP data sets, 1: Method and sensitivity to input data uncertainties. J. Geophys. Res., 100, 1149-1166.